WILLIAM & MARY

CHARTERED 1693

Dissertations, Theses, and Masters Projects   Theses, Dissertations, & Master Projects

2008

Ultrasonic guided wave interpretation for structural health inspections

Jill Paisley Bingham

College of William & Mary - Arts & Sciences

Follow this and additional works at: https://scholarworks.wm.edu/etd

Part of the Acoustics, Dynamics, and Controls Commons, and the Civil Engineering Commons

Ultrasonic Guided Wave Interpretation for Structural Health Inspections

Jill Paisley Bingham

Norfolk, VA

Bachelor of Arts in Physics, Carleton College, 2004

A Dissertation presented to the Graduate Faculty
of the College of William and Mary in Candidacy for the Degree of
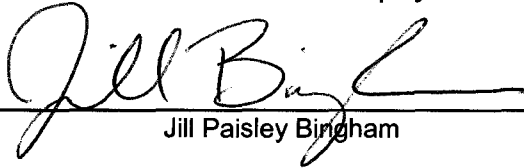Doctor of Philosophy

Department of Applied Science

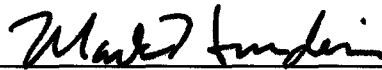The College of William and Mary
January 2009

APPROVAL PAGE

This Dissertation is submitted in partial fulfillment of
the requirements for the degree of

Doctor of Philosophy
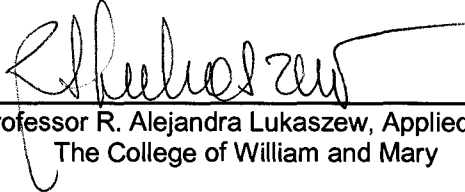
_____
Jill Paisley Bingham

Approved by the Committee, December 2008

_____
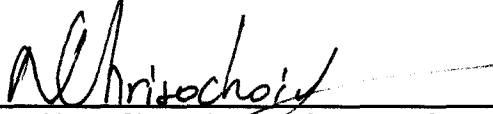Committee Chair
Professor Mark K. Hinders, Applied Science
The College of William and Mary

_____
VMEC Associate Professor R. Alejandra Lukaszew, Applied Science and Physics
The College of William and Mary

_____
Assistant Professor Christopher A. Del Negro, Applied Science
The College of William and Mary

_____
Professor Nikos Chrisochoides, Computer Science
The College of William and Mary

ABSTRACT PAGE

Structural Health Management (SHM) combines the use of onboard sensors with artificial intelligence algorithms to automatically identify and monitor structural health issues. A fully integrated approach to SHM systems demands an understanding of the sensor output relative to the structure, along with sophisticated prognostic systems that automatically draw conclusions about structural integrity issues. Ultrasonic guided wave methods allow us to examine the interaction of multimode signals within key structural components. Since they propagate relatively long distances within plate- and shell-like structures, guided waves allow inspection of greater areas with fewer sensors, making this technique attractive for a variety of applications.

This dissertation describes the experimental development of automatic guided wave interpretation for three real world applications. Using the guided wave theories for idealized plates we have systematically developed techniques for identifying the mass loading of underwater limpet mines on US Navy ship hulls, characterizing type and bonding of protective coatings on large diameter pipelines, and detecting the thinning effects of corrosion on aluminum aircraft structural stringers. In each of these circumstances the signals received are too complex for interpretation without knowledge of the guided wave physics. We employ a signal processing technique called the Dynamic Wavelet Fingerprint Technique (DFWT) in order to render the guided wave mode information in two-dimensional binary images. The use of wavelets allows us to keep track of both time and scale features from the original signals. With simple image processing we have developed automatic extraction algorithms for features that correspond to the arrival times of the guided wave modes of interest for each of the applications. Due to the dispersive nature of the guided wave modes, the mode arrival times give details of the structure in the propagation path.

For further understanding of how the guided wave modes propagate through the real structures, we have developed parallel processing, 3D elastic wave simulations using the finite integration technique (EFIT). This full field, numeric simulation technique easily examines models too complex for analytical solutions. We have developed the algorithm to handle built up 3D structures as well as layers with different material properties and surface detail. The simulations produce informative visualizations of the guided wave modes in the structures as well as the output from sensors placed in the simulation space to mimic the placement from experiment. Using the previously developed mode extraction algorithms we were then able to compare our 3D EFIT data to their experimental counterparts with consistency.

Contents

List of Figures

List of Tables

For my Dad

In memory of
Mary Louise Bingham (1945-2004)

Acknowledgments

I would first like to express great appreciation to my advisor, Professor Hinders for his guidance through this graduate program. His clever mentorship and instruction provided me with much insight and many opportunities without which I could not have completed this work. Through this experience I have not only learned about searching for scientific knowledge but also valuable life skills from him. I thank my committee Ale Lukaszew, Christopher Del Negro and Nikos Chrisochoides for taking the time to read my dissertation and give me feedback in oder to obtain this degree. I would also like to thank all the present and former lab members including Dr. Kevin Leonard, Dr. Kevin Rudd, Dr. Adam Friedman, Corey Miller, Cara Campbell and Jonathan Stevens for collaboration and hard work associated with this work. I thank Chris Bording for all his time and help with introducing me to parallel computing, making a large part of this research possible.

To my family, I thank you for all of your love and support through my life and the past four years. I'm truly blessed to be part of such a amazing family. To my roommates, Dianna and Meridyth, thank you for putting up with all my crazy hours and supporting me through writing my dissertation. To the William and Mary Women's Frisbee Team, thank you for all of the hours of stress relief and friendships on campus, without which I would have struggled. And finally, thank you to my friends for keeping me sane through this experience.

Chapter 1

Introduction

Structural Health Monitoring (SHM) combines the use of onboard sensors with artificial intelligence algorithms to automatically identify and monitor structural health issues. A fully integrated approach to SHM systems demands an understanding of the sensor output relative to the structure, along with sophisticated prognostic systems that automatically draw conclusions about structural integrity issues. Ultrasonic guided wave methods allow us to examine the interaction of multimode signals within key structural components. Since they propagate relatively long distances within plate- and shell-like structures, guided waves allow inspection of greater areas with fewer sensors, making this technique attractive for a variety of applications.

This dissertation describes the experimental development of automatic guided wave interpretation for three real world applications. Using the guided wave theories for idealized plates we have systematically developed techniques for identifying the mass loading of underwater limpet mines on US Navy ship hulls, characterizing the type and bonding of protective coatings on large diameter pipelines,

and detecting the thinning effects of corrosion on aluminum aircraft structural stringers. In each of these circumstances the signals received are too complex for interpretation without knowledge of the guided wave physics. We employ a signal processing technique called the Dynamic Wavelet Fingerprint Technique (DFWT) in order to render the guided wave mode information in two-dimensional binary images. The use of wavelets allows us to keep track of both time and scale features from the original signals. With simple image processing we have developed automatic extraction algorithms for features that correspond to the arrival times of the guided wave modes of interest for each of the applications. Due to the dispersive nature of the guided wave modes, the mode arrival times give details of the structure in the propagation path.

For further understanding of how the guided wave modes propagate through the real structures, we have developed parallel processing, 3D elastic wave simulations using the finite integration technique (EFIT). This full field, numeric simulation technique easily examines models too complex for analytical solutions. We have developed the algorithm to handle built up 3D structures as well as layers with different material properties and surface detail. The simulations produce informative visualizations of the guided wave modes in the structures, but also directly mimic output from sensors placed in the simulation space for direct comparison to experiment. Using our previously developed mode extraction algorithms we were then able to compare our 3D EFIT data to their experimental counterparts with consistency.

1.1 Guided Lamb Waves

The basic formulation and discussion of the wave mechanics and elasticity can be found in various texts [1–5], as well as extensive literature reviews of work done in the field of guided elastic waves for application in SHM [6,7]. This dissertation builds on a previous line of research we've developed over the past decade, well recorded in [8–24]. Here, we will point out some of the major breakthroughs of the field as well as recent advancements in the specific areas discussed in this dissertation.

The field of elastic guided waves was first studied in 1885 by Lord Rayleigh [25] who was concerned with the propagation of surface waves along a solid, e.g. earthquakes. The study of two-dimensional elastic waves in a bound plate was presented by Lamb [26] in 1917, hence the name given to Lamb waves in a traction-free plate. In this work he derived "period-equations" for the symmetric and antisymmetric modes which have since become known as the dispersion relations. Through the years the term Lamb waves has been extended to include waves in more general plate-like structures. Mindlin presented a two dimensional theory of flexural waves of isotropic, elastic plates deduced from the three-dimensional equations of elasticity which were close to Lamb's original solutions, but computationally more simple [27]. In 1957 Worlton presented the first results from the experimental testing of aluminum plates in a tank for laminar flaws and radial cracks, and he also presented some suggestions of the practical use of Lamb waves [28]. His second experimental work with Lamb waves in 1961 rewrote the Lamb dispersion relations into the currently used notation, as well as graphically related the phase velocity of the modes to the frequency thickness of the plate [29].

Early work by Gazis in 1959 developed an exact elastic wave solution for a

3

hollow cylinder [30,31]. Since then many more authors have added to the guided waves in hollow cylinder literature. But it has also been proposed that the non-axisymmetric propagation of guided waves in a pipe correspond to Lamb waves in unwrapped pipes. Leonard and Hinders in 2005 showed that it is possible to obtain tomographic reconstructions of pipe wall thickness using mimicked cross-hole geometries [20]. Li and Rose used this approximation in 2005 to derive a simplified model to calculate the phase velocities of non-axisymmetric flexural mode guided waves [32]. Luo, Zhao and Rose showed that although a pipe model is more accurate for a pipe experiment, a plate model often gives a quick and sufficient solution for a pipe [33].

1.2 Multi-layered Plates and Pipes

By 1978, researchers had begun studying more complex plates and pipes, Nayfeh and Nassar for example found that the stiffer a bonding material the more influence it had on the wave propagation through laminated composites [34]. Claus and Kline analyzed the effect of interfacial surface roughness on the propagation of Stoneley waves guided along the interface of two dissimilar media [35]. They found that the Stoneley wave attenuation increased as a function of increasing surface roughness. Schoenberg studied the elastic wave behavior across slip boundaries where the displacement between two layers does not have to be continuous, and showed that the reflection and transmission coefficients are frequency dependent [36]. The experimental detection of slip boundaries was found possible by considering the changes in the reflection coefficients at an incident angle as a function of frequency [37]. Xu and Datta showed that increased stiff-

4

ness and increased density have similar effects of lowering the cutoff frequency of guided wave modes in a bonded plate [38]. In 1991 Nayfeh presented an exact analytical treatment of elastic wave propagation in multi-layered anisotropic media using the transfer matrix method, which derives the individual layer solutions as wave amplitudes, then eliminating these amplitudes relates the stresses and displacements on one side of the layer to the other [39]. Laperre and Thys showed experimentally and theoretically that Lamb mode coupling between and polymer coating and aluminum plate makes the bilayer system switch between modes [40]. In 1993 Xu *et al.* used a method to decouple leaky Lamb wave data to determine the unknown elastic wave speed of a coating [41]. Rose *et al.* presented research on the correlation between the thickness of a coating of a bilayer system to the influence it has on the generation of Lamb wave modes [42]. The assertion was that if the layer thickness was $0.027 < d_p < 0.083$ mm the changes observed were minimal.

In 1995 Lowe wrote a review paper of the progression predictive methods for propagating waves in plates including dealing with multilayered plates, concentrating on the derivation of the 'Transfer Matrix' and 'Global Matrix' methods, and pointing out their short comings in the large frequency-thickness product [43]. Moulin *et al.* presented work starting in 2000 modeling the generation of Lamb waves using a coupled finite element-normal modes expansion method [44], [45]. In 2004 Duquenne *et al.* took this coupled method and extended it to the modeling of viscoelastic materials showing the attenuation of some modes in these layers [46]. By choosing modes with little attenuation from the viscoelastic layer, longer propagation distances are possible. Galàn and Abascal then used a hybrid finite element-boundary element method which explicitly included the attenuat-

ing characteristics of the coating to determine the Lamb mode conversion factors at defects under the coating [47]. Bashinger and Rose described how to use the global transfer matrix method to determine the dispersion equations, numerically solving for the phase velocity and attenuation of guided wave modes, and then verified these results with experiment [48]. In 2007 Luo and Rose applied phased array focusing to guided waves in a viscoelastic coated cylinder and showed that amplitude attenuation increased with the viscoelastic properties, but the phased array focusing increased the energy so that longer inspection distances could be achieved [49]. These results were obtained both numerically with a finite element model and experimentally.

1.3   Numerical Simulation

Along with finite element techniques, numeric modeling using the elastodynamic finite integration technique (EFIT) have proved very useful for modeling guided wave behavior. Fellinger *et al.* originally developed the basic equations of EFIT along with a unique way to discretize the material parameters for insured continuity of stress and displacement across the staggered grid in 1995 [50]. Schubert *et al.* then adapted the EFIT equations into cylindrical coordinates (CEFIT) to investigate axisymmetric wave propagation in pipes with a 2D grid [51]. In 2001 Schubert presented results looking at elastic wave propagation in porous concrete but due to computational limitations could only model 5 cm x 5 cm x 10 cm spaces with periodic boundary conditions [52]. Then in 2004 Schubert gave an overview of the flexibility of EFIT with discretization in Cartesian, cylindrical and spherical coordinates and showed a wide range of modeling applications [53]. Rudd *et al.*

then showed that the CFIT could be extended to a 3DCEFIT to include bends in pipes and to model phased array focusing after pipe bends [54]. 3DCEFIT was implemented in parallel in order to be able to model complex pipes.

1.4 Wavelet Analysis of Ultrasonic Signals

Ultrasonic signal analysis with wavelet transforms was first studied by Abbate in 1994 who found that if the mother wavelet was well defined there was good peak detection even with large amounts of added white noise [55]. Massicotte, Goyette and Bose then found that even noisy EMAT sensor signals were resolvable using the multi-scale method of the wavelet transform [56]. One of the strengths compared to the fast Fourier transform was that the extraction algorithm did not need to include the inverse transform, the arrival time could be taken directly from the time frequency domain of the wavelet transform. In 2002 Perov *et al.* considered the basic principles of the formulation of the wavelet transform for the purpose of an ultrasonic flaw detector and concluded that any of the known systems of orthogonal wavelets are suitable for this purpose as long as the number of levels does not drop below 4-5 [57]. In 2003 Lou and Hu found that the wavelet transform was useful in suppressing non-stationary wideband noisy from speech [58]. In a comparison study between the Wigner-Ville distribution and the wavelet transform, preformed by Zou and Chen, the wavelet transform out preformed the Wigner-Ville in terms of sensitivity to the change in stiffness of a cracked rotor [59]. In 2002 Hou and Hinders developed a multi-mode arrival time extraction tool that rendered the time series data in 2D time-scale binary images [60]. Since then this technique has been applied to multi-mode extraction of Lamb

wave signals for tomographic reconstruction [17,61], time domain reflectometry signals wiring flaw detection [62,63] and a periodontal probing device [64].

1.5   Research

In this work we build on this base for the development of guided wave inspection systems of real world structures. We show that the guided waves are sensitive to a variety of flaws including mass loading on the surface of a plate, delaminations under a viscoelastic coating and corrosion thinning. In each of our applications we've modified the wavelet fingerprinting technique [60] to extract mode arrival information from the signals. Finally we've developed parallel processed 3D EFIT simulations to model each of the application scenarios so that we can visualize the elastic wave energy and study the interactions with the structures in depth.

Chapter 2

Fundamentals

Our motivation is to identify problem areas in structures before failure occurs. We do this by developing techniques using ultrasound to provide quantitative information about the structure. In particular we use ultrasonic guided waves such as Lamb waves. Most of the development is carried out experimentally in the lab, then we use signal processing in order to present the complex data in a form that is easy to understand without extensive knowledge of the guided wave physics. In doing this we implement the Dynamic Wavelet Fingerprinting Technique (DWFT). This chapter lays out the foundation for each of these different aspects needed to conduct our research.

2.1   Guided Waves

Ultrasound consists of small vibrations of elastic media. In order to be in the ultrasonic range the frequencies of these vibrations are above 20 kHz, which is the human hearing threshold. Elastic solids can vibrate in two fashions: compressional or shear. This follows from the fundamental field equation of motion in tensor

9

notation:

$$\rho \partial_t^2 u_i - \partial_j \sigma_{ij} = 0 \qquad (2.1)$$

where the stress tensor (σ_{ij}) is directly proportional to the strain tensor (ϵ_{kl}) given by generalized Hooke's law

$$\sigma_{ij} = C_{ijkl}\epsilon_{kl} \qquad (2.2)$$

and where for an isotropic material,

$$C_{ijkl} = \delta_{ij}\delta_{kl}\lambda + (\delta_{ik}\delta_{jl} + \delta_{il}\delta_{jk})\mu$$

and we assume the strains are small

$$\epsilon_{kl} = \frac{1}{2}(\partial_k u_l + \partial_l u_k).$$

Here u_i is the displacement vector field in a three-dimensional elastic material, λ and μ are the material's Lamé constants. Substituting into (2.1) we derive Navier's wave equation

$$\rho \partial_t^2 u_i - \mu \partial^2 u_i - (\lambda + \mu)\partial_i(\partial_j u_j) = 0$$

or in vector notation,

$$\rho \partial_t^2 \vec{u} - \mu \nabla^2 \vec{u} - (\lambda + \mu)\nabla(\nabla \cdot \vec{u}) = 0. \qquad (2.3)$$

Next we suppress the harmonic time variation for simplicity through

$$\partial_t \Rightarrow -i\omega \quad \partial_t^2 \Rightarrow -\omega^2$$

10

where (2.3) becomes

$$-\omega^2\rho\vec{u} - \mu\nabla^2\vec{u} - (\lambda + \mu)\nabla(\nabla \cdot \vec{u}) = 0. \tag{2.4}$$

This can be solved through a Helmholtz decomposition, since any vector field can be generated by a pair of potentials: a scalar potential (Φ) that has no curl and a vector potential ($\vec{H}$) which has no divergence.

$$\vec{u} = \vec{u}_L + \vec{u}_T = \nabla\Phi + \nabla \times \vec{H} \text{ where } \nabla \cdot H = 0 \tag{2.5}$$

Substituting (2.5) into (2.4), and using vector identities

$$\nabla \times \nabla \times \vec{X} = \nabla(\nabla \cdot \vec{X}) - \nabla^2\vec{X}$$

$$\nabla \cdot \nabla\Phi = \nabla^2\Phi$$

$$\nabla \times \nabla \times \nabla\Phi = 0$$

$$\nabla \cdot \nabla \times \vec{H} = 0,$$

leaves us with

$$\left[\omega^2 + \frac{\lambda + 2\mu}{\rho}\nabla^2\right]\Phi = 0 \tag{2.6}$$

$$\left[\omega^2 + \frac{\mu}{\rho}\nabla^2\right]H = 0. \tag{2.7}$$

With a closer look at these we see that (2.6) is just a compressional, longitudinal wave traveling with velocity

$$c_L = \sqrt{\frac{\lambda + 2\mu}{\rho}} \tag{2.8}$$

11

and similarly (2.7) is a rotational, shear wave with velocity

$$c_T = \sqrt{\frac{\mu}{\rho}}. \tag{2.9}$$

The resulting linearly independent scalar wave equations,

$$\nabla^2 \Phi = \frac{1}{c_L^2} \frac{\partial^2 \Phi}{\partial t^2} \tag{2.10}$$

$$\nabla^2 H_n = \frac{1}{c_T^2} \frac{\partial^2 H_n}{\partial t^2} \qquad n = x, y, z \tag{2.11}$$

show that the longitudinal and shear bulk waves propagate without mutual interaction in an unbounded homogeneous material. These types of waves are only coupled when they interact with the boundaries of the material. This coupling gives rise to the development of guided Lamb wave modes in plate-like or pipe-like structures.

In plate-like materials where the wavelength is on the same order as the thickness, the two boundaries cause multiple reflections and mode conversions, so it becomes inconvenient to continue thinking of the waves as longitudinal and transverse. Rather, due to the superposition of the longitudinal and transverse modes, the plate develops new wave packets that propagate throughout the thickness of the plate. If we step back to the Helmholtz decomposition (2.5) and consider the combination of the displacement potentials (2.10), (2.11) we can follow the development of the Lamb wave solutions. For the complete derivation and discussion see Graff [3].

We define a coordinate system with a plate in the $x - z$ plane with the top and bottom boundaries at $y = \pm b$ (Figure 2.1). If we exclude variations with respect

Figure 2.1: Coordinates for a plate in the $x-z$ plane with thickness $y = 2b$.

to the z-direction we are left with the displacement components of

$$
\begin{aligned}
u_x &= \frac{\partial \Phi}{\partial x} + \frac{\partial H_z}{\partial y} \\
u_y &= \frac{\partial \Phi}{\partial y} + \frac{\partial H_z}{\partial x} \\
u_z &= -\frac{\partial H_x}{\partial y} + \frac{\partial H_y}{\partial x}.
\end{aligned}
\tag{2.12}
$$

Assuming plane waves propagating in the $x-z$ plane we can write

$$
\begin{aligned}
\Phi &= f(y)e^{i(\xi x - \omega t)} \\
H_x &= h_x(y)e^{i(\xi x - \omega t)} \\
H_y &= h_y(y)e^{i(\xi x - \omega t)} \\
H_z &= h_z(y)e^{i(\xi x - \omega t)},
\end{aligned}
\tag{2.13}
$$

13

giving solutions to (2.10) and (2.11):

$$\Phi = (A \cos \alpha y + B \sin \alpha y)e^{i(\xi x - \omega t)}$$

$$H_x = (C \cos \beta y + D \sin \beta y)e^{i(\xi x - \omega t)}$$

$$H_y = (E \cos \beta y + F \sin \beta y)e^{i(\xi x - \omega t)} \qquad (2.14)$$

$$H_z = (G \cos \beta y + H \sin \beta y)e^{i(\xi x - \omega t)}$$

where

$$\alpha^2 = \frac{\omega^2}{c_L^2} - \xi^2 \quad \text{and} \quad \beta^2 = \frac{\omega^2}{c_T^2} - \xi^2. \qquad (2.15)$$

From here we can write the displacements as:

$$u_x = [i\xi(A \cos \alpha y + B \sin \alpha y) + \beta(-G \sin \beta y + H \cos \beta y)]e^{i(\xi x - \omega t)}$$

$$u_y = [\alpha(-A \sin \alpha y + B \cos \alpha y) - i\xi(G \cos \beta y + H \sin \beta y)]e^{i(\xi x - \omega t)} \qquad (2.16)$$

$$u_z = [-\beta(-C \sin \beta y + D \cos \beta y) + i\xi(E \cos \beta y + F \sin \beta y)]e^{i(\xi x - \omega t)}.$$

Now we have eight unknown coefficients, $A - H$. We apply the boundary conditions. For a traction free boundary three stresses on the surfaces of the plate vanish,

$$\sigma_{yy} = \sigma_{xy} = \sigma_{yz} = 0 \text{ at } y = \pm b. \qquad (2.17)$$

This gives six boundary condition equations, but we need two more for the system with eight unknowns, so we exploit the fact that $\nabla \cdot H = 0$, giving

$$\frac{\partial H_x}{\partial x} + \frac{\partial H_y}{\partial y} = 0 \text{ at } y = \pm b. \qquad (2.18)$$

14

The stresses from (2.2),

$$\sigma_{yy} = (\lambda + 2\mu)\frac{\partial u_y}{\partial y} + \lambda\frac{\partial u_x}{\partial x}$$

$$\sigma_{xy} = \mu\left(\frac{\partial u_y}{\partial x} + \lambda\frac{\partial u_x}{\partial y}\right) \tag{2.19}$$

$$\sigma_{yz} = \mu\frac{\partial u_z}{\partial y}$$

and requirement for the divergence of the vector potential to be zero form our system of eight homogeneous equations:

$$((\lambda + 2\mu)\alpha^2)(A\cos\alpha b + B\sin\alpha b) + 2\mu i\beta\xi(-G\sin\beta b + H\cos\beta b) = 0$$

$$((\lambda + 2\mu)\alpha^2)(A\cos\alpha b - B\sin\alpha b) + 2\mu i\beta\xi(G\sin\beta b + H\cos\beta b) = 0$$

$$\mu[2i\alpha\xi(-A\sin\alpha b + B\cos\alpha b) + (\xi^2 - \beta^2)(G\cos\beta b + H\sin\beta b)] = 0$$

$$\mu[2i\alpha\xi(A\sin\alpha b + B\cos\alpha b) + (\xi^2 - \beta^2)(G\cos\beta b - H\sin\beta b)] = 0$$

$$\mu[\beta^2(-C\cos\beta b + D\sin\beta b) + i\beta\xi(-E\sin\beta b + F\cos\beta b)] = 0 \tag{2.20}$$

$$\mu[\beta^2(C\cos\beta b - D\sin\beta b) + i\beta\xi(E\sin\beta b + F\cos\beta b)] = 0$$

$$i\xi(C\cos\beta b + D\sin\beta b) + \beta(-E\sin\beta b + F\cos\beta b) = 0$$

$$i\xi(C\cos\beta b - D\sin\beta b) + \beta(E\sin\beta b + F\cos\beta b) = 0$$

In order for a solution of this system with the coefficients $A - H$ to exist, we

15

require that the determinant of the coefficient matrix is zero.

$$
\begin{vmatrix}
c\cos\alpha b & c\sin\alpha b & 0 & 0 & -f\sin\beta b & f\cos\beta b & 0 & 0 \\
c\cos\alpha b & -c\sin\alpha b & 0 & 0 & f\sin\beta b & f\cos\beta b & 0 & 0 \\
0 & 0 & -h\sin\beta b & h\cos\beta b & 0 & 0 & \beta^2\cos\beta b & \beta^2\sin\beta b \\
0 & 0 & h\sin\beta b & h\cos\beta b & 0 & 0 & \beta^2\cos\beta b & -\beta^2\sin\beta b \\
-d\sin\alpha b & d\cos\alpha b & 0 & 0 & g\cos\beta b & g\sin\beta b & 0 & 0 \\
d\sin\alpha b & d\cos\alpha b & 0 & 0 & g\cos\beta b & -g\sin\beta b & 0 & 0 \\
0 & 0 & -\beta\sin\beta b & \beta\cos\beta b & 0 & 0 & i\xi\cos\beta b & i\xi\sin\beta b \\
0 & 0 & \beta\sin\beta b & \beta\cos\beta b & 0 & 0 & i\xi\cos\beta b & -i\xi\sin\beta b
\end{vmatrix} = 0
$$

(2.21)

where

$$
c = (\lambda + 2\mu)\alpha^2 + \lambda\xi^2, \quad d = 2i\xi\alpha, \quad f = 2i\mu\xi\beta, \quad g = \xi^2 - \beta,^2 \quad h = i\xi\beta
$$

Each of the eight columns is associated with the constants A, B, E, F, G, H, C, F respectively from left to right. By adding and subtracting the rows and columns, we see that the determinant can be written as the product of four sub-determinants,

$$
\begin{vmatrix} i\xi\cos\beta b & \beta\cos\beta b \\ \beta^2\cos\beta b & h\cos\beta b \end{vmatrix} \times \begin{vmatrix} -\beta\sin\beta b & i\xi\sin\beta b \\ h\sin\beta b & \beta^2\sin\beta b \end{vmatrix} \times \begin{vmatrix} c\cos\alpha b & f\cos\beta b \\ -d\sin\alpha b & g\sin\beta b \end{vmatrix} \times \begin{vmatrix} g\cos\beta b & d\cos\alpha b \\ f\sin\beta b & c\sin\alpha b \end{vmatrix} = 0,
$$

(2.22)

each of which may be zero individually. This gives 4 families of solutions where

pairs of coefficients do not vanish

$$I : A, B, D, E, G, H = 0 \quad C, F \neq 0 \tag{2.23}$$

$$II : A, B, C, F, G, H = 0 \quad D, E \neq 0 \tag{2.24}$$

$$III : B, C, D, E, F, G = 0 \quad A, H \neq 0 \tag{2.25}$$

$$IV : A, C, D, E, F, H = 0 \quad B, G \neq 0 \tag{2.26}$$

The solutions I and II correspond to SH plate wave modes that are discussed in detail in the texts by Achenbach [1], Auld [2], Graff [3] and Rose [4]. The solutions III and IV are the coupled L and SV waves in a plate usually referred to as Lamb waves. The displacements for the symmetric cases come from solution III:

$$u_x = (i\xi A \cos \alpha y + \beta H \cos \beta y)e^{i(\xi x - \omega t)} \tag{2.27}$$

$$u_y = -(\alpha A \sin \alpha y + \xi H \sin \beta y)e^{i(\xi x - \omega t)} \tag{2.28}$$

$$u_z = 0 \tag{2.29}$$

and the antisymmetric cases from solution IV:

$$u_x = (i\xi B \sin \alpha y - \beta G \sin \beta y)e^{i(\xi x - \omega t)} \tag{2.30}$$

$$u_y = (\alpha B \cos \alpha y - i\xi G \cos \beta y)e^{i(\xi x - \omega t)} \tag{2.31}$$

$$u_z = 0. \tag{2.32}$$

<div align="center">(a)   (b)</div>

Figure 2.2: Through thickness displacements of symmetric and antisymmetric Lamb wave modes

Lamb wave displacement solutions have frequency spectra:

$$Symmetric: \quad \frac{\tan \beta b}{\tan \alpha b} = -\frac{4\alpha\beta\xi^2}{(\xi^2 - \beta^2)^2} \tag{2.33}$$

$$Antisymmetric: \quad \frac{\tan \beta b}{\tan \alpha b} = -\frac{(\xi^2 - \beta^2)^2}{4\alpha\beta\xi^2}, \tag{2.34}$$

which are commonly referred to as the dispersion relations. The real solutions of these equations represent the propagating modes of the structure. The propagating symmetric modes bulge the thickness of the plate while the antisymmetric modes flex the plate back and forth (Figure 2.2). By conducting a root finding algorithm for various frequency thickness products we can produce the dispersion curves for the structure from these equations. The dispersion curves relate the phase velocity of the modes to the frequency thickness product of the structure (Figure 2.3a). The group velocity of the modes is then derived through

$$c_g = c_p^2 \left[c_p - (fb)\frac{dc_p}{d(fb)} \right]^{-1} \tag{2.35}$$

to give the group velocity dispersion curves found in figure 2.3b. There are an infinite number of modes generated for higher frequency thickness products, although each of the modes, excluding the S0 and A0, has a cutoff frequency. At this cutoff frequency the phase velocity of the mode approaches infinity while the

<div align="center">18</div>
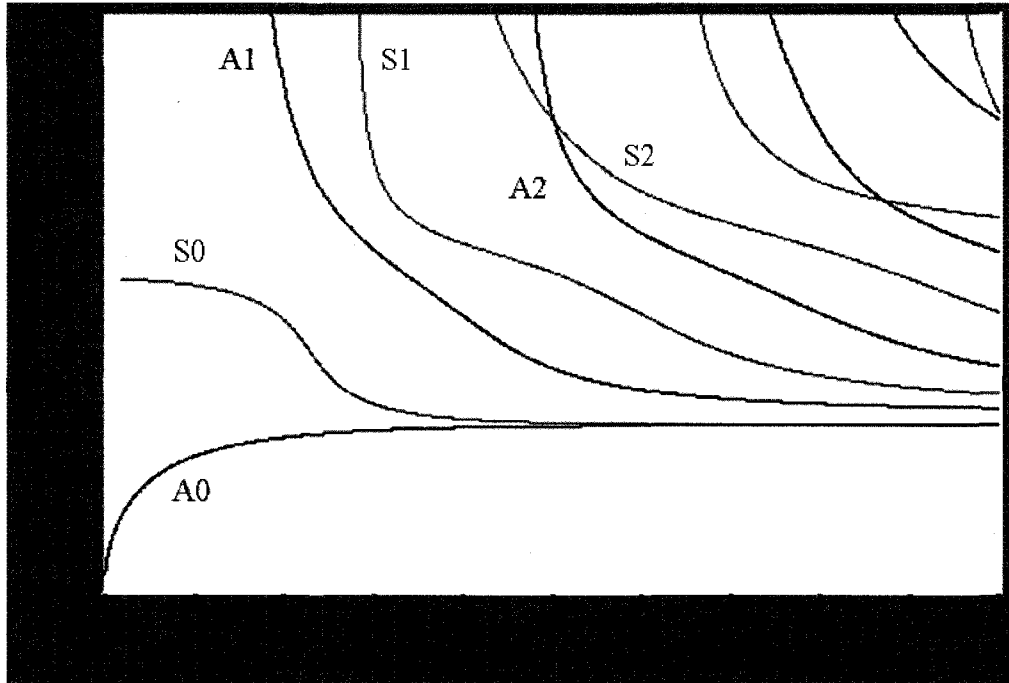
(a)
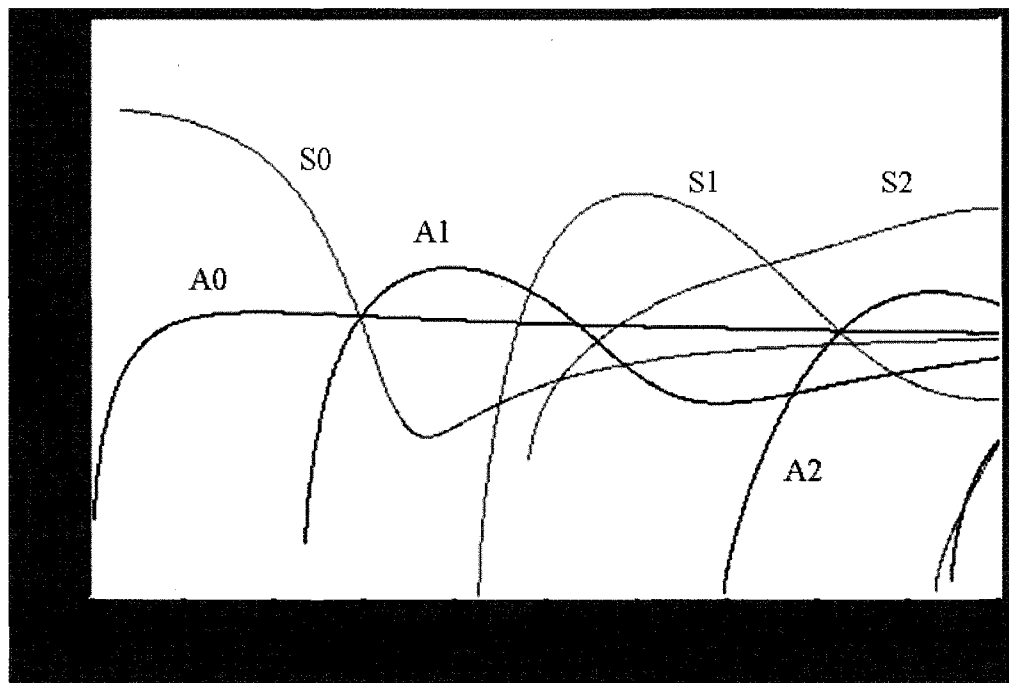
(b)

Figure 2.3: Phase (a) and group (b) velocity dispersion curves for aluminum. Symmetric modes are shown in red, anti-symettric in blue.

19

group velocity approaches zero.

The number of propagating modes in the structure is therefore determined by the frequency thickness product and the way in which the waves are generated. The dispersive properties of the generated modes allow us to gain information about the structure as they propagate. With a known starting thickness we can choose an excitation frequency that generates a highly dispersive mode. Therefore any change in thickness or material properties will translate to a change of propagating group velocity. From the dispersion curve (Figure 2.4), if we have a 3.3 mm thick sample, excited with a 1 MHz pulse we would expect to see 3 propagating modes, the A1, A0 and S0. Then with an introduction of a small thinning of the plate we would expect the A1 mode to slow down, the S0 mode to speed up, and the A0 mode to remain at the same velocity. In this way we use the dispersive nature of the guided waves to design NDE tests to interrogate structures for flaws.

2.2 Experimental Techniques

The theory of the guided waves tells us what kind of waves we should expect to see propagating through the structures, but the laboratory equipment dictates the actual signals generated. In our lab we concentrate on using computer based systems to excite the ultrasonic waves. The apparatus was a computer controlled pulser that sends out a time varying voltage pulse to the transmitting transducer which converts the pulse into mechanical energy hitting the surface of test sample. The surface vibrates accordingly. After the waves propagate throughout the piece, the receiver then translates the vibrations back into voltage that is then sampled
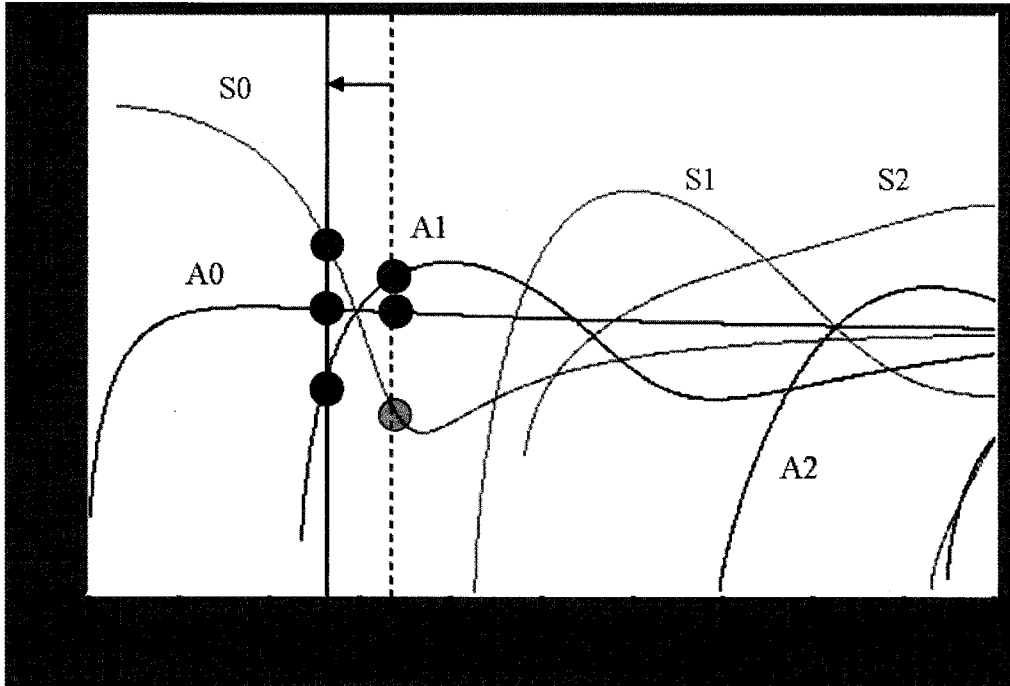
Figure 2.4: For a 3.3 mm thick sample excited at 1 MHz there are 3 propagating Lamb wave modes the A1, A0 and S0. As they propagate through are thinned region the A1 will slow down, the S1 will speed up and the A0 would have the same group velocity. The changes in velocity correspond to changes in arrival times of the modes, so we can use the mode arrival to determine quantitative features of the physical structure.
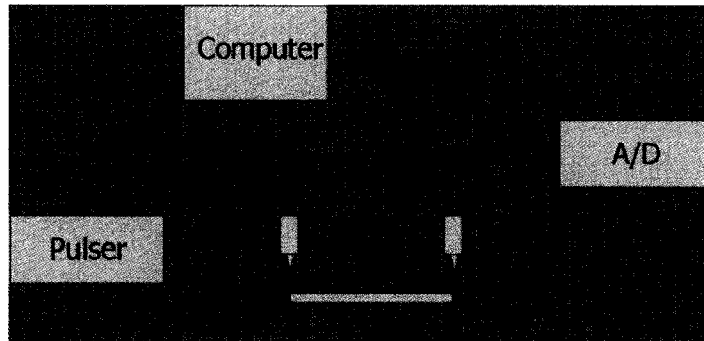
Figure 2.5: Experimental setup block diagram, the computer controlled pulser sends a voltage pulse to the transmitting transducer which excites the guided waves in the sample, the receiving transducer then translates the plate vibrations back to voltage changes that are then sampled by the A/D converter and stored in the computer.

and recorded by an analog to digital (A/D) converter (Figure 2.5). In this section we will discuss some of the considerations for choosing equipment for a particular application.

2.2.1 Pulsers

In this work we make use of three different pulsers that have advantages in different areas. First we consider a Matec TB1000 tone-burst plug-in card. This is a full-sized card that plugs directly into a rack-mount computer accompanied by a separate A/D card. This instrument will generate a sinusoidal tone burst of a chosen frequency in the range of 50 kHz to 20 MHz. The user has the ability to choose the frequency and pulse length through the use of a graphical user interface. The separate A/D card allows for the user to also pick the sampling frequency. This setup is very versatile in that we can choose exactly what frequency at which we wish to excite the transducers, pinpointing our desired location along the dispersion curves. It can also be used with a wide range of applications because

the allowable frequency range is broad. One limitation is that the voltage power is in the 200-300 V range. This means that we can't propagate very long distances. For such purposes we employ a second, high powered pulser. This apparatus is fundamentally similar to the TB1000. We can choose the desired frequency for the sinusoidal tone and it has a separate A/D card but due to the fact that the high power the electronics are much bigger in size, they have to be housed in a separate box from the computer. The higher powered box is also capable of producing low frequencies. This is very useful because in practice, we usually use lower frequencies to propagate in thicker samples for longer distances. This keeps the frequency thickness product low enough that a manageable number of dispersive modes are generated. For the research here we employed two different high-powered pulsers, one commercially made by Ritec Inc., the RPR-4000 with RT-150 (a 150 Ω load resister), and the other developed in our lab. The Ritec pulser features an 8 kW tone burst at up to 0.8% duty cycle, with a measured max of 2000 V peak to peak over the frequency range of .25 to 2 MHz. The pulser developed in our lab for rugged on site tests was modeled after the specifications of the Ritec pulser. On the other end of the spectrum is our third pulser, the nanopulser 3 (np3). This is a handheld device that contains its own A/D board and connects via an USB cable to a laptop. Due to the miniaturization of the electronics, some of the capabilities are more limited but nonetheless useful. Here instead of a tone excitation, the np3 performs a spike excitation that falls off in a few nanoseconds. This spike excitation then relies on the resonant frequency of the transducers in order to determine the generated ultrasonic waves.

All three of these devices excite voltage pulses of short duration that are then translated via the transducers to the test specimen as ultrasonic vibrations.

2.2.2 Transducers

The transducers are very important in the generation of the ultrasonic signals. Depending on crystal orientation and structure, we can control the properties of the waves we generate. We typically use piezoelectric transducers which consist of a crystal, matching layer and electrical leads. When hit with a voltage pulse, the crystal responds by expanding along a lattice direction. The matching layer transmits this vibration to the test specimen either through direct contact, an angle block or a focusing lens. In all three cases the transducer must be coupled to the surface, in our lab we typically use water. For contact and angle block transduction, the coupling water is just a thin film on the surface, but with the focusing transducers the water path is the focal path of the lens, usually 1" to 2".

The crystal structure and orientation dictate the waves that are generated. The thickness gives the resonant frequency of the vibration. If the expansion axis is normal to the surface of the transducer it is called a longitudinal transducer, otherwise it is a shear transducer. Longitudinal transducers are omnidirectional while shear transducers can either be aligned parallel to the direction of propagation, called shear vertical (SV), or perpendicular, called shear horizontal (SH). In this work we will give examples using longitudinal and SV transducers.

These transducers generate multiple modes in the test piece depending on its material properties. But if we wish to limit the number of modes generated in a test piece to simplify the signal we can do so by using an angle block to choose the particular modes according to Snell's law.

$$v_{p,material} = \frac{v_{l,wedge}}{\sin\theta} \tag{2.36}$$

24

Here the longitudinal velocity of sound in the angle block, $v_{l,wedge}$, and the angle of the wedge, θ, determine which modes are transmitted into the test material given by its phase velocity $v_{p,material}$. The other modes with different phase velocities are reflected off the surface and absorbed in the angle block.

We choose the frequency of transducer and coupling method for each individual application depending on the physical requirements of the detection system. For instance, for aircraft structural health monitoring (SHM) applications weight is a large concern so we use smaller transducers that are higher in frequency in direct contact with the structure to eliminate any extra materials. For tests in an underwater environment, the coupling fluid is already present so we can use an focusing lens or angle beam approach to simplify the signals.

2.3   Signal Processing

For our computer based systems we have written and implemented Matlab graphical user interfaces in order to operate each of our apparatus. Once we have recorded signals we can employ our signal processing techniques. Our philosophy is to excite complicated signals in order to keep all of the time series information, then post-process the waveforms to extract the most useful information about the modes of interest. This work concentrates on using the Dynamic Wavelet Fingerprinting Technique (DWFT) in order to accomplish this. The DWFT implemented here relies on filtering the data with a discrete stationary wavelet filter to remove a few layers of detail then passing the filtered signal through the fingerprinting algorithm.

2.3.1 Filtering with Wavelets

Wavelets are a very useful tool for analyzing time series data [55]. The wavelet transform allows us to keep track of both time and frequency, or scale features. Whereas Fourier transforms break down a signal into a series of sines and cosines in order to identify the frequency content of the entire signal, wavelet transforms keep track of local frequency features in the time domain. The difference arises from the use of basis functions called wavelets to represent the signal through translations and dilations of a mother wavelet. The mother wavelet is any square-integrable function of finite energy that is scaled by stretching and compression (dilation), compared to original signal then shifted in time (translated) for the next comparisons. We find the set of wavelets from the mother wavelet $\Psi(t)$ in this fashion:

$$\Psi_{s,\tau}(t) = \frac{1}{\sqrt{s}}\Psi\left(\frac{t-\tau}{s}\right),\qquad(2.37)$$

where s is the scale factor and τ is the translation factor and the factor $s^{-1/2}$ takes care of energy normalization across the different scales.

There are two classifications for wavelet transforms, the discrete wavelet transforms (DWT) and continuous wavelet transforms (CWT). The CWT uses every possible scale and translation whereas the DWT acts on a specific subset of scale and translation values. The CWT of a signal $f(t)$ is defined as

$$W(s,\tau) \equiv \int\limits_{-\infty}^{\infty} f(t)\Psi_{s,\tau}^{*}(t)dt \qquad(2.38)$$

where $*$ denotes the complex conjugation. The wavelet transform $W(s,\tau)$ can be thought of as a function of τ at a fixed value of s, it represents the detail contained

26

Figure 2.6: As the wavelet is dilated in the time domain, the resulting frequency spectra band together to form a band-pass filter bank.

in the signal $f(t)$ at the scale s [65].

Since $\Psi(t)$ is square-integrable, and its Fourier transform $\hat{\Psi}(\omega)$ is continuous, $\hat{\Psi}(\omega)$ must decay as $|\omega| \to \infty$ and as $\omega \to 0$. If this decay is rapid, then $\hat{\Psi}(\omega)$ will be small outside of a frequency band. We also know that a compression of the wavelet in the time domain corresponds to a stretch and shift of its frequency spectrum.

$$\Psi(t) \to \hat{\Psi}(\omega) \qquad \Psi(at) \to \frac{1}{|a|}\hat{\Psi}(\frac{\omega}{a})$$

This then leads to being able to think of a single wavelet as a band-pass filter and a series of dilated wavelets as a band-pass filter bank as seen in Figure 2.6. An infinite number of wavelets are needed in order to cover the entire frequency spectrum down to $\omega = 0$ since every time the wavelet is stretched in the time domain by a factor of 2, its bandwidth is halved. In practice, we introduce a scaling function, $\Phi(t)$ that has a low-pass spectra in order to reduce the number of wavelets needed. The scaling function covers the spectrum from $\omega = 0$ to the band-pass filter of a chosen wavelet scale (Figure 2.7). The wavelet is fully defined by the wavelet function $\Psi(t)$ and the scaling function $\Phi(t)$, figure 2.8 shows the Coiflet wavelet, order 5, defined by its scaling and wavelet functions with their resulting finite impulse response filters.
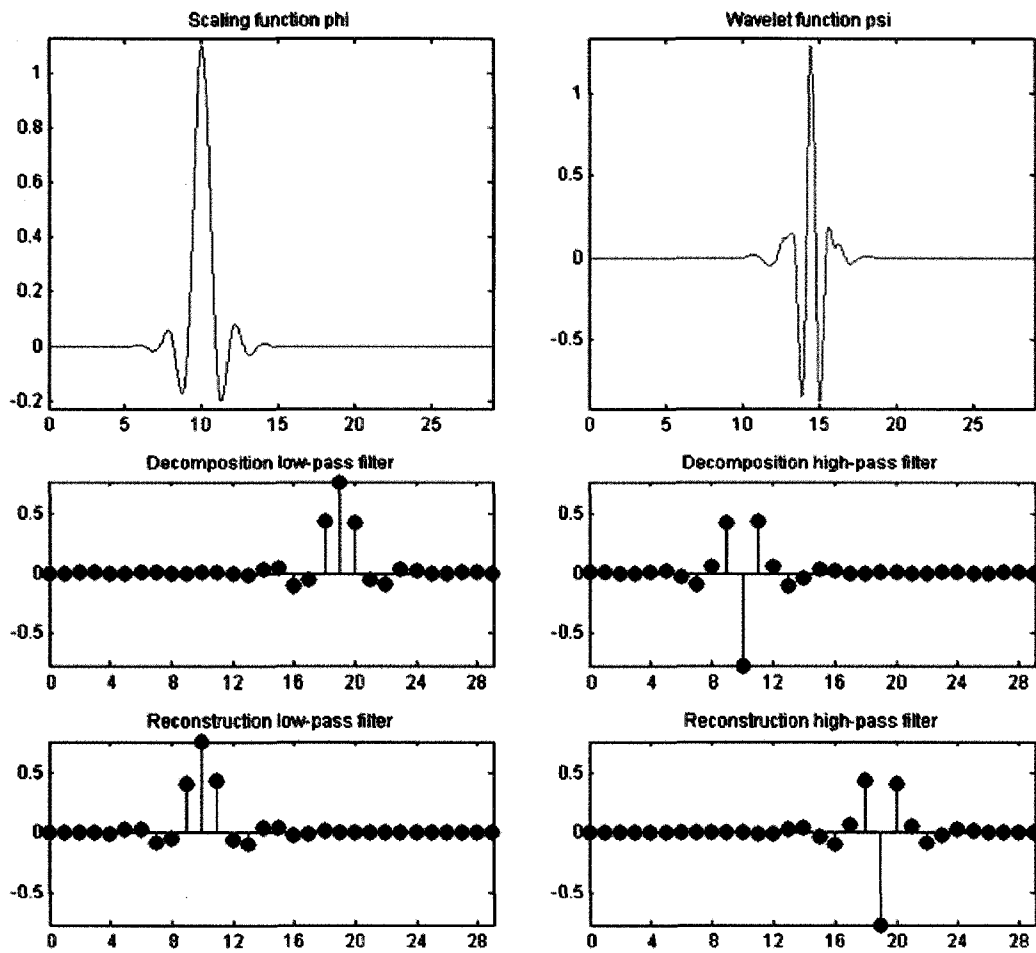
Figure 2.7: The spectrum of the scaling function $\Phi(\omega)$ is a low-pass filter that reduces the number of wavelets needed to cover the spectrum of the signal.
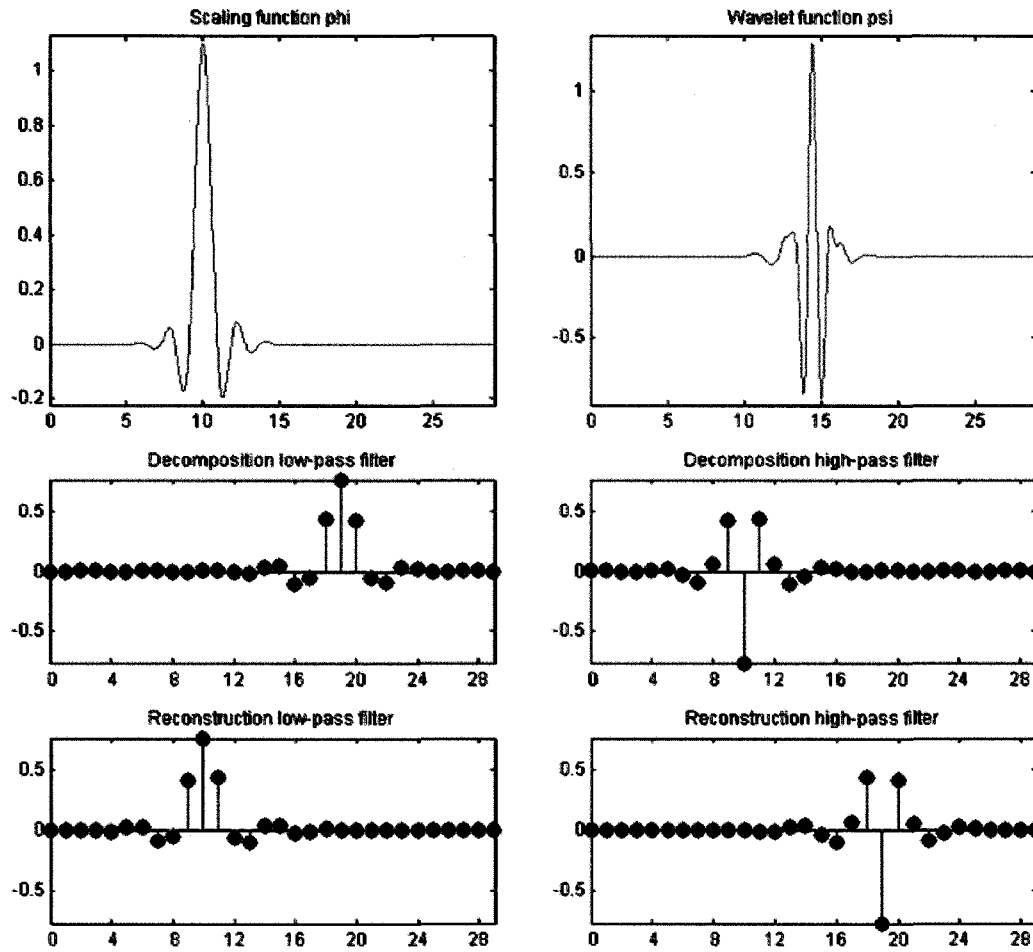
Figure 2.8: The 5th order Coiflet wavelet is completely defined by the scaling function, $\Phi(t)$ (left), and the wavelet function, $\Psi(t)$ (right). The resulting FIR filters that are used in the DWT and IDWT are also depicted.

With a discrete number of scales needed to transform the signal we can formulate the DWT as the implementation of a wavelet and scaling function filter bank. The decomposition low-pass filter given by the scaling function reveals the lower frequency approximations of the signal, while the high-pass filter from the wavelet function gives the high-frequency details. Without subsampling, the wavelet transform is time-invariant and is referred to as a stationary discrete wavelet transform (SWT). Figure 2.9 shows how the SWT splits the signal into low and high frequency components for multiple levels.

In general most of the information in a signal is contained in the approximations of the first few levels of the SWT. The details of these low levels have mostly high frequency noise information. If we set the details of these first few levels to zero, when we reconstruct the signal with the inverse SWT we have effectively de-noised our signal to keep just information of the Lamb wave modes of interest.

2.3.2 Dynamic Wavelet Fingerprinting Tecnique

The next step in our signal processing is to pass the filtered signal through the DWFT. Previous work by Hou [23] and Leonard [18] has developed the DWFT for the processing of ultrasonic signals. Here we will briefly show how this technique has been implemented for our purposes. We start with the filtered ultrasonic signal and take the continuous wavelet transform. Figure 2.10 shows a simple example of a test ultrasonic pulse going through the DWFT. The CWT gives a surface of wavelet coefficients, this surface is then normalized between [0-1]. Then we perform a thick contour slice operation. The user defines the number of slices to use, the more slices, the thinner the contour slice. The contour slices are given the value of 0 or 1 in alternating fashion. They are then projected down to
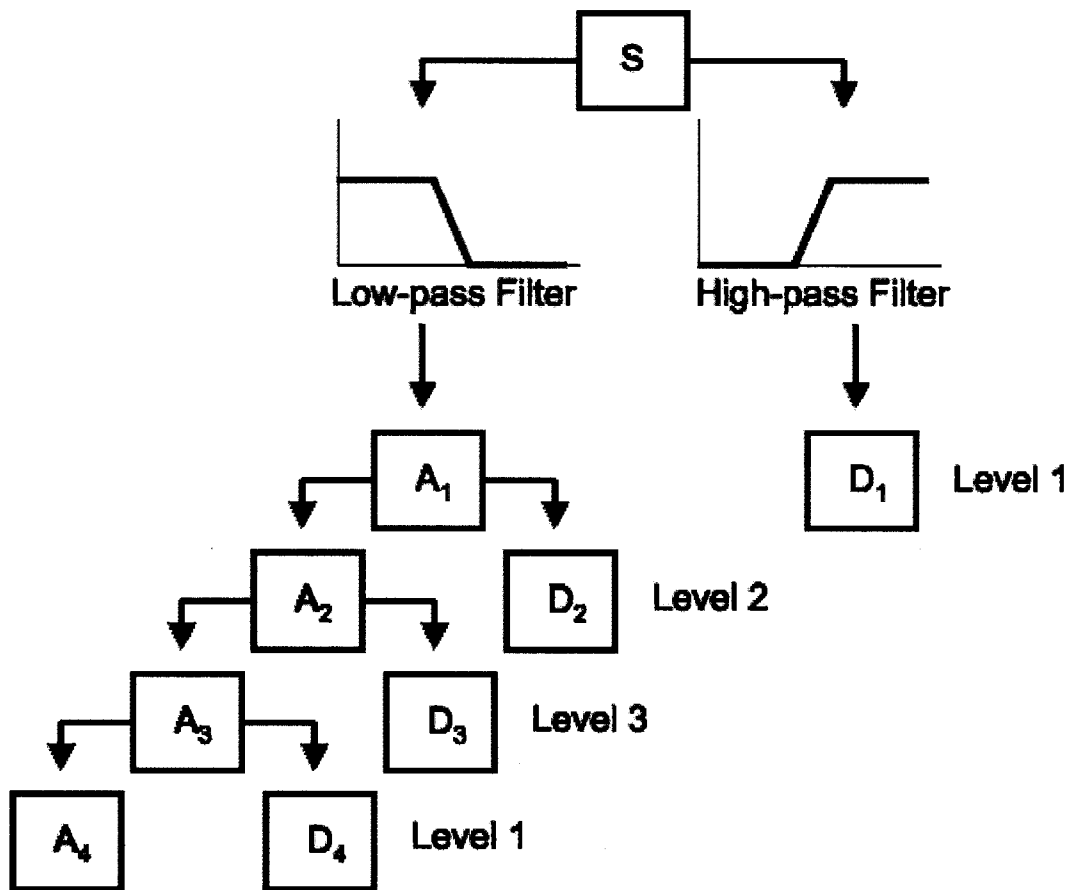
Figure 2.9: The SWT uses the low-pass filter from the scaling function and the high-pass filter of the wavelet function in order to split the signal into low frequency components (approximations) and high frequency components (details).
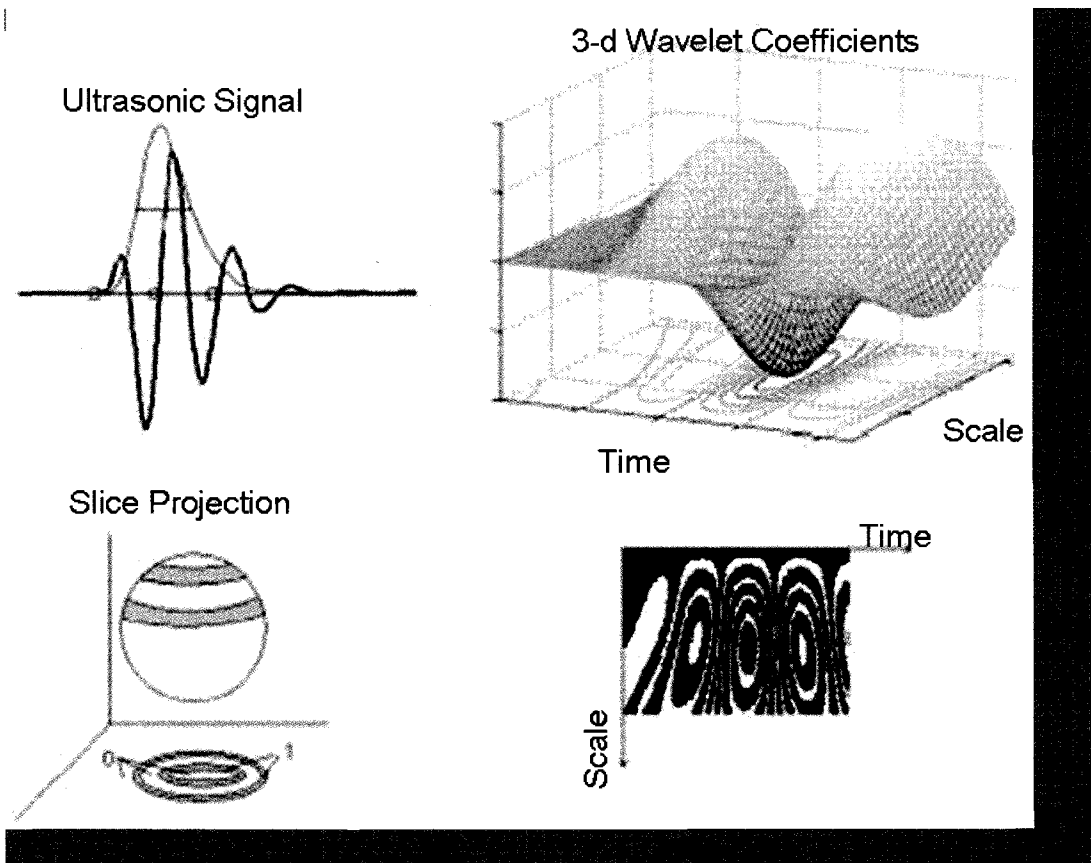
Figure 2.10: The DWFT takes an ultrasonic test pulse (upper left) preforms a CWT to obtain the wavelet coefficients that form the surface (upper right). This surface is then normalized between [0-1] and a slicing operation is performed (lower left). The slices are then projected down onto a 2D black and white image (lower right). (Figure from Hou [23]).

a 2D image where the result often looks remarkably like the ridges of a human fingerprint.

The problem has now been transformed from 1-dimensional signal identification problem to a 2D image recognition scenario. The power of the DWFT is that it reduces the time-series data into a binary matrix that is easily stored and transfered. There is also a robustness to the algorithm, since different mother wavelets emphasize different features in the signals. For the most part in the research we've manually chosen the mother wavelet based on experience and using wavelets roughly shaped like the excitation pulses.

The last piece of the DWFT is the image recognition of the binary features that correspond to the modes of interest. We have found that different modes are represented in unique features in our applications. In the next chapter we discuss the implementation of the DWFT to signals from mass loadings on ship hulls, delaminations under pipe coatings and corrosion on the surface of aircraft stringers. The fingerprints from each of these has its own meaningful representation but we've found that using a simple ridge counting algorithm on the 2D images is a helpful way to identify some of the features of interest. Once a feature has been identified in the time scale space we have determined its arrival in the time domain as well and we can draw conclusions based on our knowledge of the guided wave theory.

Chapter 3

NDE Applications

Thus far we have introduced the principles of ultrasonic guided waves and have shown how we can use the signal processing to automatically extract information from the complicated waveforms. In this chapter we apply these techniques to three diverse real world applications. Complex geometries of engineered structures make subtle abnormalities difficult to identify via traditional inspection methods. The structures are either hard or expensive to get to or dangerous to examine in person. Guided waves follow the intricacies of the structures so the can be inspected intact without the added expense of downtime in many cases. The scenarios that we present here are our efforts toward developing techniques to examine ship hulls for attached limpet mines, to identify and characterize adhesion of coatings on large diameter pipes, and to find corrosion and thinning flaws on aircraft stringers.

3.1 Ship Hulls

The US Navy has many large ships in hostile waters, and is concerned about the security of these vessels including their large underwater ship hulls. Of particular concern are limpet mines on the ship hull under the water line. One of the precautions that the Navy takes is to secure a perimeter around the ship on the water's surface at all times, however this still leaves the possibility of an underwater approach by a swimmer. To counter this manner of attack, the Explosive Ordinance Disposal (EOD) department of the Navy employs its own human divers and mammals that search the hulls for mines. This is dangerous and inefficient for the divers. The hulls are too large to completely check by hand and there is often little to no visibility due to turbid waters requiring close proximity which further endangers the diver. We describe here our preliminary efforts for designing an autonomous robotic, guided wave ultrasonic system to systematically search for magnetically attached limpet mines under the waterline of ships. This project is named REMORA (**R**obotic **E**xamination for **M**ines **O**n hulls using **R**ayleigh-Lamb **A**coustic waves. A remora is a suckerfish that attaches itself to the body of large mammals, sharks and boats, here we envision an autonomous robotic inspection system for limpet mine detection.

In this approach robots carrying ultrasonic sensors crawl along the ship hull at about the water line, sending out high power acoustic signals that are guided along the hull surface and then received by a sensor on another robot. In order for the guided waves to be perturbed by the attached mine, the guided waves have to be sensitive to a mass loading on the surface of the hull. By carefully choosing the excitation parameters we can specify a frequency thickness product that positions the measurement on the shoulder of a very dispersive mode. This means that

even a small mass loading compared to the size of the ship hull would slightly alter the local propagation parameters and thus translate to a detectable shift along the dispersion curve. A small increase in the frequency thickness product change triggers a larger change in the propagation velocity.

But first we have to generate the appropriate guided waves and make sure that they are propagating through the ship hull. Ship hulls are fairly thick compared to pipe walls and aircraft structures. This means that our normal philosophy of exciting mutli-mode signals and separating them out afterwards is even more complicated because of the number of higher-modes generated. So instead we took an angle block approach to this problem. We know from equation (2.36) that we can choose particular propagating modes by exciting the waves at an angle to the surface of the hull. In order to characterize the behavior of the guided wave modes in the presence of a magnetic mass loading, we did preliminary test on a quarter sized destroyer hull at the Aberdeen Army Testing Center in Maryland. Then we performed in-situ tests on the Del Monte cargo ship, in the water at the Little Creek Amphibious Base in Virginia.

3.1.1   Aberdeen Preliminary Testing

We obtained access to a quarter sized DDG-1000 destroyer hull at the test site for 3 days. The destroyer hull had been cut into three sections and placed in dry dock. We performed our testing on the mid and stern sections of the destroyer, the bow section of the ship was not available due to it previously having been used for explosives testing by the EOD. We have included rough schematics of the middle and stern hull sections that we preformed tests on (Figure 3.1).

The aim of the project was to identify the appropriate scheme for detecting
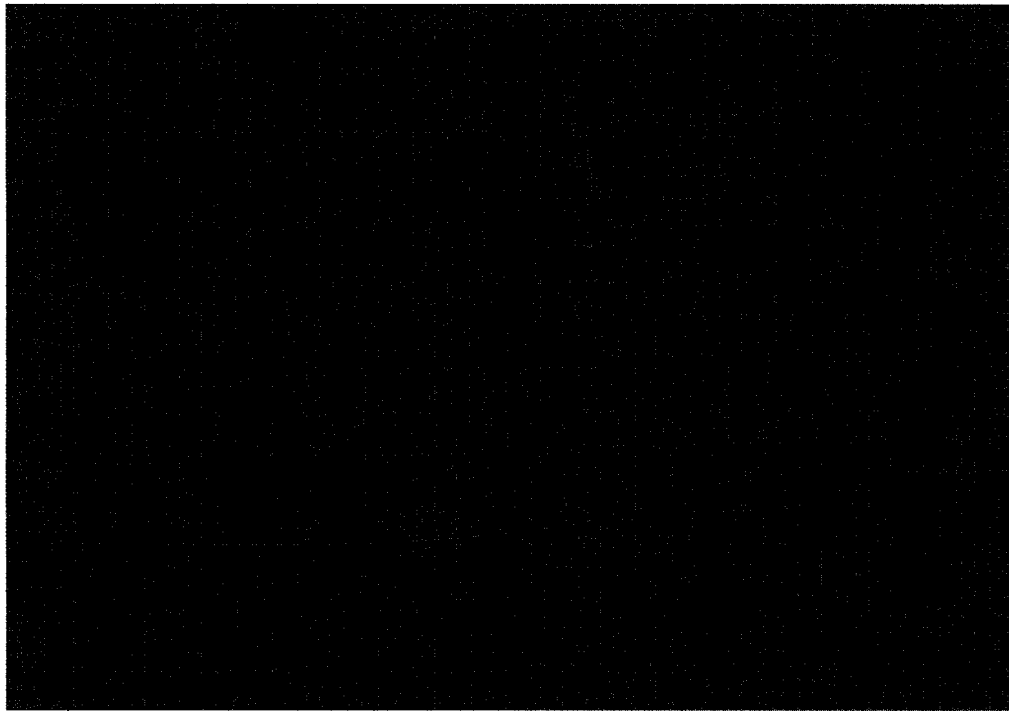
(a) Destroyer mid section.
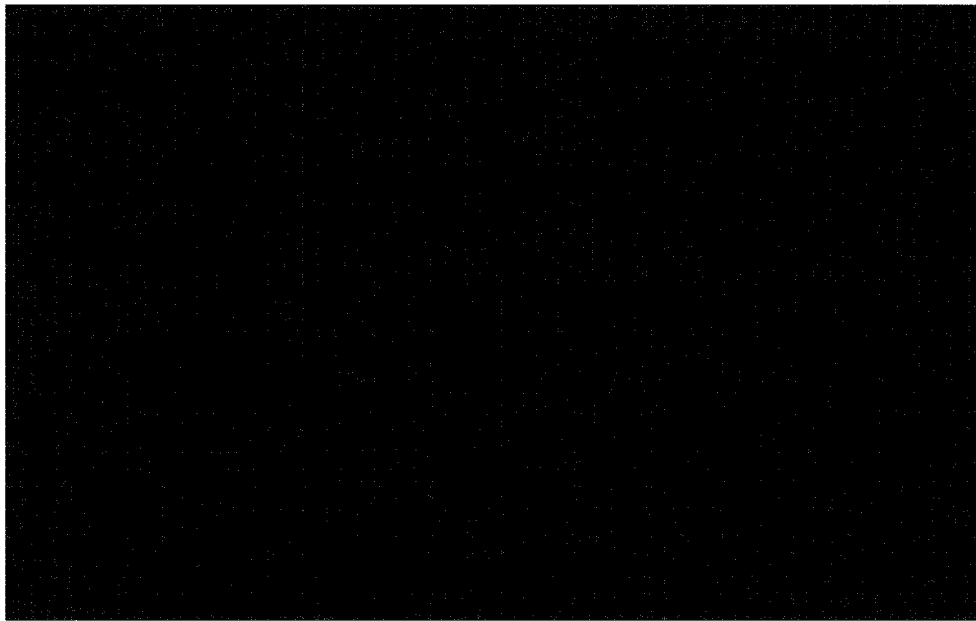
(b) Destroyer stern section.

Figure 3.1: Schematics for the test location in the mid and stern sections of the quarter scale destroyer in dry dock. In the stern section figure the location letters in parentheses indicate the corresponding hull location on the other side of the keel.
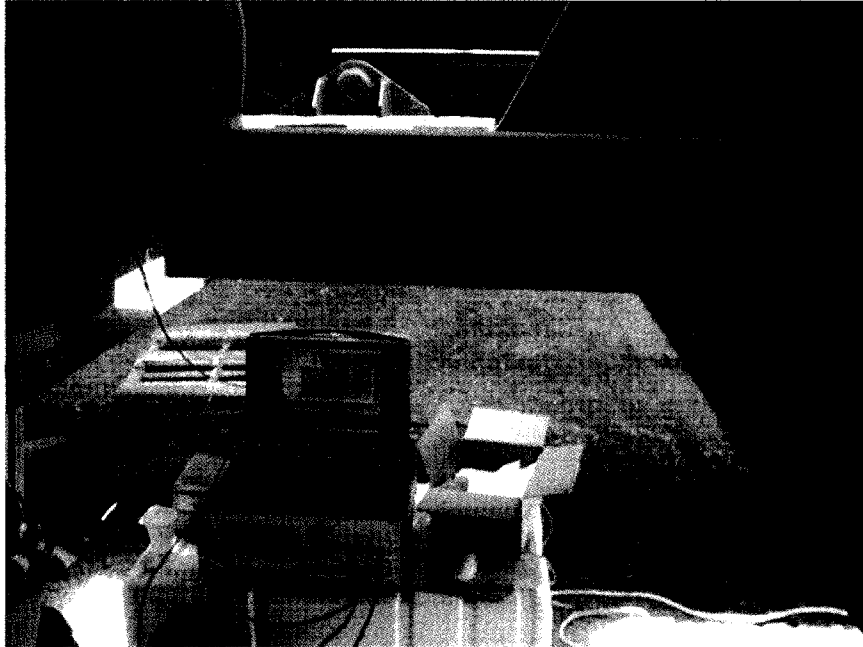
Figure 3.2: Portable Dolch lunch box computer atop of the high powered Ritech RPR-4000 pulser/receiver on site under the quarter scale destroyer hull in dry dock at the Aberdeen Army Testing Center in Maryland.

and locating a mock mine placed on the underside of the hull. Our mock mine consisted of a 5 pound weight and four toroidal magnets. The test apparatus was a high powered pulser/receiver from Ritec Inc. along with a Gage analog to digital card in a portable PC. Figure 3.2 shows a picture of the equipment setup under the ship hull in dry dock.

By examining the dispersion curves for steel (figure 3.3) we chose our frequency thickness product. The quarter scale ship hull is made from 5/16" steel panels welded together. We chose a excitation frequency of 500 kHz in order to be on the shoulder of the first order symmetric mode (S1). This gives a frequency thickness product of 3.988 MHz-mm and the fastest mode should have the velocity of 4.8 mm/μs. On site, we chose to use a 30° angle block to excite the S1 mode, which
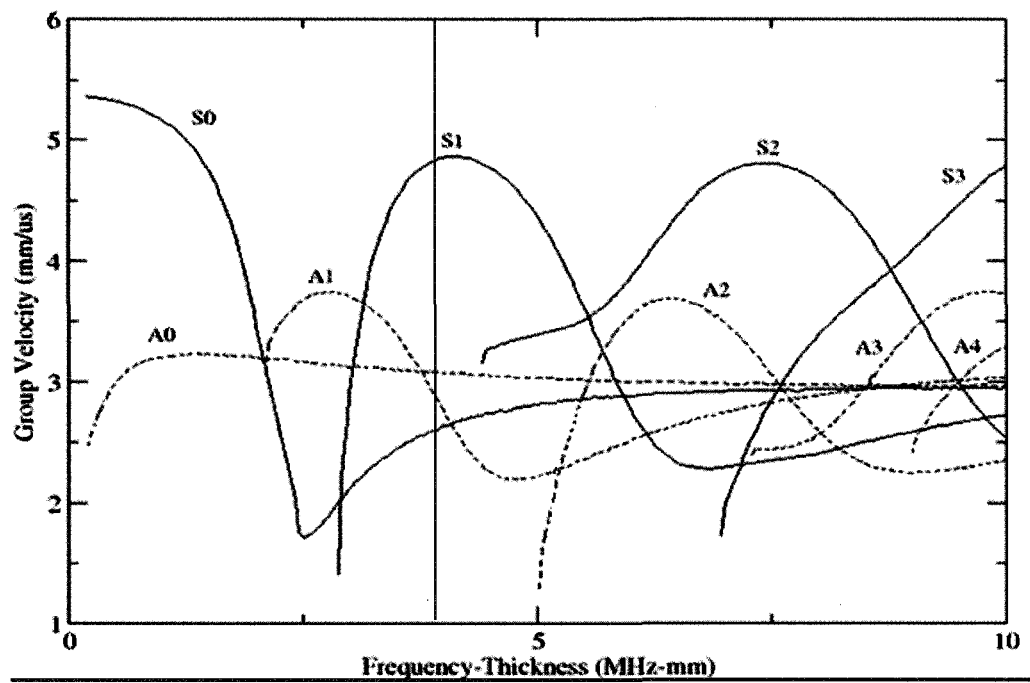
Figure 3.3: Steel dispersion curve where the red line indicates the frequency thickness product of 3.988 MHz-mm using a 500 kHz transducer on a 5/16" steel hull.

39

is close to the desired 27.1° derived from Snell's law.

Here we will present some of the results from these tests that were used to help develop a technique for identifying the presence of the mock mine in the signals. For Test 1 we took baseline measurements without the mine present for many pitch-catch positions of increasing distances down the midsection of the hull as well as the corresponding measurements with the mock mine present. The receiver was placed on the mid line of the hull (point A in Figure 3.1a) while the transmitter was moved out towards the sides of the ship. The transmitter was placed at points C, F, H and I of the midsection for evaluation. Figure 3.4 shows the raw waveforms that were collected for each of these positions without the presence of the mock mine. The red and blue dotted vertical lines in each of the waveforms indicate the expected arrival of each of the guided wave modes, S1, A0, A1, S0 from left to right respectively.

It is difficult to extract the first arriving mode so we employed filtering. Figure 3.5 shows the same waveforms after being passed through a Fourier filter to remove some high frequency noise. Although this technique is useful to determine the frequency content and remove some of the noise in the signals it doesn't really gain us any information about the guided wave modes that we care about. Instead pass the signal through a SWT filter to remove some layers of detail (Figure 3.6) to better distinguish the modes. The filter made use of the 'coif3' mother wavelet and removed the first four layers of detail. In this instance we can start to see the presence of the first arriving S1 mode. Since we are concentrating on the first arriving mode we chose to window the signal around this mode for closer examination. This was done by taking the expected arrival of the S1 and then counting to the left 500 points for the start of the window and then used a window
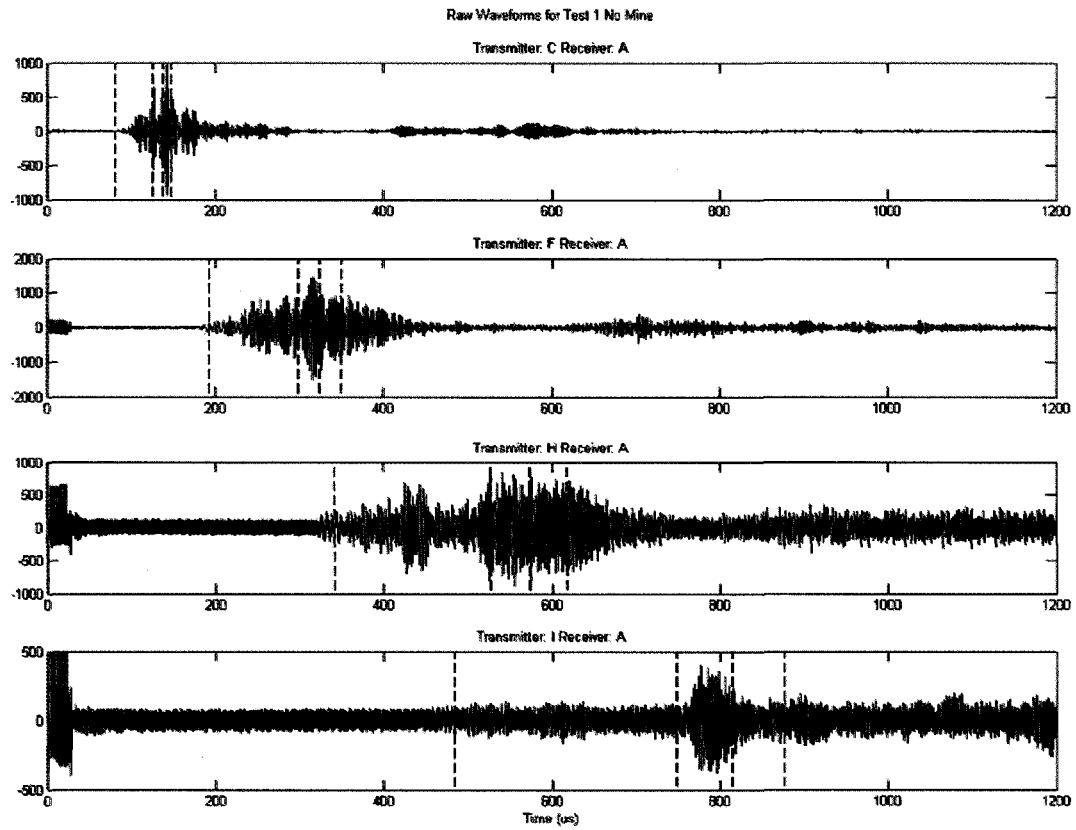
Figure 3.4: Raw waveforms collected at 25 MHz using 500 kHz transducer with 30° angle block for increasing lengths down the hull towards the keel. Transmitter placed at locations C, D, E and F with receiver remaining at point A for propagation distances of 15.5", 36.5", 64.5", 91.5" respectively. The dotted vertical lines show the expected arrivals of the S1, A0, A1 and S0 guided wave modes.

41
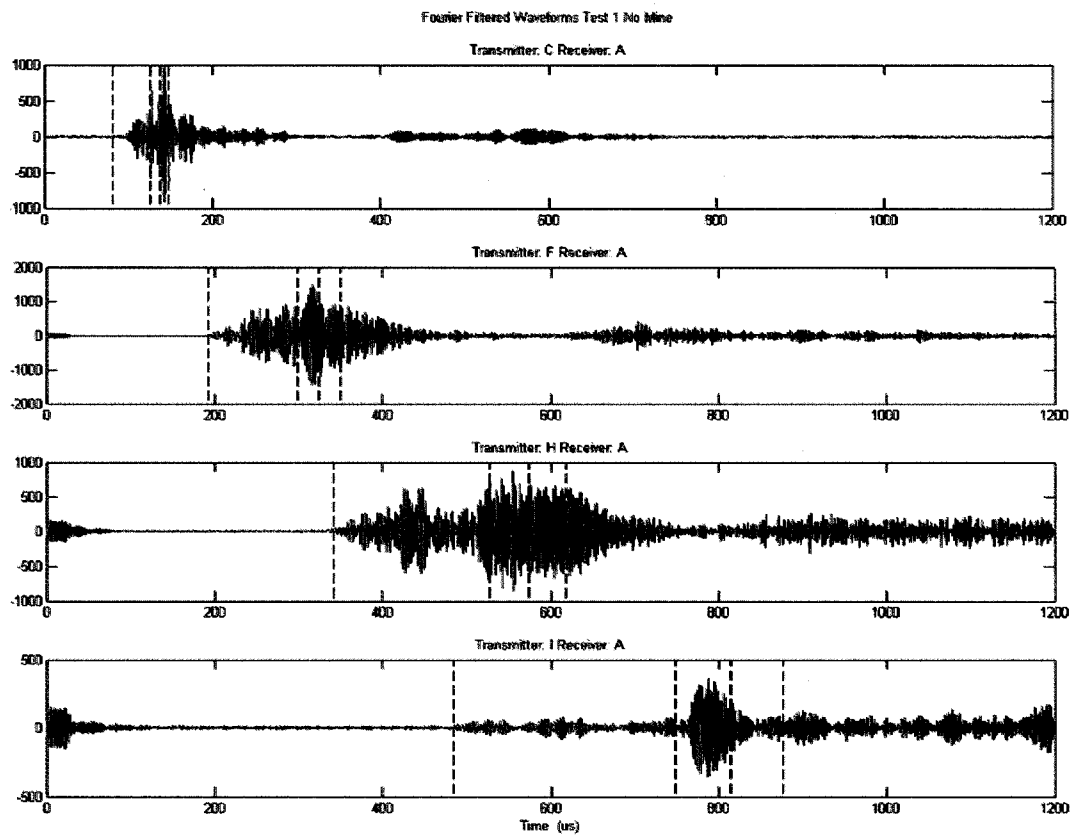
Figure 3.5: Fourier filtered waveforms from 3.4
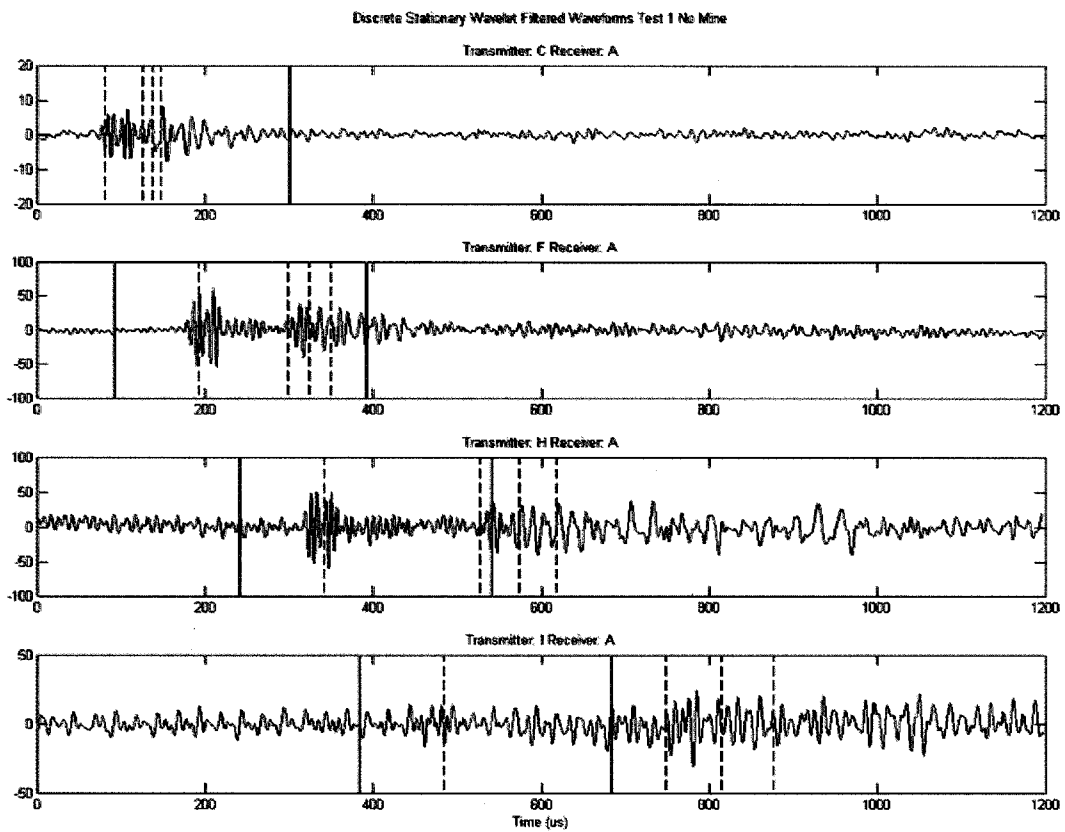
Figure 3.6: Discrete stationary wavelet filtered waveforms from 3.4
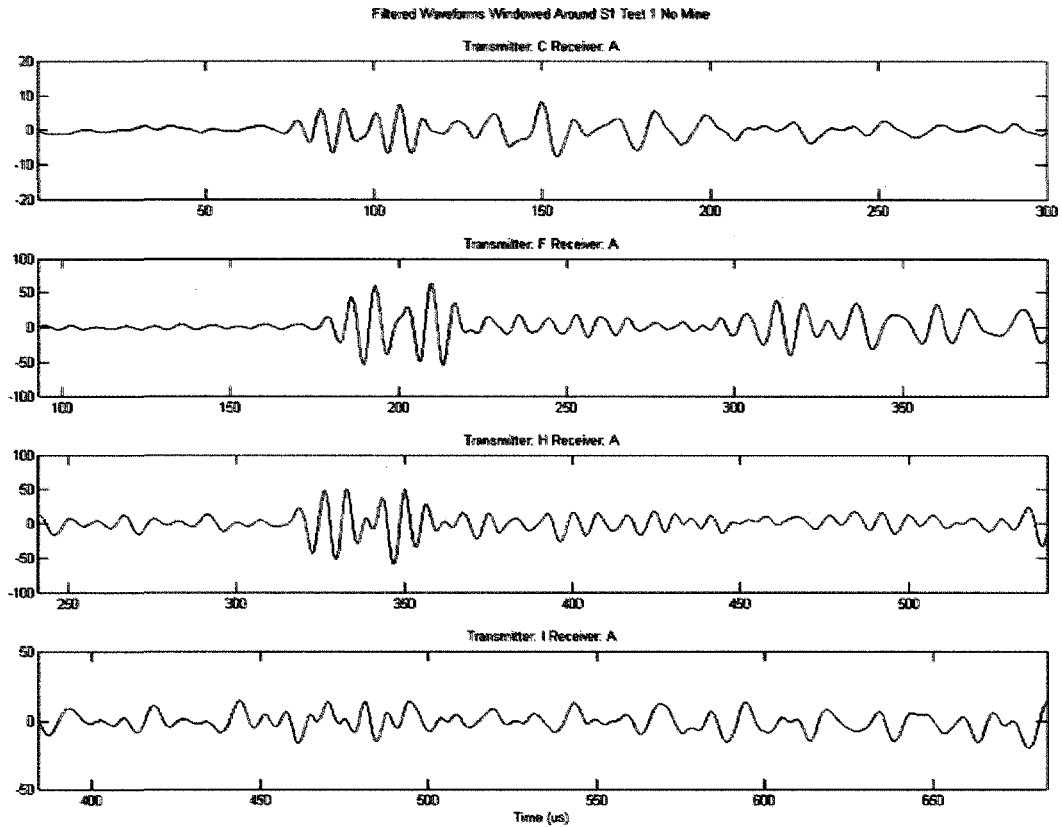
Figure 3.7: Window of discrete stationary wavelet filtered waveforms from 3.4. Window was determined back counting backwards from the expected arrival time of the S1 mode.

width of 1500 points. This window is shown in figure 3.6 between the vertical black lines. Figure 3.7 shows just the windowed portion of the filtered signal that contains the S1 mode. In order to present the data in a clearer format, we pass the windowed, filtered signals through our DWFT. Figure 3.8 shows the resulting thumb prints from the transmitter location progression without the mock mine present. The DWFT used the 'mexh' mother wavelet for 50 levels in obtaining the wavelet coefficients, then sliced the surface in 10 thick contours of width .05. We chose this combination of settings for the DWFT because of the emergence of

44
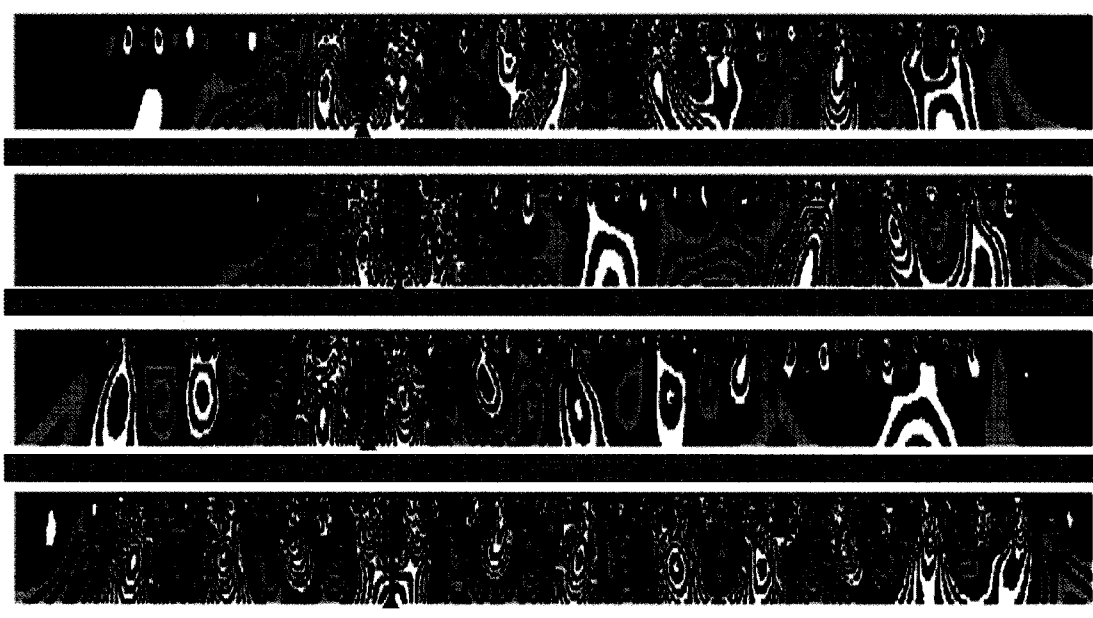
Figure 3.8: DWFT thumb prints generated from the data collected in test 1 without the presence of the mock mine for increasing propagation distances. The vertical solid red lines indicate the arrival of the mode of interest the S1.

the circular gray feature that corresponds to the S1 mode. In figure 3.8 the center of this feature has been indicated by a vertical solid red line. The next challenge was to compare signals with and without the mock mine to see if we could identify the mass loading on the hull.

We took measurements with the mock mine in multiple positions in order to determine if mine placement mattered in the signals. We kept track of four different mine placements for the four different propagation distances. Looking back to figure 3.1a we can see the four possible mine placements at points B, D, E, and G. This gave a variety of scenarios for the mine, close to the receiver, close to the transmitter, on a stringer and in the middle of a span between the transducers. The shorter propagation distance tests don't include all of the mine placements because the mine would be outside of the propagation interval. Each of

Figure 3.9: The thumb prints resulting from the DWFT on data collected from the shortest propagation distance of 15.5" without (top) and with (bottom) the mock mine placed at position B in 3.1a. The vertical red solid lines indicate the center of the circular gray feature in each of the thumb prints that corresponds to the S1 mode.

the waveforms was treated in the same fashion as the signals with no mine. Figures 3.9-3.12 show the resulting thumb prints for each of the propagation distances.

Considering four propagation lengths separately we can see an interesting trend develop. In each of these thumb prints we still see the circular gray feature that corresponds to the arrival of the S1 mode. We've extracted the arrival time in microseconds under each of the thumb prints. From these we can see a shift to the left, a sooner arrival time, therefore a faster traveling velocity of the S1 mode. It can be hard to visually identify the shift from all of these thumb prints so we've presented the expected and extracted arrival time in Table 3.1. From this table we can see a couple of interesting features. First of all, the expected arrival times of the mode and the extracted times for each of the propagation lengths do not necessarily match. This is because of some difficulties that we occurred during data collection. We did not receive exact schematics of the quarter scale ship from the Aberdeen Testing Center, therefore we had to rely on on-site measurements of the ship which proved to be somewhat difficult with the curved

46

S1 arrival 201 μs

S1 arrival 199.8 us

S1 arrival 199.4 μs
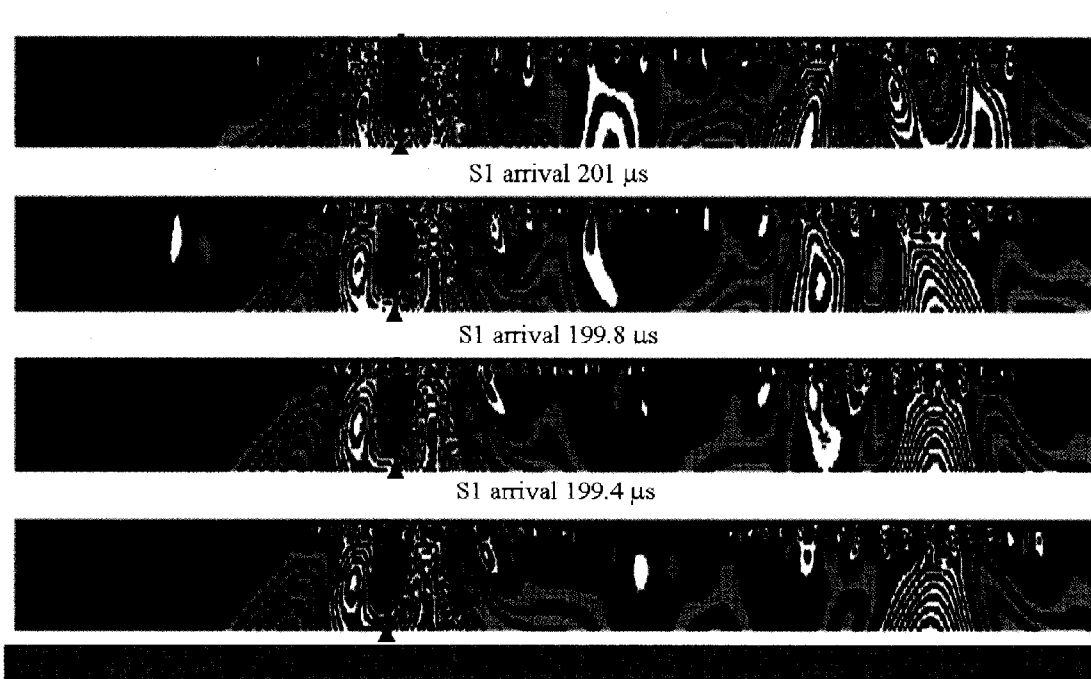
Figure 3.10: The thumb prints resulting from the DWFT on data collected from the propagation distance of 36.5" without the mock mine, then having it placed at positions B, D and E in 3.1a from top to bottom respectively. The vertical red solid lines indicate the center of the circular gray feature in each of the thumb prints that corresponds to the S1 mode.
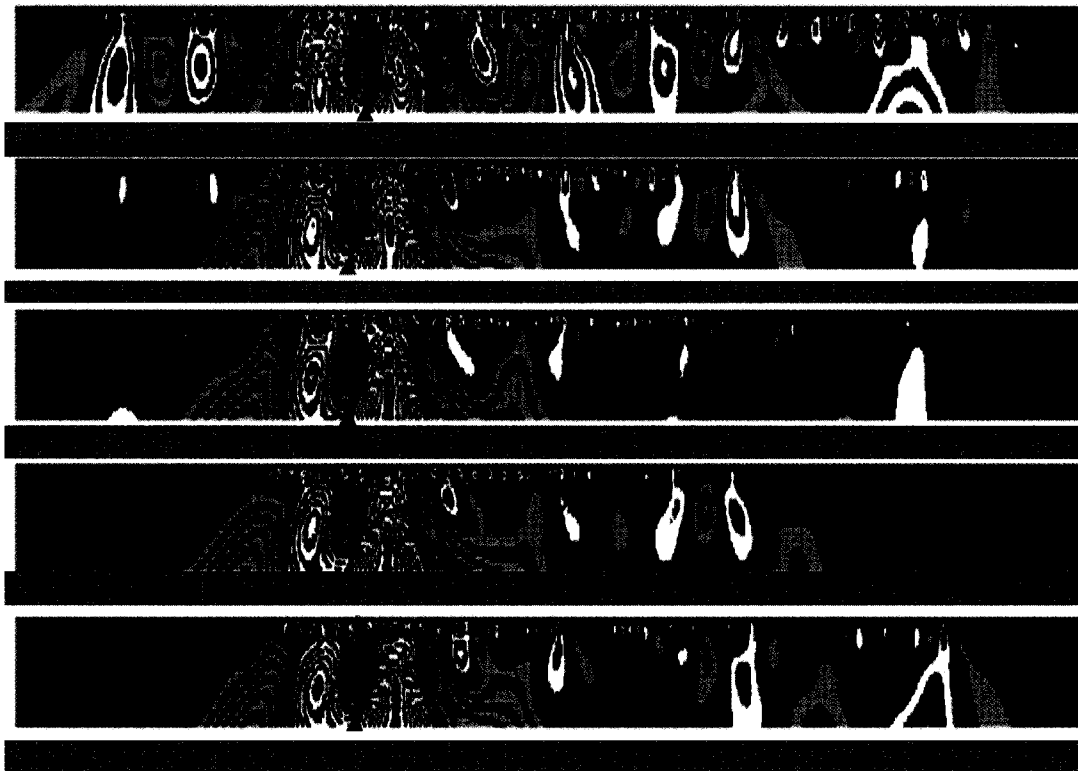
Figure 3.11: The thumb prints resulting from the DWFT on data collected from the propagation distance of 64.5" without the mock mine, then having it placed at positions B, D, E and G in 3.1a from top to bottom respectively. The vertical red solid lines indicate the center of the circular gray feature in each of the thumb prints that corresponds to the S1 mode.
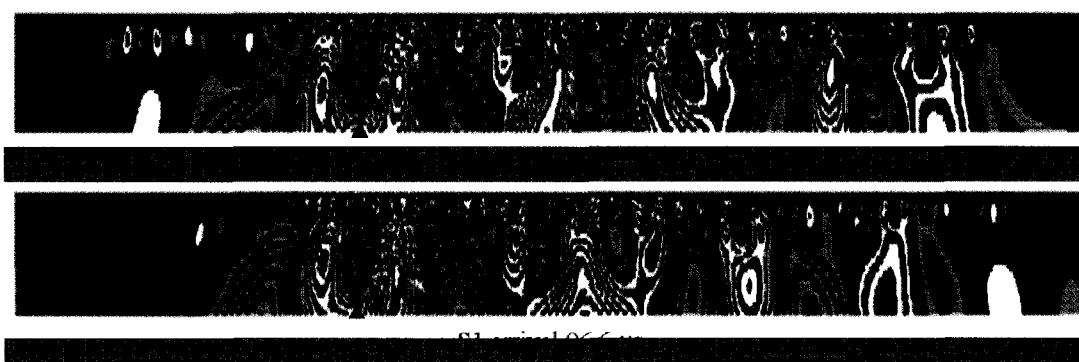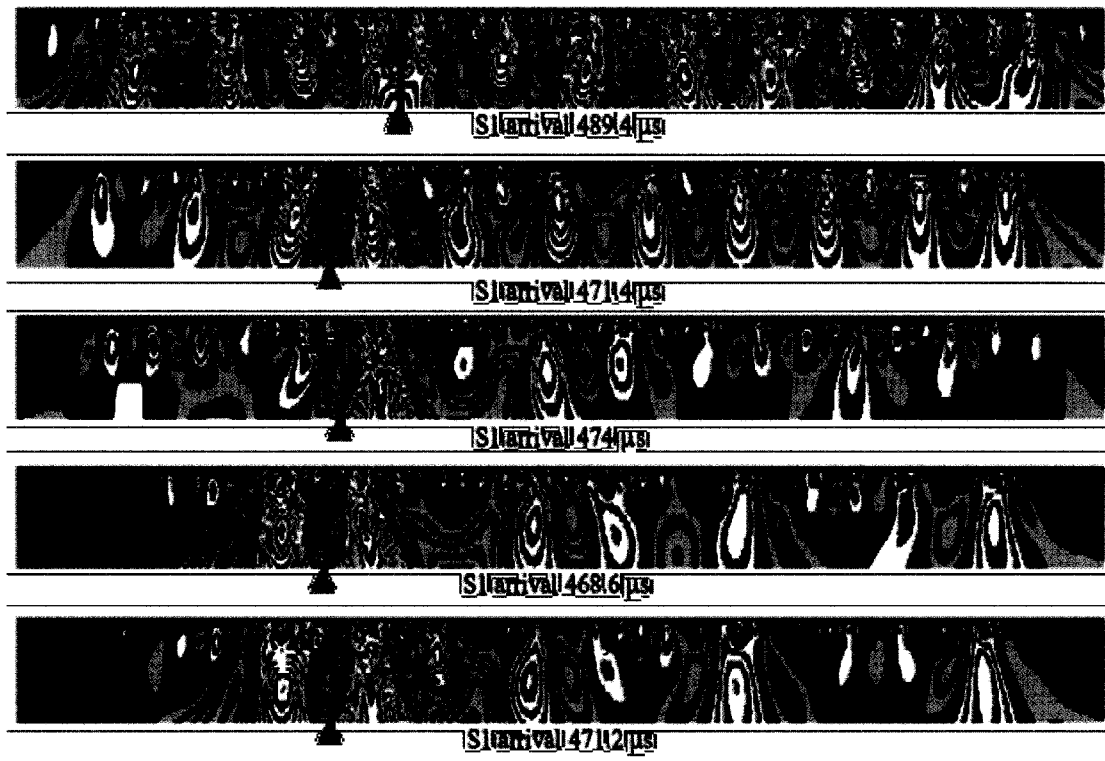
Figure 3.12: The thumb prints resulting from the DWFT on data collected from the propagation distance of 91.5" without the mock mine, then having it placed at positions B, D, E and G in 3.1a from top to bottom respectively. The vertical red solid lines indicate the center of the circular gray feature in each of the thumb prints that corresponds to the S1 mode.

Propagation Distance (in)	Transmitter Location	Receiver Location	Discription	Mode Arrival (μs)
19.5			Expected	82.02
	C	A	No Mine	97.8
	C	A	B Mine	96.6
36.5			Expected	193.14
	F	A	No Mine	201
	F	A	B Mine	199.8
	F	A	D Mine	199.4
	F	A	E Mine	197.8
64.5			Expected	341.31
	H	A	No Mine	339.8
	H	A	B Mine	336.2
	H	A	D Mine	335.6
	H	A	E Mine	335.6
	H	A	G Mine	337.6
91.5			Expected	484.19
	I	A	No Mine	489.4
	I	A	B Mine	471.4
	I	A	D Mine	474
	I	A	E Mine	469.6
	I	A	G Mine	471.2

Table 3.1: Expected and extracted S1 arrival times from Aberdeen test 1 for each of the four propagation distances and mine configurations.

surfaces and bowing of the structure. However, we are fairly confident that our distance measurements are close to the actual dimensions since the extracted arrival times are in the neighborhood of those expected. Another factor in the differing of the times is that the expected time is derived from the dispersion curves that assume a flat plate structure, not one that is warped, corroded, welded and attached to structural members such as the stringers inside the hull. Moreover, we have the luxury of having measurements with and without the mock mine attached, so accurate distance measurements are not completely necessary at this point in the development. The next point of interest is that we see a shift in the extracted times to a slightly sooner arrival time. This is consistent with being on the shoulder of the S1 dispersion curve. The addition of the mock mine mass acts as a local thickening of the hull where it is attached so the frequency thickness product increases, thus increasing the group velocity of the mode when the mine is present.

For test 2 we did a similar propagation study on the stern section of the hull to see if the different sections of the hull vary in their wavelet signatures due to structural variances. Transmitting from position A in Figure 3.1b and receiving at steps out toward the waterline of the ship, we gathered similar results to the mid section. Figure 3.13 shows the raw waveforms collected from seven increasing receiver positions towards the outside of the hull. For comparison we've also included the waveforms with the mock mine positioned at position M1 in Figure 3.1b. Again, it is not readily apparent what the difference is between the signals with and without the mine without further signal processing. We then passed the signals through the same processing scheme as used in Test 1. Here we present the windowed portions of wavelet filtered signals (Figure 3.14) and their resulting

Figure 3.13: The raw waveforms from Aberdeen Test 2. The transmitter was placed at location A on Figure 3.1b, close to the keel of the stern section of the destroyer. The receiver was then stepped outwards towards the waterline taking measurements at each step. Both signals without the mock mine and with it placed at location M1 are included. The vertical solid black lines indicate the processing window around the S1 mode, while the dashed red and blue lines indicate the expected arrivals of all the symmetric and antisymmetric modes.

Propagation Distance (in)	Transmitter Location	Receiver Location	Discription	Mode Arrival (μs)
27			Expected	142.9
	A	B	No Mine	149.2
	A	B	M1	148.2
54			Expected	285.8
	A	C	No Mine	273.0
	A	C	M1	273.0
81			Expected	428.6
	A	D	No Mine	421.0
	A	D	M1	419.6
105			Expected	555.6
	A	E	No Mine	576.2
	A	E	M1	534.8
112			Expected	592.7
	A	F	No Mine	637.4
	A	F	M1	570.2
127			Expected	627.0
	A	G	No Mine	726.8
	A	G	M1	623.0
132			Expected	698.5
	A	H	No Mine	663.0
	A	H	M1	658.0

Table 3.2: Aberbeen Test 2 extracted mode arrival times compared to expected times for the S1 mode from the dispersion curves.

thumb prints (Figure 3.15) from the DWFT. The windowed sections of the filtered signal further emphasize the point that it is very difficult to decipher the influence of the mass loading from the time series signals alone. We have again extracted an arrival for the S1 mode from the thumb prints using the circular gray feature sandwiched between two larger white features. The locations of this feature are given by the vertical solid red lines in figure 3.15. If we look at the numbers for the S1 arrival times more closely (Table 3.2) we continue to see a general decrease in arrival time with the addition of the mock mine.
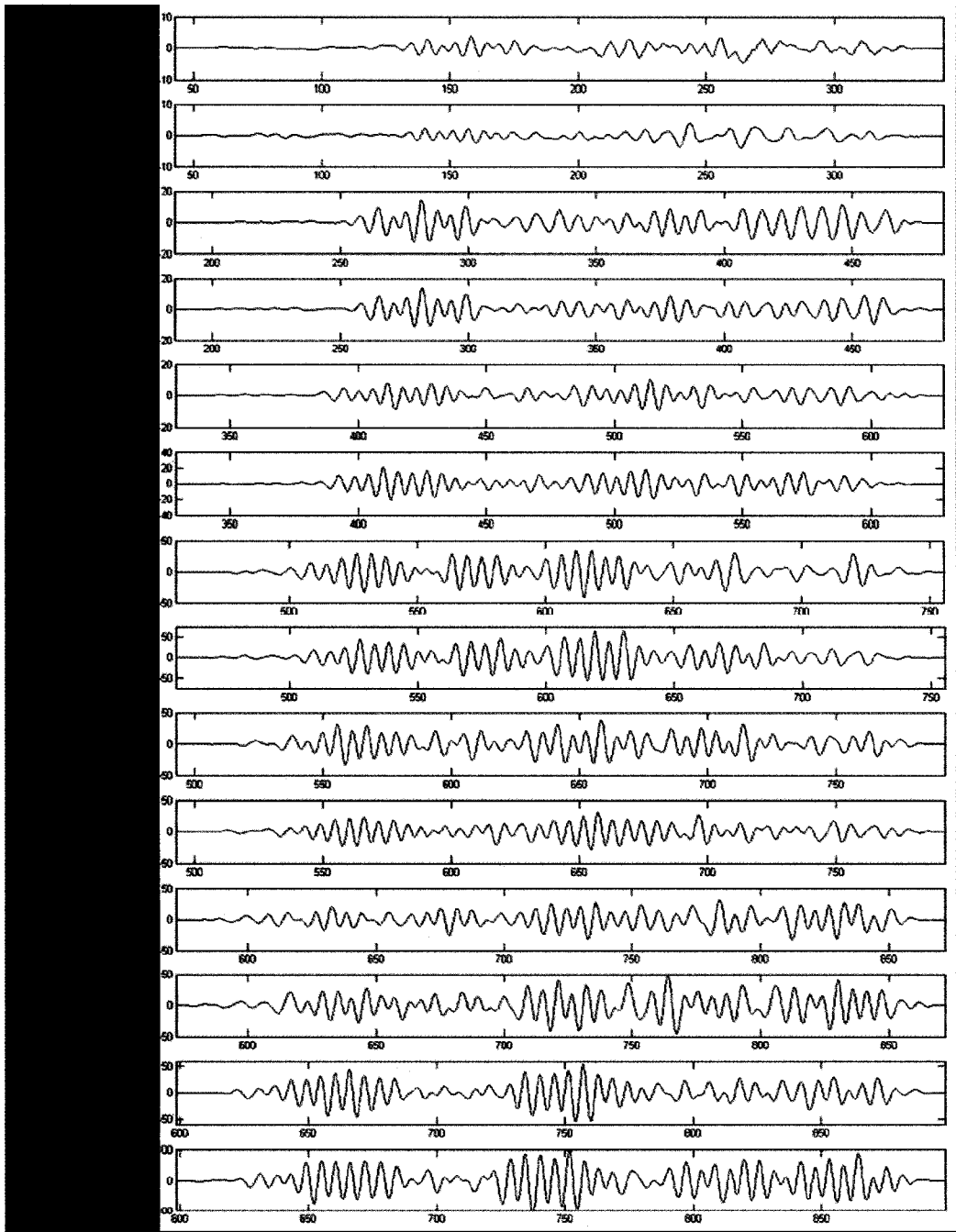
Figure 3.14: Aberdeen Test 2 windowed filtered signals sent to the DWFT.
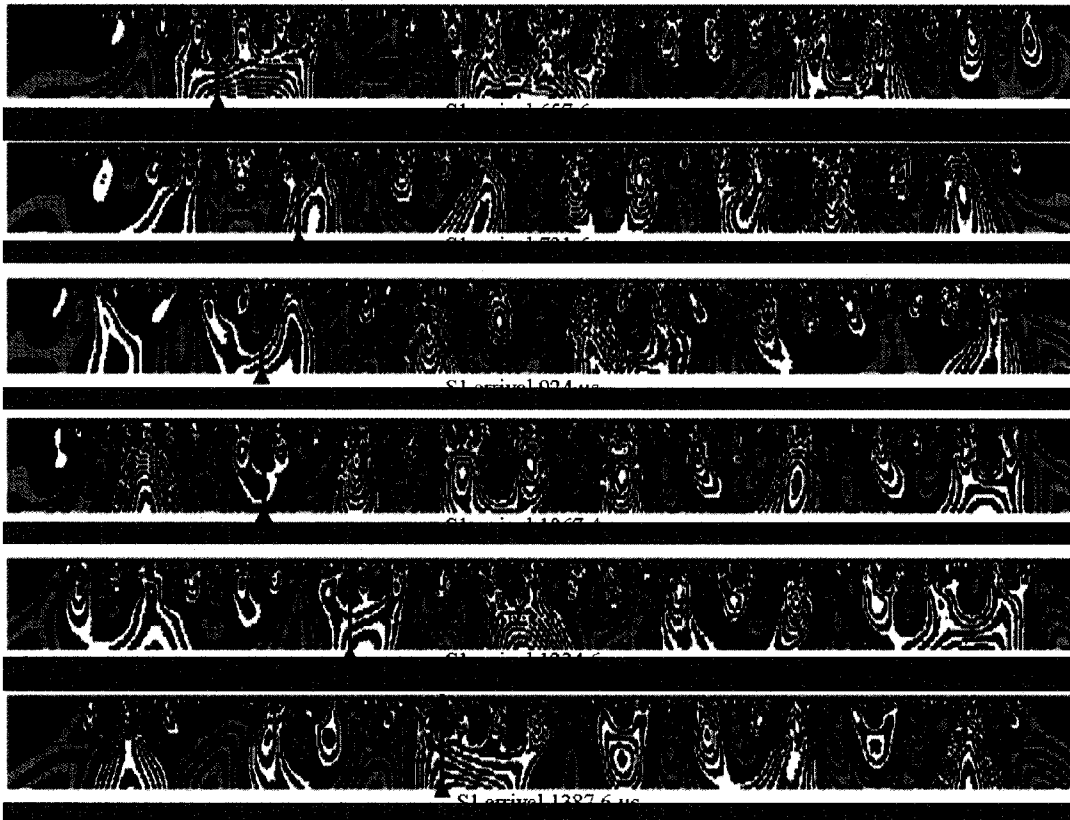
Figure 3.15: Aberdeen Test 2 DWFT fingerprints. The arrival for the S1 mode is indicated by the vertical red line in each of the images.

For our last two preliminary tests on the quarter sized hull in dry dock at Aberdeen we wanted to see how far we could propagate a usable signal. The first of these, which we will refer to as Aberdeen Test 3, propagated the signal from the waterline on the stern section down the hull towards the keel then back up the opposite side of the hull. When referring to Figure 3.1b the locations correspond to transmitting from H and receiving on the other side of the keel (not shown) at the corresponding symmetric locations to the parenthesized points. The recorded signals are for propagation lengths of 11', 12'9", 15', 17'3", 19'6", and 21'6" as measured on site. Figure 3.16 shows the raw time series data for the increasing lengths top to bottom. Again the expected arrival times are given by the vertical dashed lines, as well as the window around the first arriving S1 mode by the solid black lines. Using this windowed portion of signal we were again able to produce similar features in the resulting thumb prints from the signal processing routine. Figure 3.17 shows these resulting thumb prints with the feature of interest indicated by the vertical red lines in each of the images.

We have seen in these preliminary tests that the S1 arrivals that we extract using the thumb print features and the expected times from our distance measurements on site don't quite match up. Instead of the mode traveling at a slightly different wave speed we are more inclined to believe our distance measurements were off. We can use the the S1 mode group velocity of 4.8 mm/μs to determine a new distance measurement for each of the waveforms and compare that to what was measured on site (Table 3.3) for Test 3. On average the difference is about 11 cm, and considering that the transmitter footprint was 10 cm, the receiver 2.54 cm and that the error is between 1.7-3.5% of the total propagation distance, it is reasonable to think that our measurements could be off by this amount. If we
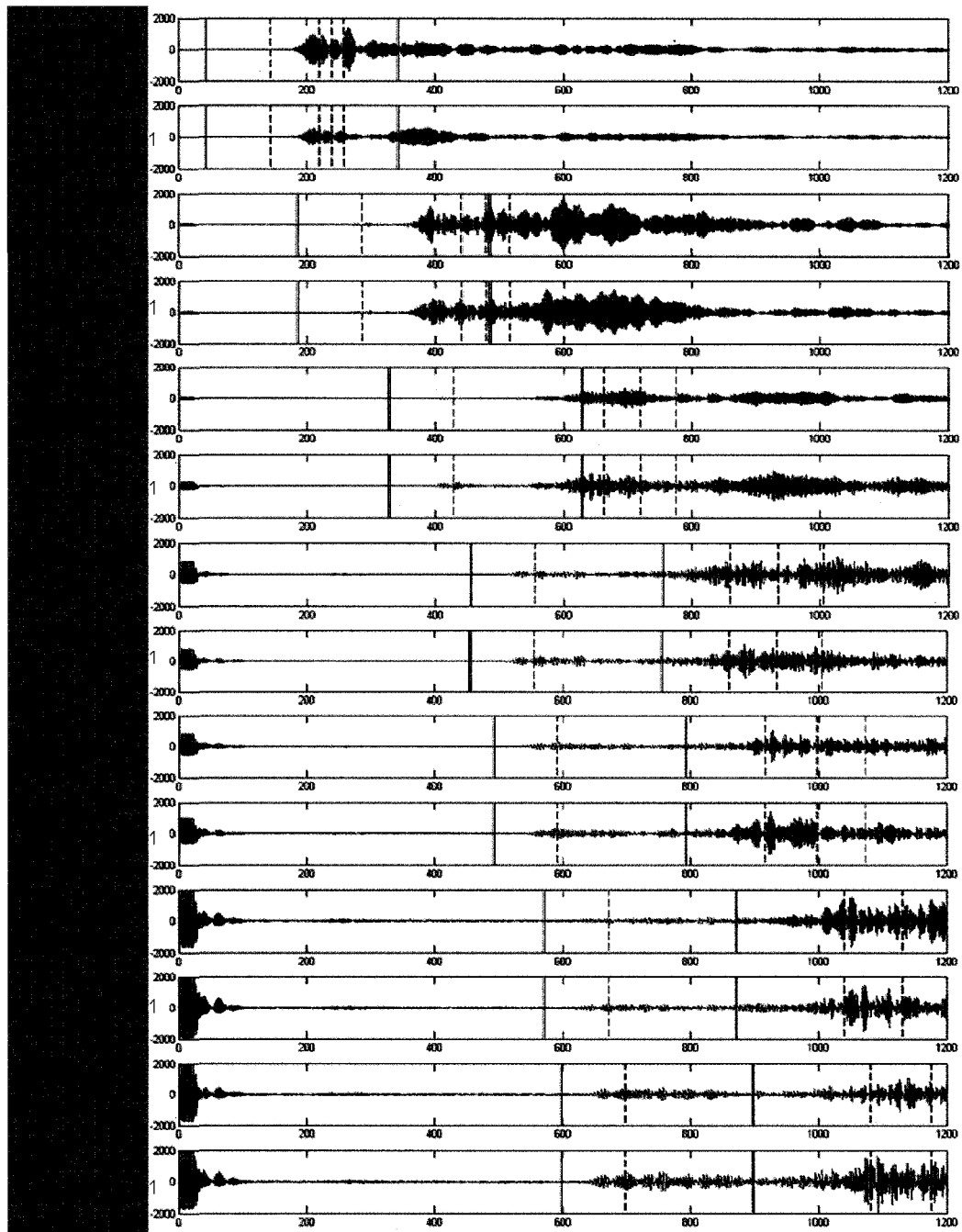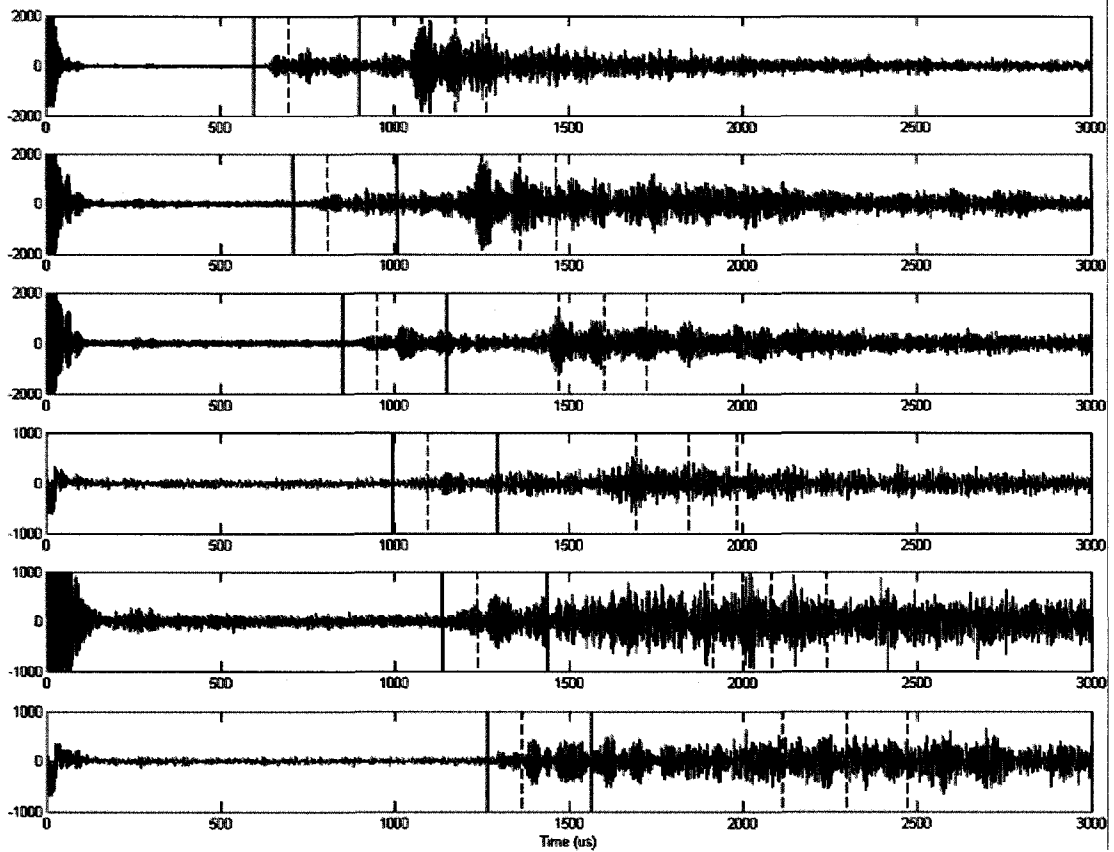
Figure 3.16: The raw waveforms from Aberdeen Test 3. The transmitter was placed at location H on figure 3.1b, close to the waterline of the stern section of the destroyer. The receiver was then placed on the near side of the keel for the top signal then placed on the other side stepping up the opposite side of the hull towards the waterline at positions Z, Y, X, W, and V. The vertical solid black lines indicate the processing window around the S1 mode, while the dashed red and blue lines indicate the expected arrivals of all the symmetric and antisymmetric modes.
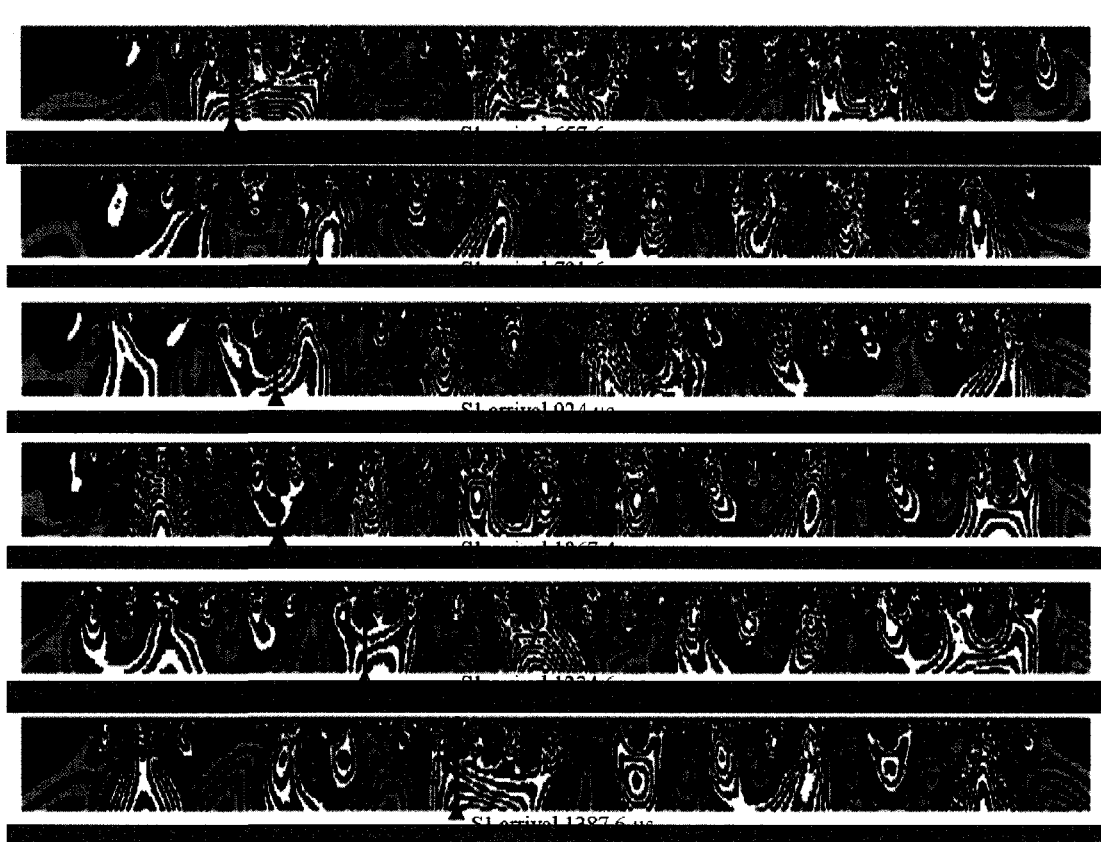
Figure 3.17: Thumb print images from Aberdeen Test 3.

Trans - Rec Locations	Extracted Arrivals (μs)	Calculated Distances (m)	Measured Distances (m)	Difference (cm)
H - A	657.6	3.156	3.353	19.7
H - Z	791.6	3.799	3.886	8.7
H - Y	924	4.435	4.572	13.7
H - X	1067.4	5.123	5.258	13.5
H - W	1234.6	5.926	5.944	1.8
H - V	1387.6	6.66	6.553	-10.7
				avg: 11.35

Table 3.3: Aberdeen Test 3 difference between expected and extracted arrival times translated to a difference between measured and actual propagation distance.
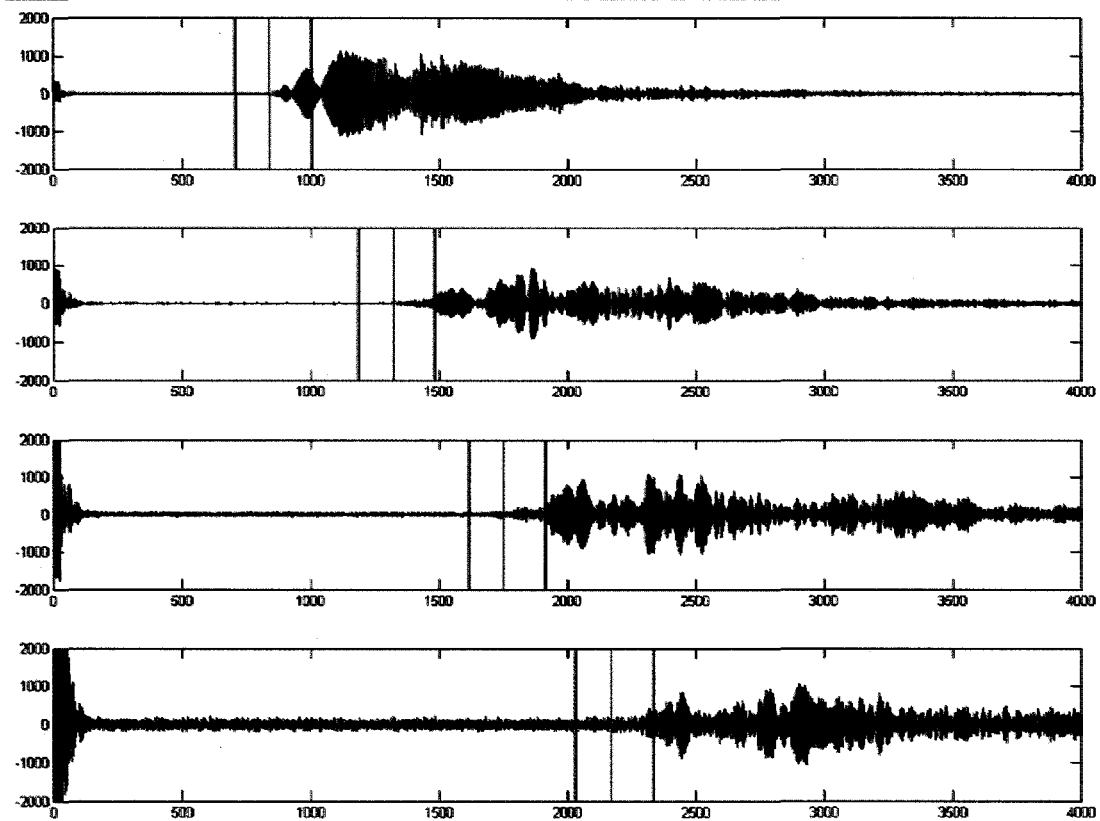
Figure 3.18: Raw time series signals, transmitting lengthwise down the midsection of the hull for increasing distances. The vertical green line shows the point that was picked to center the S1 window around, the window extent is given by the black lines.

keep this in mind we can discern distances for our final set measurement in Test 4. In this test we propagated lengthwise down the midsection of the hull. Because of the constraints of the dry dock we were unable to measure the distances for the test. Instead, we can use the signal processing routine that we have developed in this section to extract the arrival times of the S1 mode from the recorded signals to determine the propagation distances.

To start this process we looked at the raw time series signals, shown in Figure 3.18. Instead of knowing the propagation distance before hand, we chose to
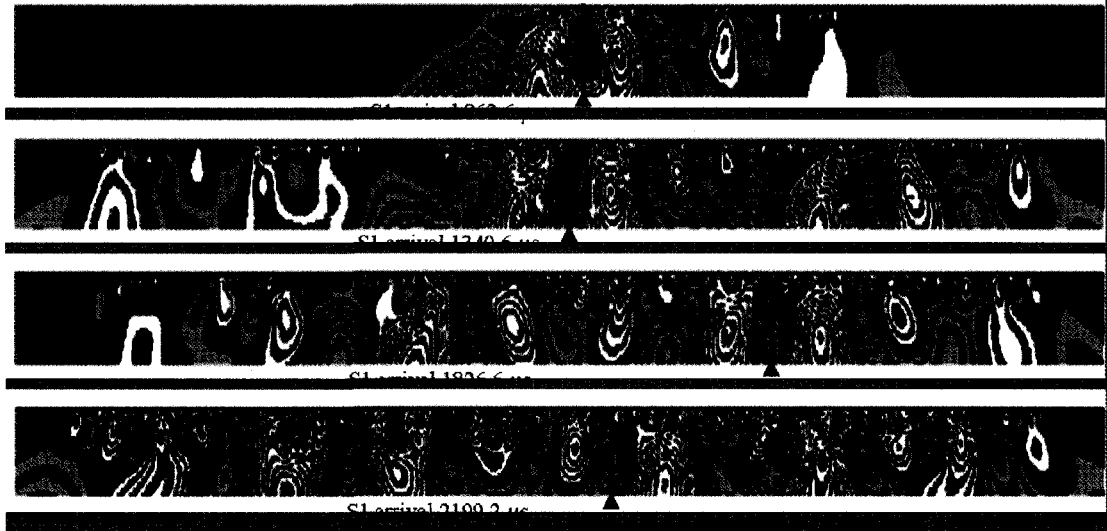
Figure 3.19: Resulting thumb prints from Aberdeen Test 4 in which the propagation length was unknown but we are able to pick out the first arriving S1 mode from the images indicated by the circular gray feature that is marked by the vertical red line.

estimate the S1 arrival from experience with the signals. This was done by choosing the location indicated by the green line in each of the signals. The resulting windows are shown by the black vertical lines. The signals were then processed, Figure 3.19 shows the resulting thumb prints from the windowed portion of the signals. When we visually search each of these images we see the familiar gray circular feature that is surrounded by two larger white features, the red lines indicate the location of this feature of interest and the S1 arrival time for each signal is included below the thumb prints. If we take an S1 mode velocity of 4.8 mm/μs we find that these arrival times correspond to propagation distances of 3.967 m, 6.435 m, 8.767 m, and 10.556 m from top to bottom respectively. We can then go back and look at the expected arrival times of all the modes for these distances and compare to the signals. In Figures 3.20-3.23 we show how the ex-

Figure 3.20: Shows the reverse processing of the extracted arrival time to determine propagation length and compares the expected arrival times for all modes for this distance to the filtered and raw signals.

tracted arrival times match to the filtered and raw signals. This progression reiterates the importance of being able to extract the arrival times through signal processing not just from looking at the unfiltered time series waveforms. As the distance increases the signals become more corrupted by the numerous scatterers due to the structure of the ship hull and the the dry dock that it is sitting on. In Figure 3.23 we see that it is almost impossible to discern the mode arrival from the filtered signal without the aide of the feature extraction from the DWFT.

In these preliminary tests at the Aberdeen Testing Center we have confirmed proof of concept. We have successfully shown that we can use a high powered
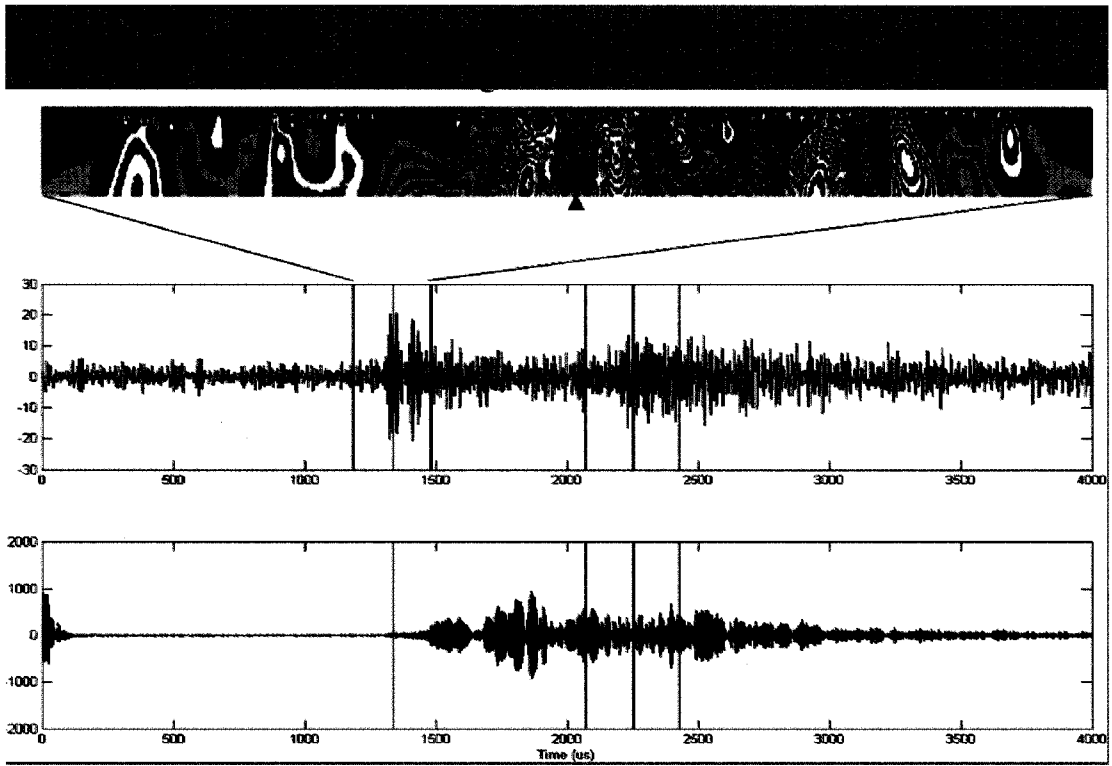
Figure 3.21: Shows the reverse processing of the extracted arrival time to determine propagation length and compares the expected arrival times for all modes for this distance to the filtered and raw signals.
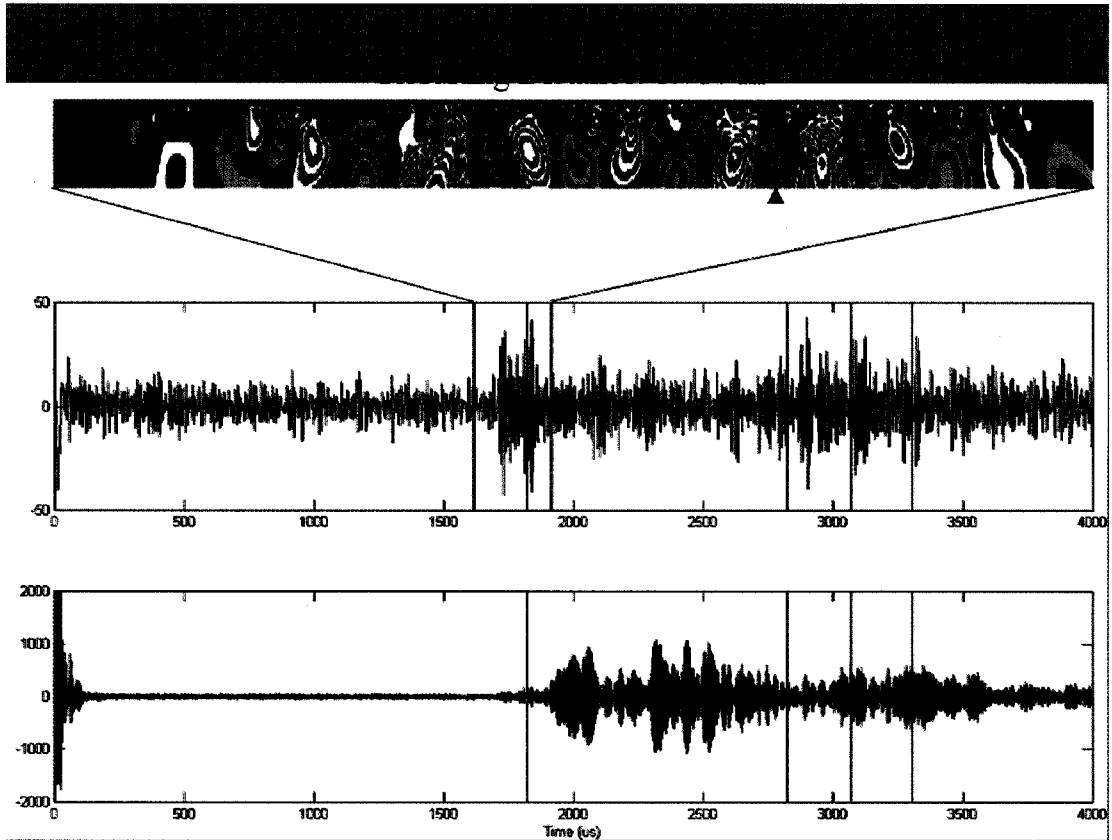
Figure 3.22: Shows the reverse processing of the extracted arrival time to determine propagation length and compares the expected arrival times for all modes for this distance to the filtered and raw signals.
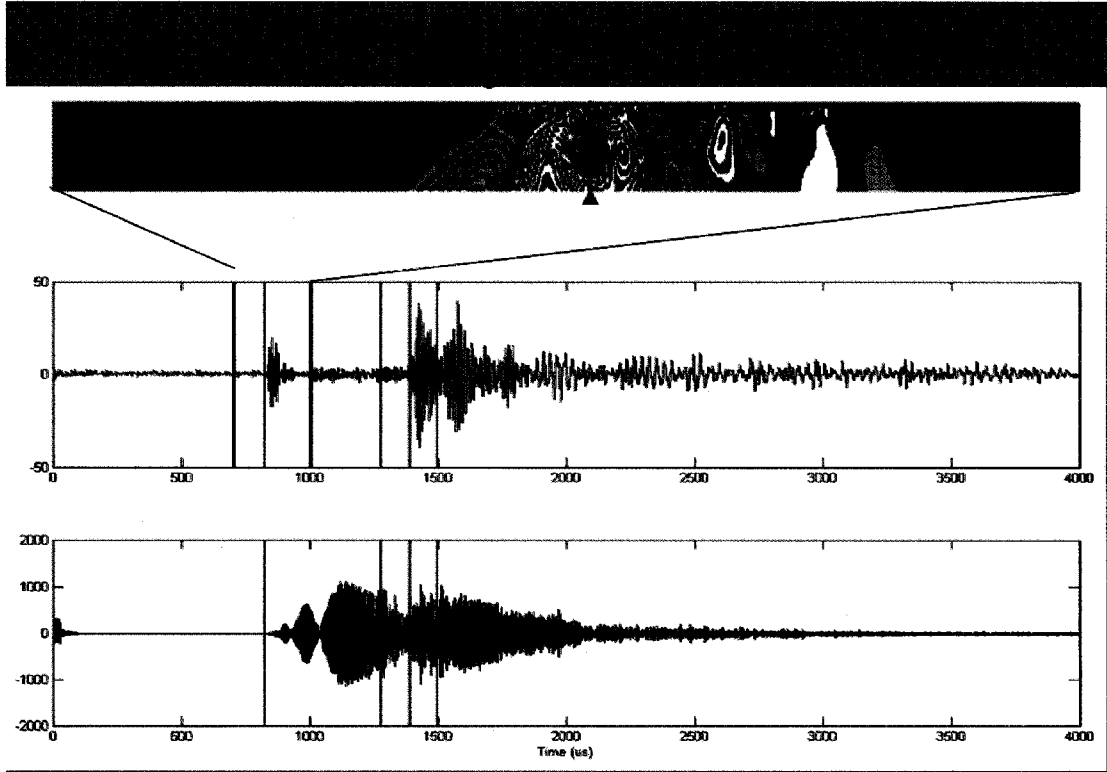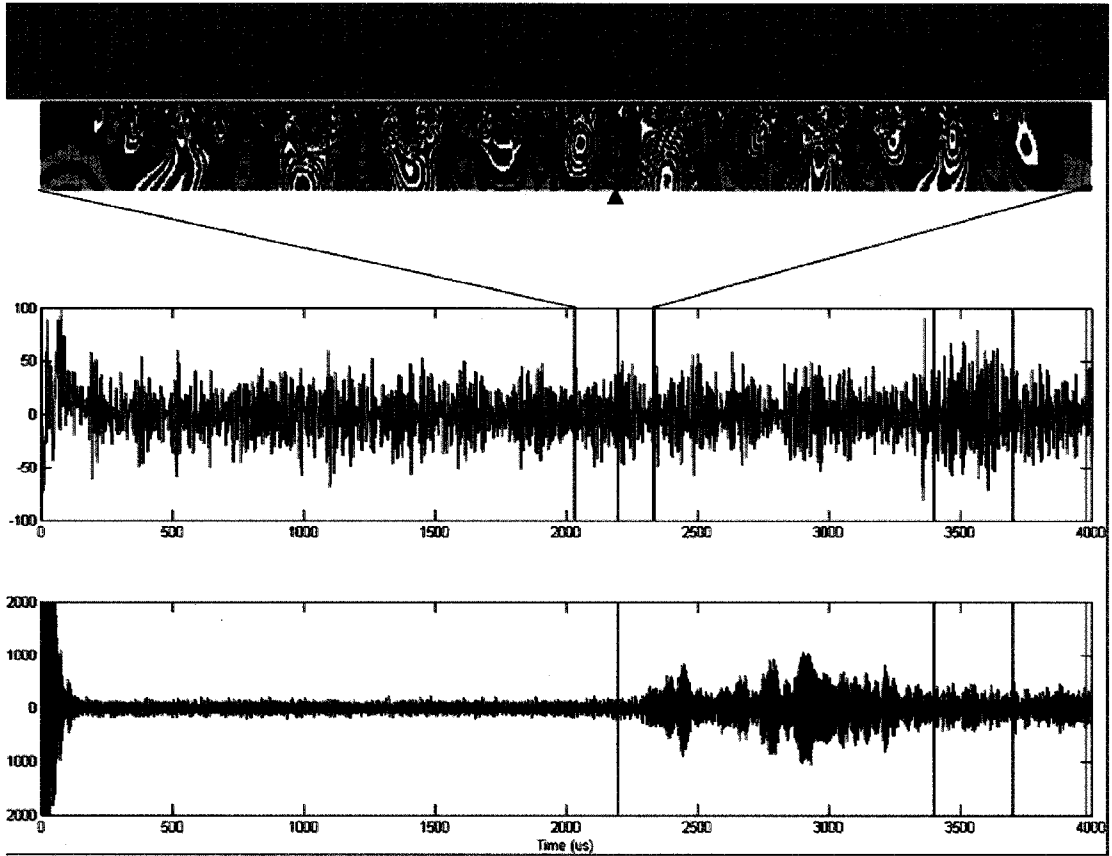
Figure 3.23: Shows the reverse processing of the extracted arrival time to determine propagation length and compares the expected arrival times for all modes for this distance to the filtered and raw signals.

pulser/receiver to transmit usable signals in a quarter scale ship hull in dry dock. Propagation distances up to 10.5 m have shown similar features in the resulting thumb prints from the DWFT. Using this feature extraction we have also shown that there is a reasonable correspondence between the mass loading on the surface of the hull by the mock mine and a shift to the left of the the feature of interest. This shift corresponds to a quickening of the mode which is what we would expect since we positioned our tests on the shoulder of the S1 dispersion curve. Some of the limitations of this work have been inconsistent coupling to the ship hull and rough distance measurements. Having accurate schematics of a ship would help to discern proper dimensions in practice and working on a ship sitting in the water would alleviate the coupling difficulties. Our next step in the development of this mine detection technique was to do field testing on a actual ship in the water.

3.1.2 Little Creek In-Situ Testing

The second phase of this REMORA project was to continue proof of concept tests on a full scale ship in the water. This in-situ data collection was conduced at at the Naval Amphibious Base, Little Creek Virginia. For four days the USNS Del Monte was used as our testing ship and diver support was provided by the EOD Training and Evaluation Unit Two (EODTEUTWO). The Navy Public Affairs Library classifies the Del Monte as a T-AK-5049 in the Military Sealift Command ships, which is basically a cargo ship that the Navy uses to transport troops and munition. This ship is docked at Little Creek for training purposes.

For our experiments we needed access to a small Zodiac boat in the water, the pier for most of our experimental equipment and finally the ship hull itself under the waterline. It made the most sense to situate ourselves on the port side
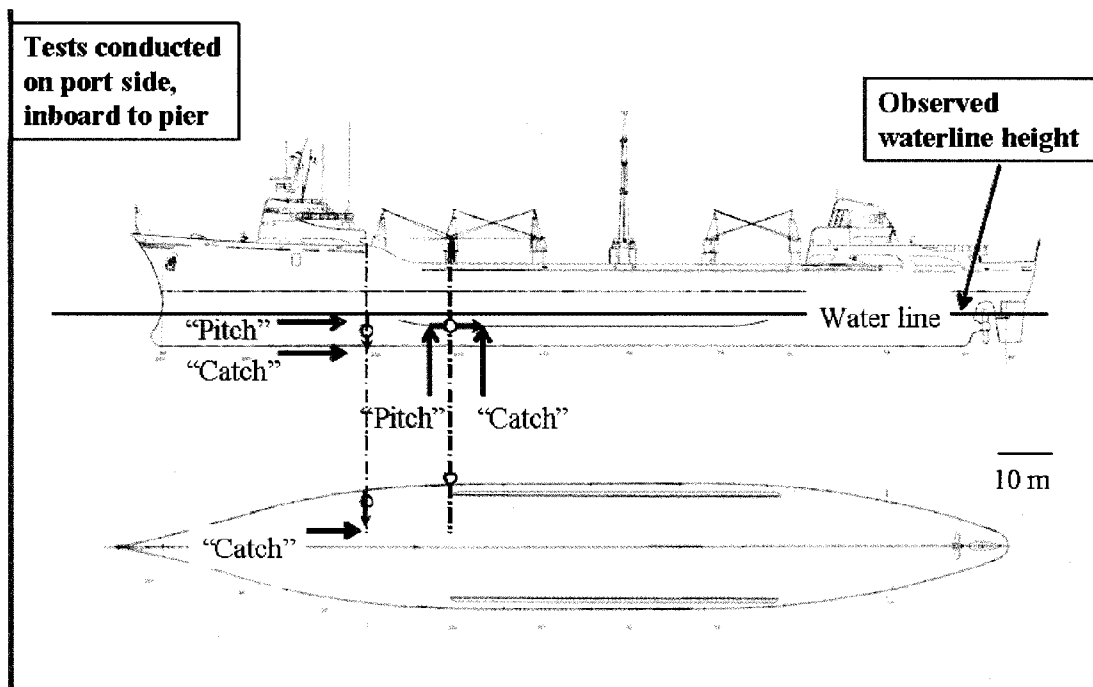
Figure 3.24: Sketch of the Del Monte cargo ship where we performed in-situ experiments.

of the ship towards the bow before the first pier bumper around frame numbers 132 and 152 (Figures 3.24-3.25). From this position we could take longitudinal measurements down the length of the hull towards the stern as well as transverse measurements from the waterline towards the keel. Figure 3.25 also shows some of the environmental challenges that we faced throughout the duration of these tests. First of all the scientific equipment including the high powered pulser and the computer were located on the pier about 2-3 m above the waterline. This made communication rather difficult, having to relay messages over the edge of the pier, not to mention the lack of communication once the divers were submerged. Also a source of difficulty was the turbid water conditions. In Figure 3.25d the magnetic transducer frame is located less than a meter under the waterline but yet it is

(a) Del Monte pier side setup

(b) Test mines on hull side

(c) Divers between pier and Del Monte
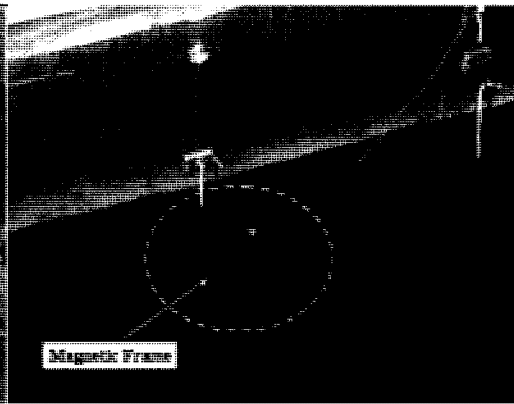
(d) Magnetic transducer frame on hull

Figure 3.25

barely visible. At times the underwater visibility was as low as 1 inch, this made it very hard for the divers to accurately position the equipment at times. One of the strengths of the guided wave technique is that it does not rely on visibility, however, at this stage in development it is important to know the configuration of measurements we are taking so that we can extract useful trends.

Since we are concerned with the submerged part of the hull we need to consider the transduction of the ultrasonic signal into the hull. As with the tests conducted at Aberdeen we need to select our propagating modes using the angle wedge technique. Here the coupling becomes easier, since we are already underwater we don't need an angle block or coupling fluid, instead we use a liquid wedge. A modal analysis of the Lamb wave modes generated by a liquid wedge performed by Jia [66] shows an inverse relationship between plate thickness and leak rate of the excited mode for a given frequency thickness value. It has also been demonstrated that the amplitude of the excited displacement increases with the size of the incident beam. Keeping this in mind we stipulate that since the ship hull is thick and we are using a lower frequency, we will have a relatively small leakage of energy into the water and that we can use a large diameter transducer within its focal length to excite propagating Lamb wave modes in the hull. However, we need to keep in mind with a large diameter transducer, the angle of mode excitation is smaller. In order to reliably hold the transducer in place at an angle we developed a custom magnetic frame to hold the transmitting transducer (Figure 3.26). This frame was designed to be fully adjustable on site so that we could fine tune the incident angle, the sweeping angle (direction of propagation) and focusing distance to optimize the signals. Some of the fine tuning adjustments were small and hard to operate underwater with gloves on and low visibility.

MAGNETIC FRAME

MAJOR ELEMENTS

3/4" RETAINING RING TO CAPTURE SLIDE

SEARCH TUBE FOR VERTICAL ADJUSTMENT

RETRACTABLE SPRING PLUNGER

BRONZE ROTOR

INDEX DISK WITH DETENTS EVERY 10 DEG

3/4" 316SS TUBING STRUTS

RADIUS ADJUSTMENT LOCKING SCREW

SETSCREW PREVENTS LOSS OF TRANSDUCER

CRIMP FERRULE FOR RG/58 COAX

EXISTING YOKE

NEW DELRIN TUBE END

NEW SHORTER TUBE

MAGNETIC MOUNTS

TRANSDUCER W/UHF THREAD MOUNT   COMPRESSION SPRING

Figure 3.26: Schematic of the magnetic frame which holds the transducer at the critical angle to the hull for the excitation of the guided wave mode in the ship hull. This frame is fully adjustable in focus height from hull, angle of incidence and sweep angle.

69
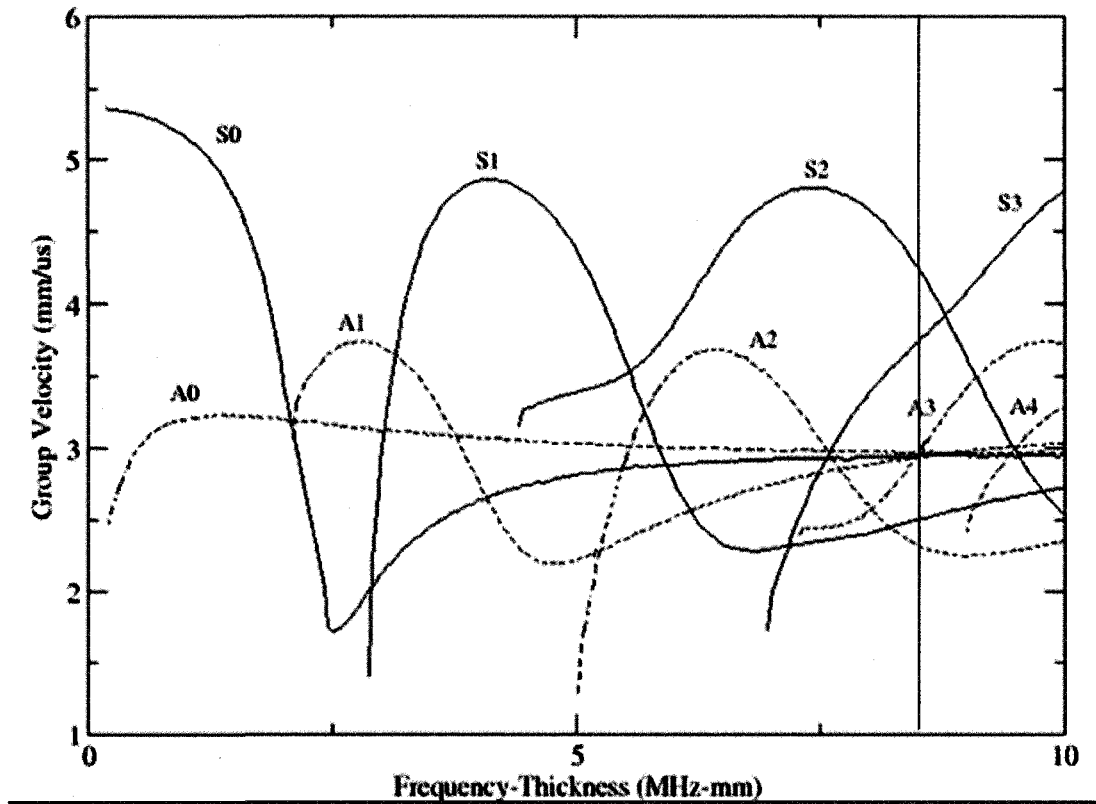
Figure 3.27: Steel dispersion curve showing the frequency (500 kHz) thickness (18.2563 mm) product (9.1281 mm-MHz) of the Del Monte side hull.

The side hull thickness of the Del Monte is 23/32" so that gives a frequency thickness product of 9.1281 mm-MHz for an excitation frequency of 500 kHz. Using this information we can see from the steel dispersion curve (Figure 3.27) that we are on the waning shoulder of the S2 mode. At this frequency thickness product the S2 mode has a phase velocity of 5.6 mm/μs which gives a critical angle for excitation of this mode in the hull of 15.53°. For the convenience of the divers we made an angle guide at 15.53° out of a piece of wood. The diver could easily place the guide against the hull and adjust the angle of the transducer to line up to the groove cut into the wood guide. This was a simple way to insure

that we started near the critical angle for each of the tests before attempting fine tuning adjustments for signal optimization.

We spent four days working with the divers developing a complex communication scheme. Sitting up on the pier looking at the oscilloscope waveform we were blind to the status of the set up. The divers on the other hand could put their hands on the apparatus but could not see very well because of the murky water. The experiments were also difficult to conduct because of the sensitivity to precise adjustments. Looking at the the signal we could see when the diver achieved optimal fine tuning but the time lapse between when we saw the signal, made a remark to a diver in the Zodiac who then pulled on the guy wire to the driver underwater was too great to record optimal signals most of the time. Then if we tried to get back to the observed signal strength we had to basically tell the driver to reverse a portion of their actions without actually knowing what those were. Despite these factors we were able to record some meaningful data that show promising results.

One of the most promising sets of data was from a test where we were looking at how the signal changes according to whether we were propagating longitudinally along the ship or transversely down the hull towards the keel. Figure 3.28 shows the signals recorded from propagating the S2 mode 1 m in both of these configurations with and without test mines. The test mines used in these particular tests were Italian and large Russian models (Figure 3.29). In Figure 3.28 we used a Fourier filter to eliminate the low frequency noise in the green signal to get the overlaid black waveforms. The top three signals show the transverse propagation followed by the longitudinal in the lower three. One interesting trend that we noted in the data is that when the mines were present the amplitude of the
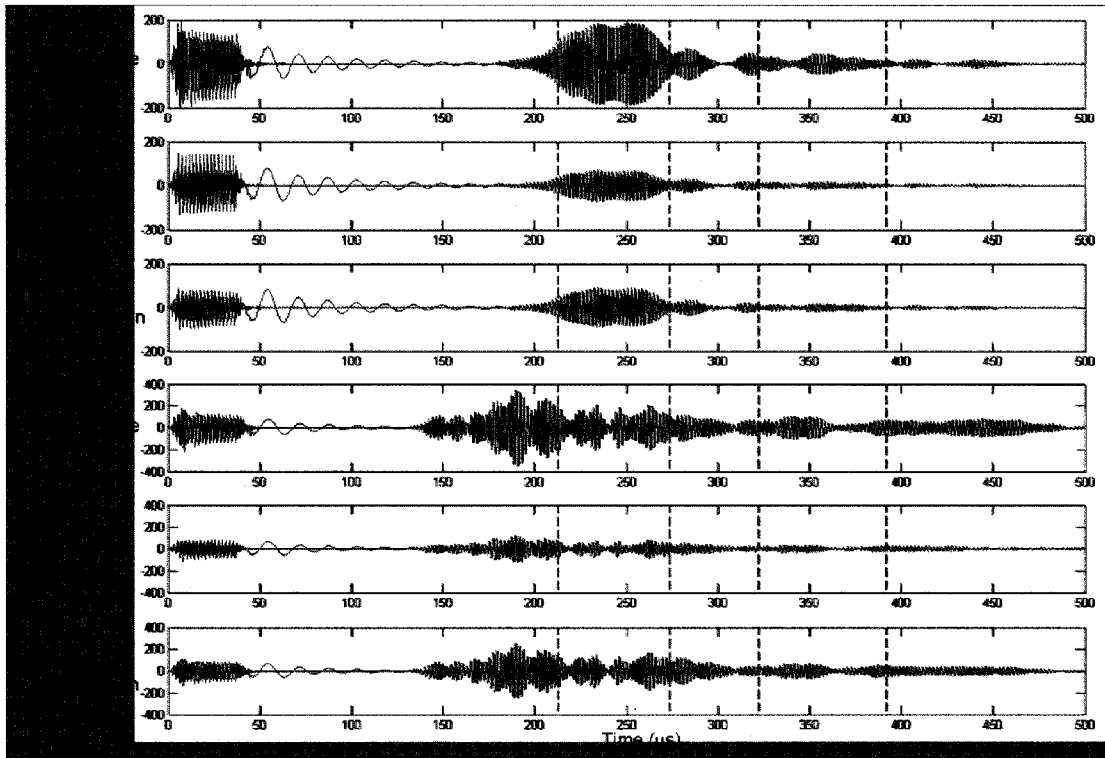
Figure 3.28: Six raw waveforms from two configurations of 1 m propagation through the hull of the Del Monte with and without test mines. The top three signals show transverse propagation where the transmitter was 1 m below the waterline and the receiver 1 m below that towards the keel. The bottom signals correspond to transmitting from 3 m below the waterline towards the stern longitudinally 1 m to the receiver. Each of the two configurations have signals generated without a test mine and with two different styles of mines, an Italian and a large Russian.

Figure 3.29: Picture of test mines used in data collection on the Del Monte. The Russian mines held the mass of the mine in contact with the ship hull with multiple strong magnets whereas the Italian mine had four smaller magnetic attachment points to the hull.
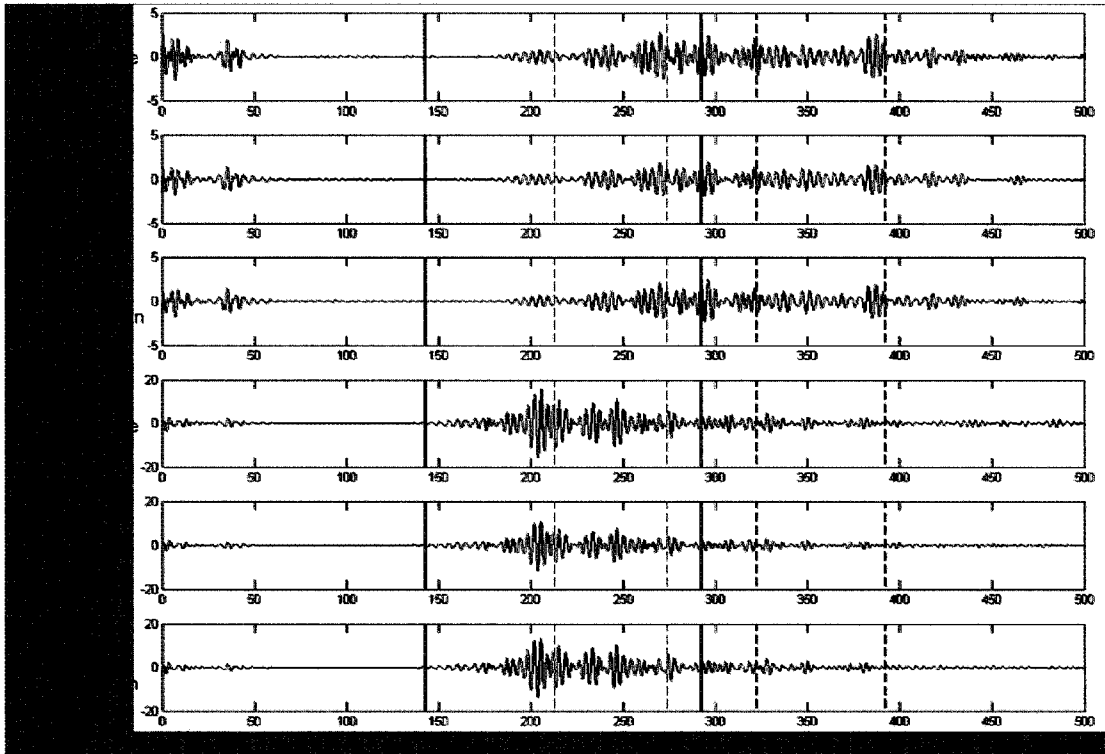
Figure 3.30: Filtered signals from the 1 m propagation data set found in figure 3.28. Notice the S2 mode to the left of the first dashed red line which indicates the expected arrival time of the S2 mode.

signals seemed to drop, this could be used in conjunction with other findings for a mine detection algorithm. However, as with the Aberdeen data it is impossible to see the first mode arrival from the unfiltered signals. If we pass the time series data through the same SWT filter as was used with the Aberdeen data we see the S2 mode start to emerge (Figure 3.30). Then if we pass the windowed portion around the expected S2 mode through the DWFT we can see the resulting thumb prints (Figure 3.31). In the longitudinal test we see the familiar circular gray feature corresponding to the arrival of the S2 mode. However in the thumb prints for the transverse test we do not see this feature (note box outline). This could be because the mode amplitude is not very large in the filtered signals. Instead we
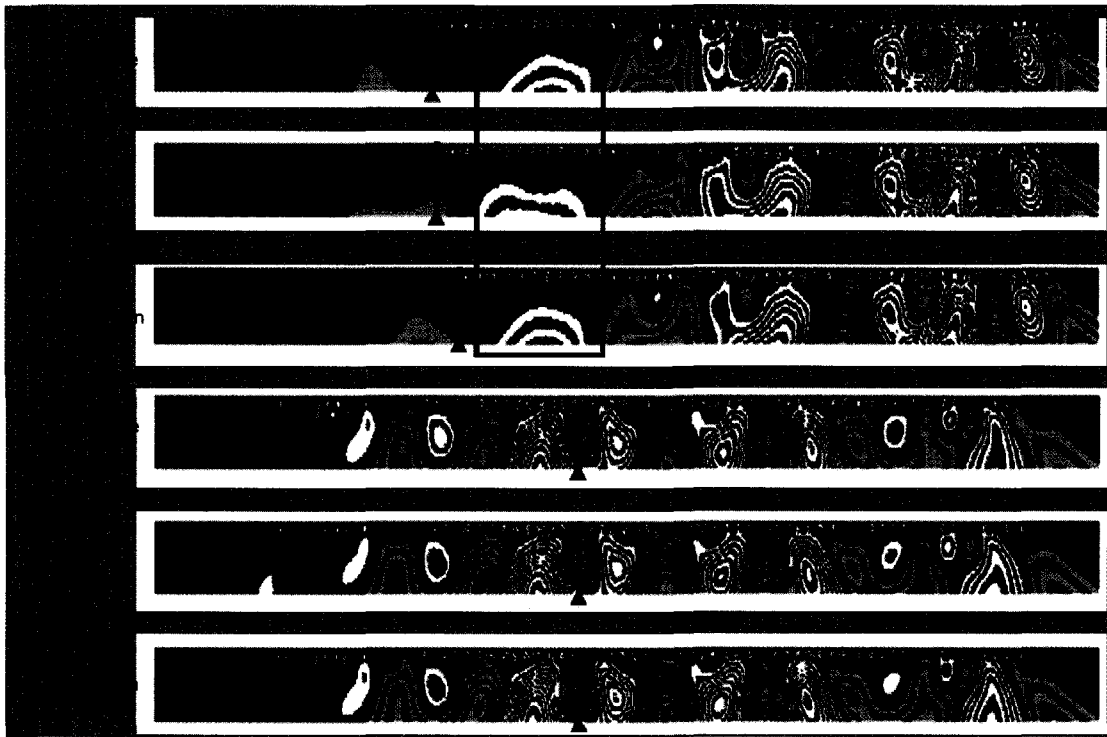
Figure 3.31: Resulting thumb prints of the S2 mode arrival from data in figure 3.28. Notice the presence of the familiar gray circular feature in the longitudinal signals. The transverse signals on the other hand have an interesting small pattern of features in stead of the circular gray feature.

do see a pattern of small features near the top of the thumb prints which could correspond to the S2 mode as well. We have marked the start of this pattern with the red lines for the transverse tests. With the addition of the mines this feature seems to move to the right in the thumb prints. This movement indicates a slowing of the S2 mode, which is what we would expect from our location along the dispersion curve for the S2 mode. It is also interesting that the large Russian mine that has a larger footprint on the hull would have a larger impact on the mode arrival time than the Italian mine. In the longitudinal direction the mines do not seem to have as large an impact on the propagating mode, this could be due to larger features like structural ribs attached on the inside of the hull or some other unseen factor.

With the experimental constraints it is hard to draw conclusive parallels between the processed signals and the mine configurations on the ship hull itself. We are confident from our findings however that we are able to excite the selected Lamb wave modes in the ship hull that are sensitive to mass loadings. In order for stronger conclusions and the development of a robust autonomous mine detection algorithm, there needs to be an experimental approach where the scientists are more able to control their testing environment including placement of equipment as well as visibility and communication with the underwater divers. A tank test with a section of a hull would be ideal for such a experiment. A clear water environment would allow the researchers to have a better understanding of the equipment status and the ability to carefully instruct the in-water divers. In this scenario, systematic tests would highlight the how supporting structures behind the hull affect the signal propagation. We saw evidence of such factor when comparing the propagation in the longitudinal versus transverse test. With fewer environmental

factors, data collection would be smoother. Our successful proof-of-concept tests indicate that with more data we would be able down-select design parameters to simplify signal excitation for robotic automation. The biggest factor being the ability to understand with confidence how the guided waves are interacting with the structure and added mass loading of the limpet mines. Another approach to systematically considering all of the parameters is to use full field numeric computer simulations. By allowing the model to examine each individual parameter individually i.e. the excitation of the guided waves, the guided wave interaction with a mass loading, or the effect of structural components on the guided wave propagation, we could optimize each. This would be very beneficial before further experimental testing so that the excitation can be fully automated decreasing the need for the in water diver having expertise in using the apparatus during development.

3.2   Pipe Coatings

Our next NDE application of guided waves is pipeline maintenance. The US Department of Transportation (DOT) installs and maintains over 2.3 million miles of pipeline nationwide that carry many substances including water, oil, natural gas and propane. Some of these pipelines have been in use for decades. With optimum maintenance the DOT holds that these pipelines could continue to function properly for more decades to come. In order for the DOT to determine which pipelines need maintenance they need to nondestructively examine their condition. One of the safeguards against damage to the pipelines are their coatings. Because the coatings protect the actual pipeline from the outside environment,

Figure 3.32: DOT sample of excavated pipeline section: 20" diameter 3/8" thick steel pipe with green epoxy and coal tar coatings.

damage to the coating could translate with time to irreversible pipeline damage. Due to the age of some of the pipelines, the DOT doesn't have accurate records of the particular coatings on every pipeline installed across the country. Therefore, the DOT is interested in being able to access a small part of a pipe, identify what type of coating is present on the surface and determine if it is in need of repair. Of particular interest are coating delaminations that could be a result of manufacturing flaws or the beginning signs of corrosion of the pipe substrate.

For this research we concentrate on large diameter, low pressure pipelines that are used for the transportation of the liquids and gases that fuel the nation and drive the economy. These types of pipelines are typically coated with epoxies and coal tar for protection. The DOT provided a sample pipe section that had been excavated from the field (Figure 3.32). After years of use, this sample was marred,

gouged and visually corroded. It is a good source of flawed data but in order to develop a technique for identifying flaws we need to start with a cleaner sample. Large diameter pipes are awkward to work with, so we used a thick plate to mimic the guided waves in the pipe sample since pipe can be thought of as a plate rolled up on itself [33]. In a pipe the waveforms are somewhat more complicated because of the constructive and destructive interference that occurs as the helical waves wrap around the pipe. However, since we are dealing with large diameter pipes, we don't have to worry about the wrapping effects as much since the circumference is large enough that the modes separate out in time. Using a flat plate also allows us to easily apply coatings in a controlled manner in the lab instead of having to outsource the coating application.

Since the task from the DOT was to identify different coating types, and determine delaminations of the coatings from the steel, we set up just this scenario. Using an 8' x 2' x 5/16" steel plate we covered four, 16" square areas with coatings (Figure 3.33). We obtained three different coatings: two epoxies (CANUSA HBE-95 from CCPC and Protal 7200 from Denso) and Bitumastic 50 from Carboline which is a coal tar. In order to manufacture a disbond under the coatings of uniform size and known location we tapped down a double thickness of plastic to prevent the coatings from adhering to the steel. The Protal 7200 has the same green color as the coating that was used on the pipe sample from the DOT so we decided to have a test area that was a layer of Protal 7200 and a layer of Bitumastic 50 to mimic the pipe sample in addition to the three individual coatings.

The steel dispersion curve (Figure 3.34) shows that guided waves excited in the pipe at 500 kHz for a frequency thickness value of 3.96 MHz-mm have dispersive properties. At this frequency thickness product, four Lamb wave modes propagate
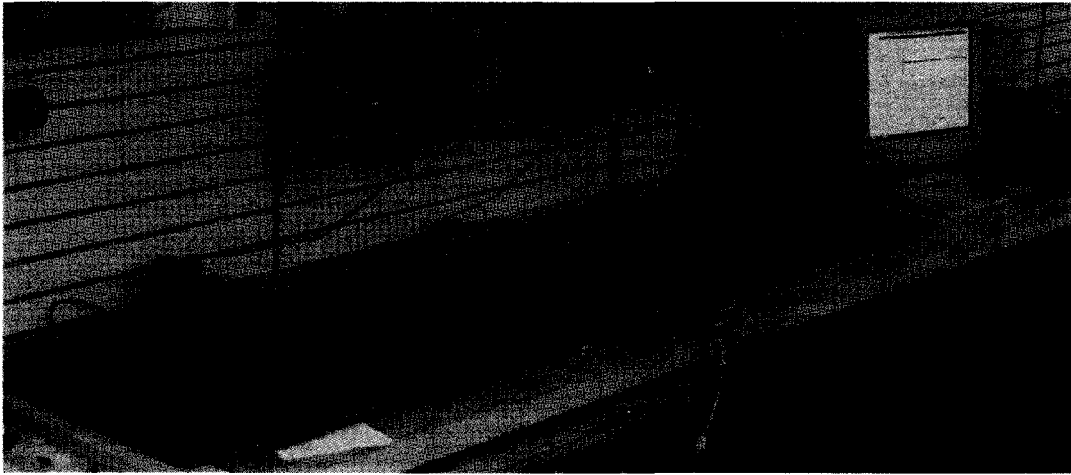
Figure 3.33: Steel test plate, 8' x 2' x 5/16", used as 'unrolled' steel pipe for testing of delaminations under coatings.
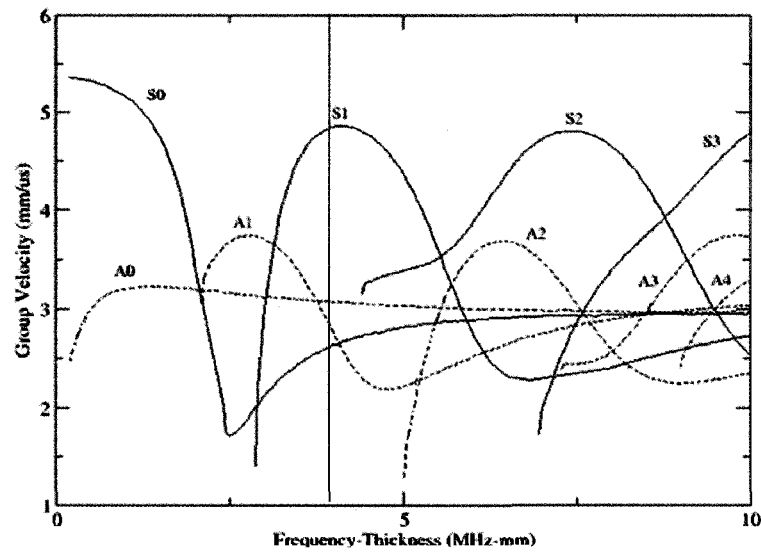

Figure 3.34: Steel dispersion curves. 500 kHz excitation, gives a frequency-thickness product of 3.96 MHz-mm for a steel plate 5/16" thick.

	Mode	Group Velocity (mm/μs)	Arrival
Frequency: 500 kHz	S1	4.85	89.03
Thickness: 7.9375 mm	A0	3.075	140.42
Distance: 431.8 mm	A1	2.9	148.89
	S0	2.6	166.07

Table 3.4: Propagating mode group velocities for a steel pipe 7.9375 mm thick excited with 500 kHz transducers and arrival times for propagating 431.8 mm.

with different velocities. The first arriving mode will be the S1 which will slow down with a thickness loss, next comes the A0 which is relatively non-dispersive in this region, followed by the A1 and S0 modes which speed up and slow down respectively with a thickness loss. Table 3.4 gives the group velocities of the modes as well as their arrival times for a propagation distance of 431.8 mm.

Unfortunately this simple analysis only considers the steel pipe wall underneath the coatings which change the mode properties. Assuming that the coatings are linear viscoelastic layers, for the time harmonic case, elastic and viscoelastic solutions are identical with the exception that the viscoelastic material constants are complex and frequency dependent [48]. By inserting the real and complex material parameters for the layers into the model through the transfer matrix method [39], the global matrix method [43], or a hybrid finite element-normal modes expansion method [44], [46] we can obtain dispersion curves for the propagating Lamb wave modes. Through these methods it is apparent that there is the emergence of a decaying exponential term that causes attenuation of the propagating waves in the viscoelastic material due to the complex roots of the dispersion relations. However due to the involved nature of solving for the full dispersion relations of the viscoelastic and elastic layer system we have chosen to approach our problem initially from an experimental standpoint. We contend that the steel

Material	Hardness	Hardness Unit	S_g
CANUSA HBE-95	> 85	Shore D	1.031
Denso Protal 7200	85 ± 2	Shore D	1.53
Carboline Bitumastic 50	15	Shore A	1.50 [49]
Steel	120	HV5	7.8

Table 3.5: Hardness and specific gravities for the coatings and steel for the pipeline tests. Due to the wide range of the viscoelastic coatings and elastic steel, three different hardness scales are used: Shore A, Shore D and the Vickers.

substrate is the largest factor in the propagation of the modes, and the effects of the coatings on these modes help us differentiate between the coatings. Due to the attenuation caused by the viscoelastic layers we expect a dampening of the guided modes compared to the clean steel plate. In the local frequency thickness region we also expect the dispersive nature of the pipe and layer system to be similar to that of the pipe. We expect this to hold more true for a layer that is more elastic rather than viscoelastic. The stiffer the layer, the more effect it has on the guided elastic modes in the underlying substrate [34]. The coal tar is a soft sticky material that indents with finger prints when touched. On the other hand, the epoxies are stiff hardened layers that cannot easily be cut with an utility knife. From product data sheets we've determined the hardness and specific gravity, S_g, of the different materials found in Table 3.5. The three different hardness scales are necessary because of the viscoelastic differences between the coatings and the steel. Shore A is the lowest scale, followed by Shore D for the viscoelastic properties then finally the Vickers scale tests the elastic properties of the steel with a 5 kg weight. This shows a great mismatch in hardness between the Bitumastic 50 and the steel pipe, while the two epoxies have comparable albeit lower hardness than the steel. This means that we would expect that the guided waves would
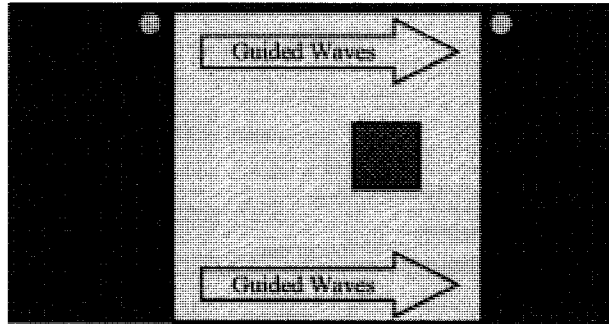
Figure 3.35: Coating test configuration. The transmitting transducer (left) and receiver (right) were stepped 2 mm at a time down the sides of the coating square pulsing at 500 kHz in order to excite the guided Lamb waves at each step. Each coating has a manufactured delamination of finite size (2" x 2") in the area indicated.

show more dispersive traits in the samples covered with the epoxy coatings than the coal car.

For the experimental tests of each of the coated areas on the large steel plate, we used linear stepper motors to take controlled steps down the sides of the test areas. Figure 3.35 shows the configuration of each of the coating squares. The transmitting transducer (left) and the receiving transducer (right) were stepped in parallel down the sides of the square taking a waveform every 2 mm for 72 steps. This can be thought of stepping around the circumference of a real pipe sample, or using a single transmit-receive transducer with the guided waves propagating all the way around the circumference. Figure 3.36 shows sample waveforms from three of the coating configurations: the HBE-95, Bitumastic 50 and Protal 7200 + Bitumastic 50. These waveforms were taken from flawless sections of the samples. Fortunately we immediately see some differences between the three different waveforms. The raw waveforms from the tests with epoxy coatings have lower signal to noise ratios, this dampening was expected due to the viscoelastic properties of
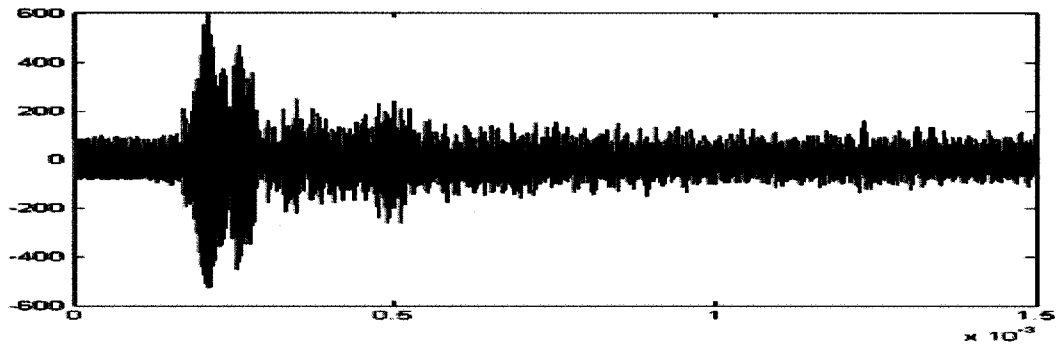
(a) HBE - 95
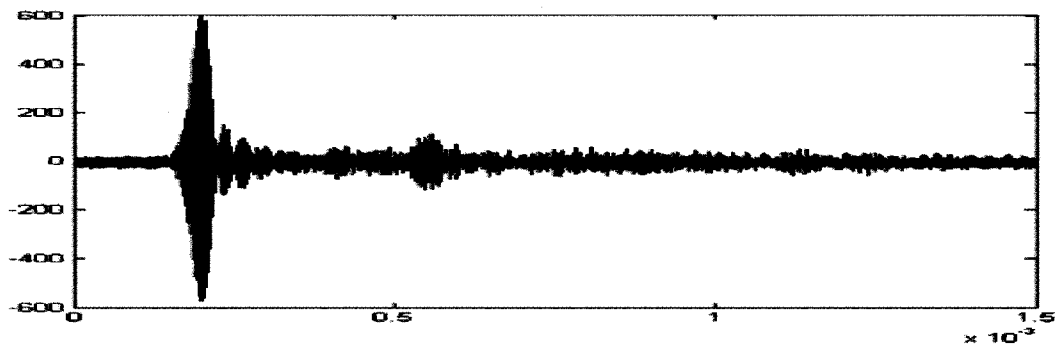
(b) Bitumastic 50
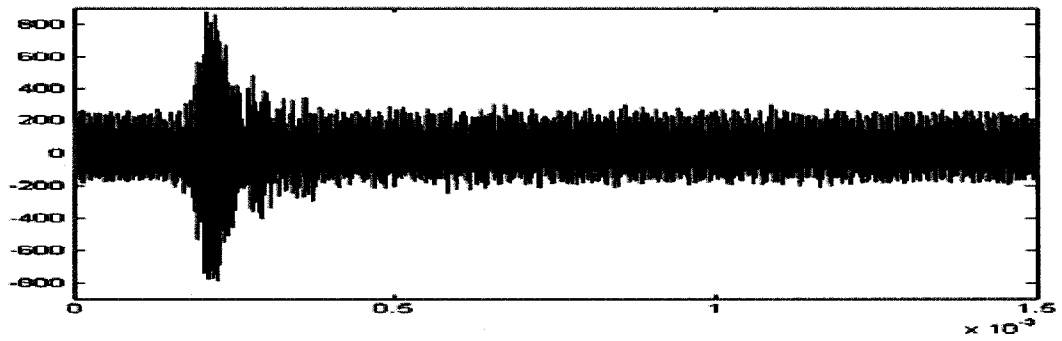
(c) Protal 7200 + Bitumastic 50

Figure 3.36: Three sample waveforms from three different coatings.

84

(a) HBE - 95
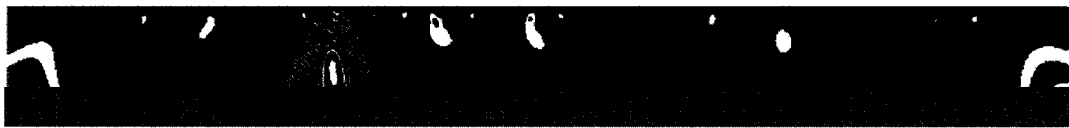
(b) Bitumastic 50

(c) Protal 7200 + Bitumastic 50

Figure 3.37: Three sample thumb prints from regions of the plate with three different coatings.

the coatings attenuating the signals some.

Using a SWT to remove three levels of details before applying the DWFT with the 'gaus2' mother wavelet we obtain thumb prints containing a triangular feature for each of the coatings (Figure 3.37). The thumb prints show some interesting features. The Bitumastic 50 feature is very clean without any other mode features present, while the two epoxy samples indicate the presence of other modes. Of the three, the Bitumastic 50 is the first arriving, followed by the HBE-95 and finally the Protal 7200+Bitumastic 50. Drawing from Table 3.4 we suspect that this mode feature corresponds to the S0 guided wave mode. As thought, the arrival times for the epoxy coated samples are delayed when compared to the pipe wall alone. The earlier arriving guided wave modes seem to be very attenuated in the coatings. The steel dispersion curves indicate a slowing of the S0 mode, this would correspond to the triangular feature moving to the right. The material property mismatch between the steel and the Bitumastic 50 seems great enough that the

elastic waves are not very affected by this layer, staying primarily in the steel pipe wall.

As the transducers are scanned down the sides of the coating samples there waveforms are collected from paths that do not propagate through the delamination before and afterwards as well as those on the edges of the flawed area and passing directly through the delamination. Figure 3.38 shows select thumb prints from the 72 step scan of the HBE-95 coated sample. As the propagation path begins to interact with the delamination the triangular feature move to the right as expected. This signifies a slowing of the mode. When passing directly through the delamination the amplitude of the signal significatly drops as well as having a later arrival at 276.8 μs. This is a drastic slowing of the guided wave mode, indicating a possible mode conversion when propagating directly through the delamination. The propagation paths that interact with the edges of the flaw seem to more closely follow what we would expect from a thickness loss. For steel this 2 mm thickness loss would be shown with a 28.8 μs delay of the arrival of the S0 mode, here we see the arrival 49 μs later at 228.9 μs. The dispersion of the this epoxy-steel system is intensified.

If we look at the same sort of progression for the Bitumastic 50 sample we see that the delamination has little effect of the arrival time of the S0 mode, but instead delamination lessens the dampening of the other modes for a portion of their propagation so we see their presence (Figure 3.39). With the guided wave energy mostly staying in the pipe wall, it makes sense that there would not be a dispersion effect in this sample. With a delamination the pipe wall does not change. Taken to an extreme, this material property mismatch can be compared to the interface between steel and water. When submerged, guided

86
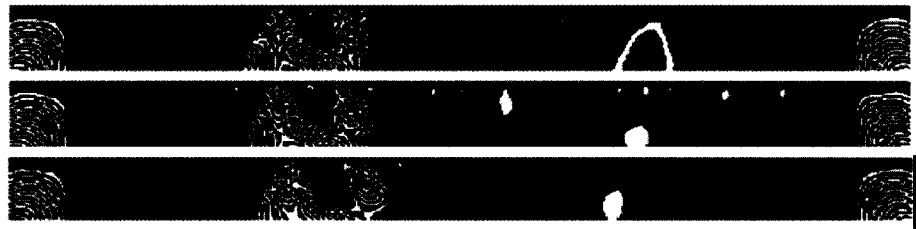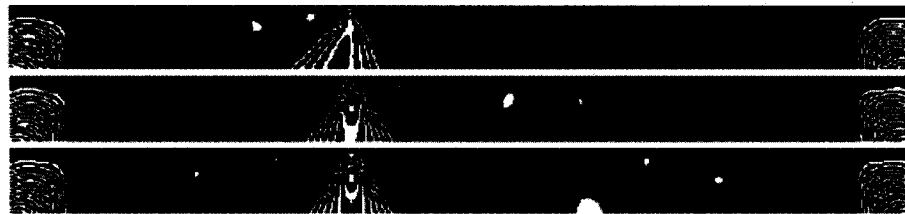
(a) Before flaw

(b) Edge entering flaw

(c) Delamination

(d) Edge exiting flaw

(e) After flaw

Figure 3.38: Thumbprints for HBE-95 scan past delamination section.

(a) Before flaw
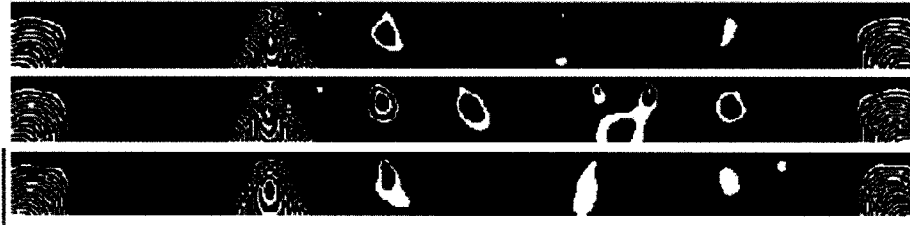
(b) Edge entering flaw
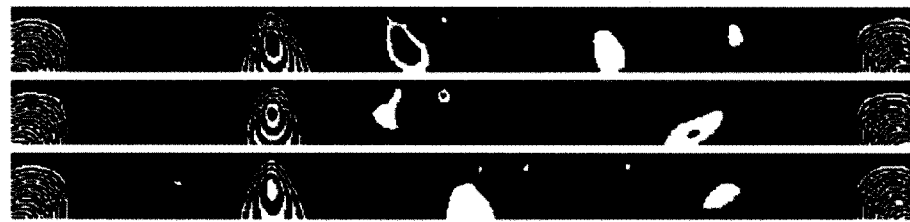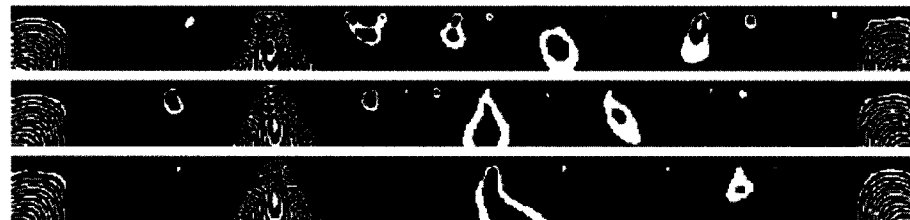
(c) Delamination

(d) Edge exiting flaw

(e) After flaw

Figure 3.39: Thumbprints for Bitumastic 50 scan past delamination section.

waves still propagate through the steel wall with little leakage into the surrounding liquid. Here there is more energy attenuated into the coal tar layer because of its viscoelastic properties. Interestingly, the amplitude of the S0 mode decreases when propagating directly through the delamination as indicated in 3.39c by the fewer ridges in the triangular feature.

Turning attention towards the Protal 7200 + Bitumastic sample we can see some of the fingerprint characteristics of both the HBE-95 and Bitumastic samples. As the parallel transducers move past the delaminated region (Figure 3.40b), we see the effect of the loss of the epoxy thickness as the triangular feature moves to the right. Just as this mode was dampened at the edge of the flaw for the Bitumastic 50 coating by itself we see the ridge count drop here as well. We also see the presence of a possible mode conversion since the delay of the guided wave mode when propagating directly through the flaw is so great. The amplitude here is once again drastically diminished from the signal with the unflawed coating. The similar results for the two coating sections with epoxy coatings indicate the the viscoelastic material properties for these two epoxy layers are similar. There also seems to be a fairly large disconnect between the guided waves propagating directly through the epoxy delaminations. The manufactured delamination creates a step function in the thickness of the plate, this could result in a mode conversion to a much slower propagating mode. This could also be evidenced by edge effects of the delamination. The edge effects are present because of the large beam width of the guided waves. For these tests we used 500 kHz, 1" contact transducers, the large crystal size is needed because of the lower frequency. When more and more of the beam is propagating through the delamination, it affects more and more of the guided wave energy which translates to the gradual movement of the
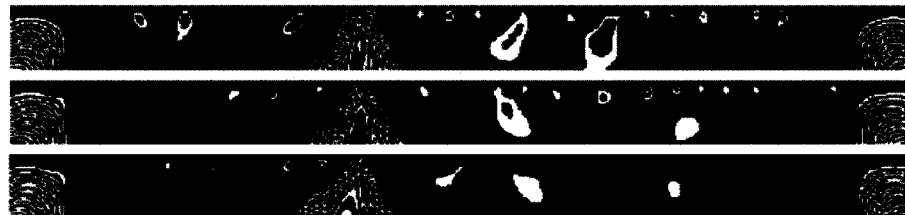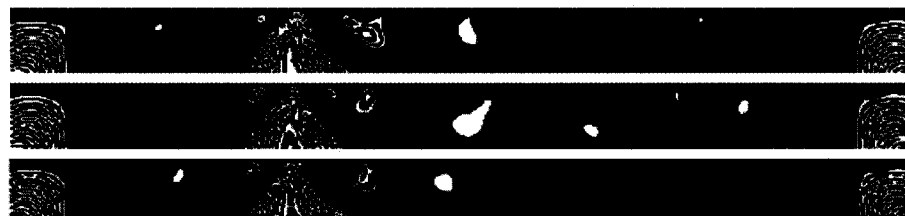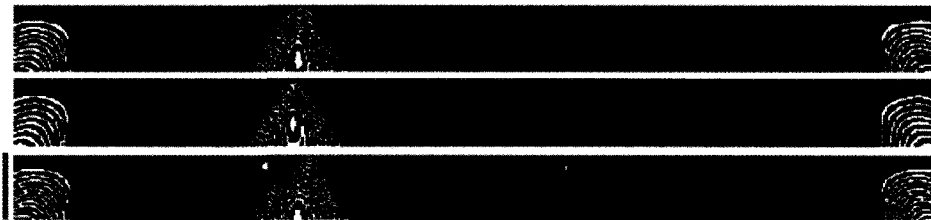
(a) Before flaw
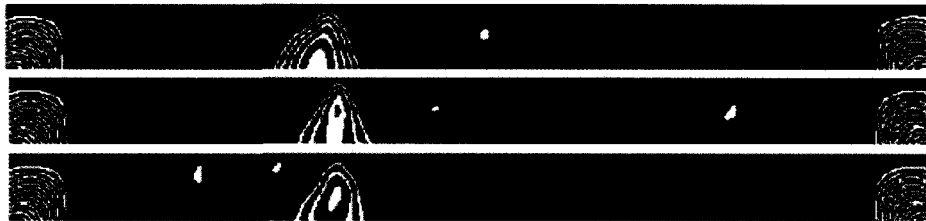
(b) Edge entering flaw
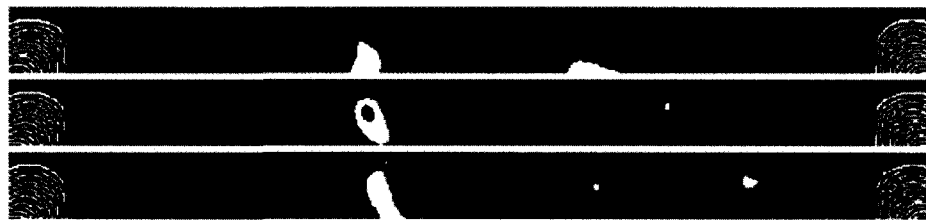
(c) Delamination

(d) Edge exiting flaw
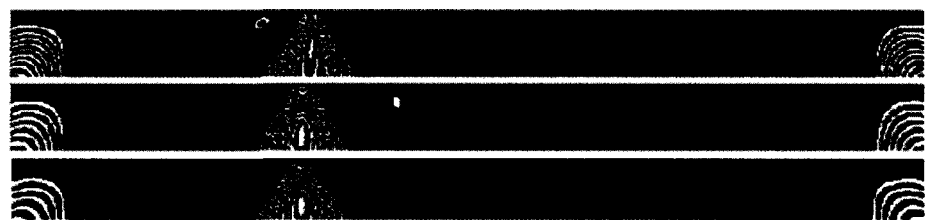
(e) After flaw

Figure 3.40: Thumbprints for Protal 7200 + Bitumastic 50 scan past delamination section.

(a) No visible flaw

(b) Propagating through ground flaw
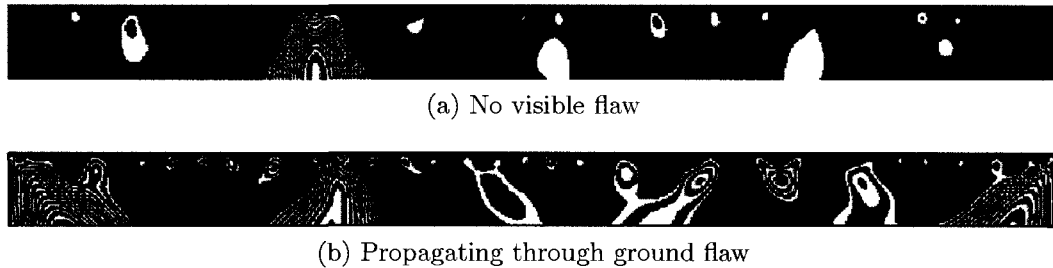
Figure 3.41: Thumbprints derived from lengthwise experimental test of the DOT pipe sample

triangular feature to the right.

We are confident that we can identify the effects of a delamination under the epoxy coatings from the plate experiment. The question is what happens to the signals and DWFT features when we return to the DOT real pipe sample. As mentioned before, this sample has many different flaws, the ground flaw (Figure 3.32) is of particular interest at this time. The ground flaw only as thick as the the double protective coating. The steel is very close to its original thickness. With the same parameters as the plate tests, we were able to record waveforms lengthwise down the pipe first in an area of the pipe surface that did not have any visible damage followed by propagation through the grounded area. This area has the same approximate size as the delaminations under the coatings on the plate test piece. Figure 3.41 shows the resulting thumb prints for the test propagation length of 431.8 mm. Once again we see the shift to the right of the large triangular feature when the guided waves are propagating through the flaw. The more gradual thinning flaw, the shifts arrival time which coincides with the our original notion that the guided waves in the coating-pipe system mimic those of the steel pipe itself. It is also noted that the plate coatings were made in our lab, so the thickness that we could uniformly achieve was 2 mm, while the epoxy

91

coating on the pipe sample is much thinner with the combined thickness of the epoxy and coal tar being 1 mm. The difference in effective thickness loss accounts for the decrease in magnitude of the arrival shift.

This section described an experimental approach to the extraction of guided wave mode arrivals in order to gain quantitative information about the test piece. We've found that the DWFT algorithm could show differences between unknown coatings as well as identify the presence of delamination and grinding flaws in the propagation path. Combined with complex multi-layered models to help identify the guided wave feature changes, this extraction algorithm can be used for the detection of hidden flaws under a variety of protective coatings without having to disturb the coating and/or pipeline usage. For systematic studies of a wider range of materials and flaw sizing and positioning relative to the transducers we can employ computer simulations. Experimental samples could always have more flaws present than intended, but when trying to develop a system for inspection, it is important to fully understand the model being worked with. Computer simulations allow for just this case, and although it is idealized we can always step back to experiment for bench marking . The simulation space would allow the researcher the needed control over flaw dimensions and placement with respect to the transducers for the development of a robust flaw detection system.

3.3   Aircraft Stringers

Our final NDE application addresses the national fleet of aging aircraft. The question: is it reasonable to keep repairing the old aluminum aircraft or is it to build new structures? In this industry, as with most industries, the end of

the argument is in the bottom line. Whichever solution will be the most cost effective is the one that will win out in the end. We find that the reliability of the maintenance depends on whether or not we can accurately diagnose problem areas fast and cheaply. Repairing aircraft is a challenge because some problem areas are concealed inside the skin of the aircraft or under a coating. It is wasteful to take apart sections of the airplane just to find that they do not need repair. New construction also has its own issues with maintenance and repair. These arise when deciding which materials to use in the construction. Composites are strong and lightweight and as such give competition to aluminum airframes. Aluminum companies must reduce the weight of their product in order to still be attractive to aircraft manufactures. Reducing the weight of the aluminum actually translates to reducing the amount of aluminum that is used in the structure. We can place sensors to track structural integrity instead of over engineering the structure. Some of the structural pieces of interest in this work are the airframe stringers. Airframe stringers are one of the main structural components to which the outside skin is attached. In key locations which are susceptible to corrosion, an ultrasonic guided wave system would be ideal for monitoring large areas quickly without taking apart the structure.

The research presented in this section deals with our efforts to understand the wave propagation in airframe stringers and their interaction with corrosion and thickness loss flaws. First using an incremental thickness loss experiment and then an accelerated corrosion test, we consider the changes in mode arrivals. In each case we again employ the DWFT to extract mode arrivals.

The stringer samples provided by Alcoa are made of a special high-strength aluminum alloy, Al 2024 T3511, in which copper is the major alloying element

along with a small magnesium content. The approximately 4% copper and 1.5% magnesium provide increased strength and work-hardening characteristics. However, due to the higher copper content, this alloy is less resistant to corrosion. Minute copper particles on the surface and grain boundaries of the alloy create small galvanic cells in the material. The copper is more noble than the aluminum so it has potential to reduce the adjacent aluminum, causing corrosion. As this intergranular corrosion continues, the copper ions replate themselves on the alloy increasing the corrosion rate. This is why the temper, T3511, and work-hardening are important, the heat treatment can affect the amount, size and distribution of the intermetallic precipitates [67]. In extruded structures, the grains become elongated down the length of the structure so the intergranular corrosion proceeds in a exfoliating manner. The grain boundaries expand, flaking off mostly non-corroded layers in a fashion that we can model as a thinning of the plate-like structure.

The sample aluminum stringers used are 1m in length and have a "T" cross-section. The original flange thickness was 1.6 mm. We used piezoelectric shear wave contact transducers in a pitch-catch arrangement to inspect the samples. The transmitting transducer, aligned in the shear vertical (SV) configuration where the polarization of the PZT crystal is parallel to the length of the stringer, excites Lamb wave modes that are then recorded by the receiving transducers. Since the Lamb wave modes are dispersive, the presence of a flaw shifts the arrival times and amplitudes of the Lamb wave modes received. For thinning flaws, we expect that the faster S0 mode will speed up while the slower A0 mode will gradually slow down with increased thinning (Figure 3.42).

We began investigating the interaction of the guided waves with the stringers by doing a experimental propagation study to examine how the modes separate
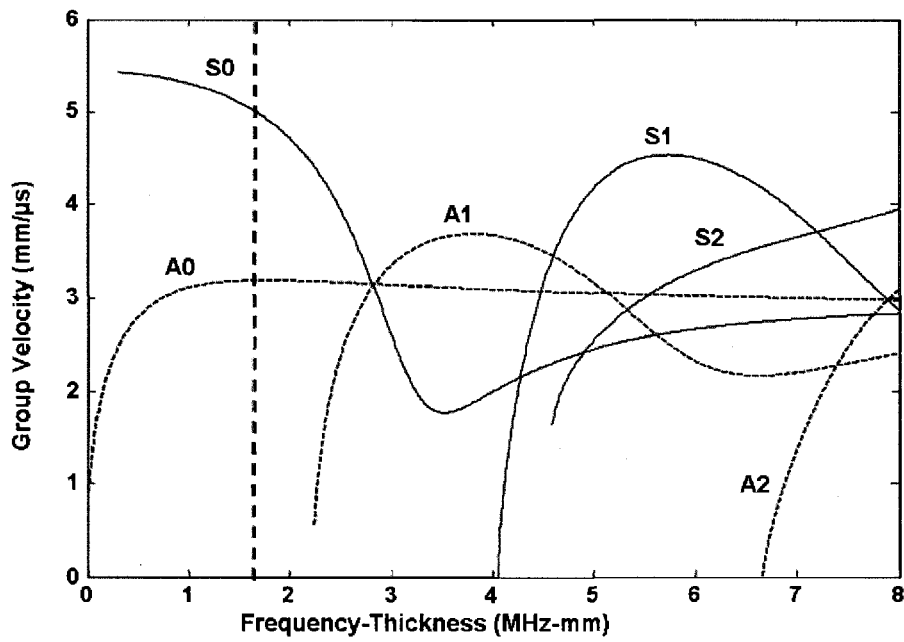
Figure 3.42: Aluminum dispersion curve. For a frequency-thickness product of 1.6mm-MHz (dotted line) we expect the arrival of 2 guided wave modes, S0 and A0.
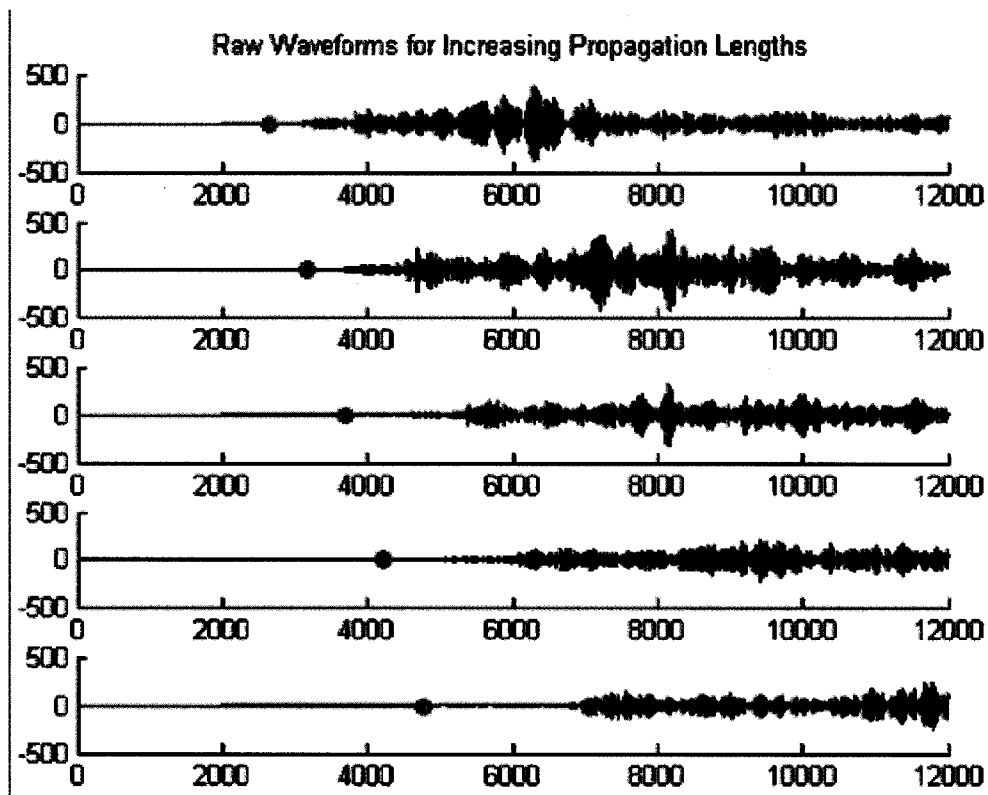
Figure 3.43: Waveforms recorded for propagation lengths from top to bottom of 50, 60, 70, 80, and 90 cm respectively. The red and blue dots indicate the expected S0 and A0 positions.

out in time as they propagate. This study was useful to familiarize ourselves with the waveforms. Recording signals for increasing lengths along the same structure allows us to be confident that we are picking out the desired guided wave modes from the complex waveforms. Figure 3.43 shows the raw time series signals produced from a 5 cycle 1.4 MHz tone burst, recorded at a 25MHz sampling rate. The propagation distance increases from the top signal of 50 cm in 10 cm increments to 80 cm. Here the red and blue dots correspond to the expected positions of the S0 and A0 modes for each propagation length. From looking at these waveforms it is hard to isolate the individual guided wave modes so we

96
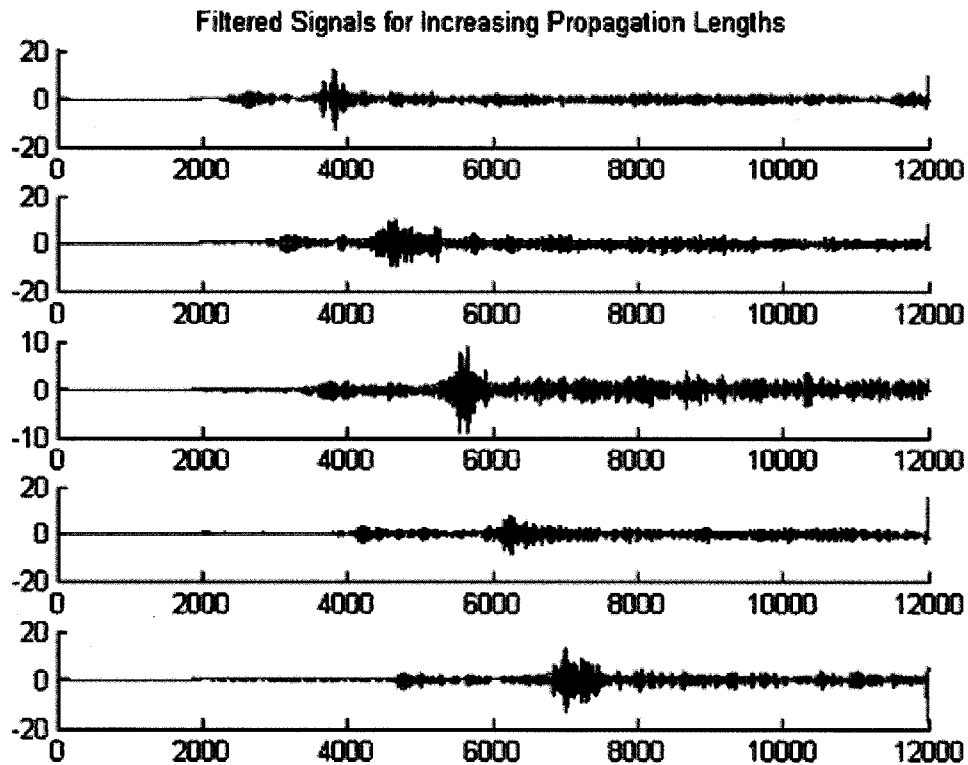
Figure 3.44: Propagation study filtered data. The green line shows the result from a enveloping technique that is passed to the DFWT. The red and blue dots indicate the expected S0 and A0 positions.

pass the data through a SWT filter, the filtered signal is shown in Figure 3.44. Now we can start to pick out the desired guided wave modes from the filtered signals and can see that they separate out as expected. If we pass the filtered signal through an enveloping scheme and finally the DFWT we can easily locate the modes (Figure 3.45). In these images the thumb print has been expanded to match the raw time series spacing. The triangular feature to the left indicates the start of gated time series signal. The first arriving S0 mode is the next feature to the right with a single hemisphere feature while the A0 feature has a doublet hemisphere located further to the right. This propagation study proves that we

97
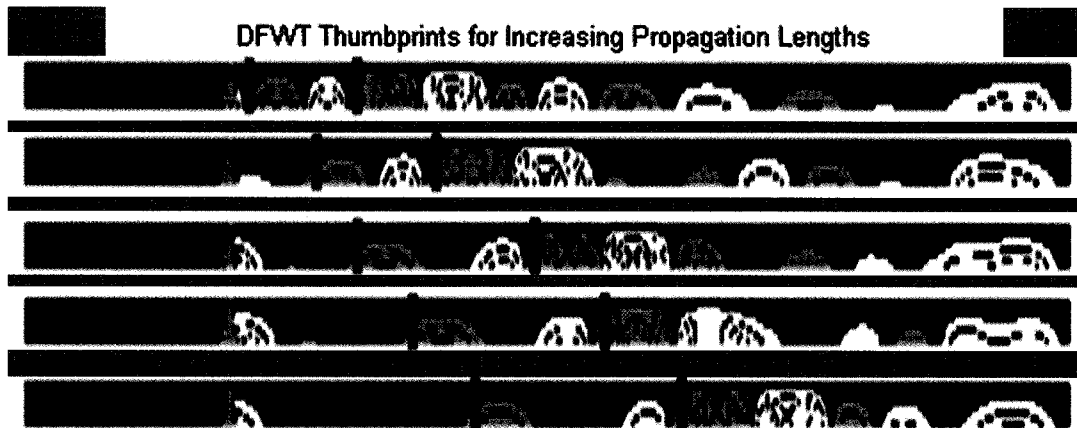
Figure 3.45: Propagation study DWFT thumb print images show the separation in time for further propagation distances. The triangular feature to the left indicates the beginning of time series data while the S0 and A0 modes are shown by the single hemisphere and doublet feature respectively.

can distinguish and extract the guided wave modes from the raw data collected from the airframe stringer structure. Using this knowledge we can move on to examining how these mode interact with flaws.

3.3.1 Incremental Thickness Milling

Our first step in looking at thinning flaws on the stringers consisted of simulating the effect of corrosion. By incrementally decreasing the thickness of the stringer flange with a milling machine, we know precisely how much material we are removing at each step. Setting the stringer on the table it looks like an upside down "T". The milling increments were taken from the middle 40 cm of the bottom flange, from the outside edge 21.5 mm towards the web. Figure 3.46 shows the thickness versus mill step. Which gives us the expected velocities for the guided wave modes as they travel through the flawed section in each step. Figures 3.47a and 3.47b show the expected velocities of the guided wave modes through the

98
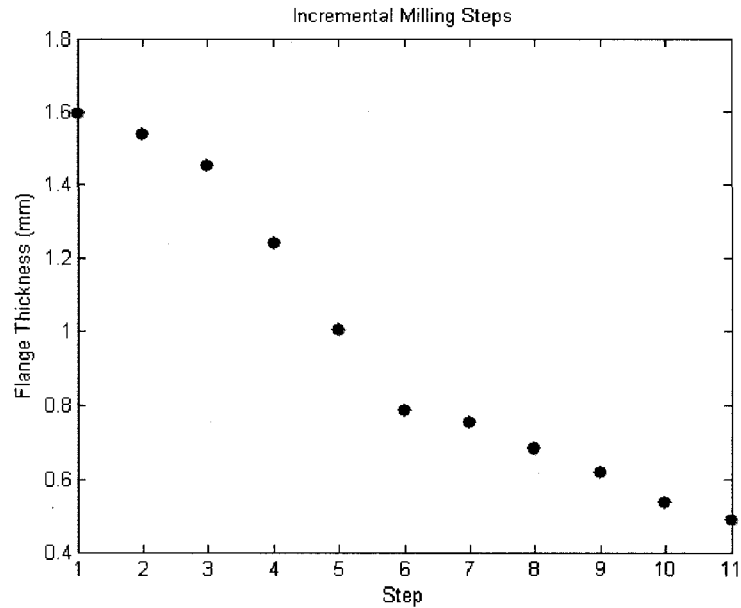
Figure 3.46: The incremental milling tests consisted of 10 steps, each removing another layer from the middle 40 cm of the bottom flange.

milled section of the stringer.

For the tests, the transducers were placed 10cm from the ends of the stringers in an effort to separate the reflections from the ends out in time from the signal that we care about. We also placed modeling clay on the ends of the stringer to damp out some of the standing waves that develop in the laboratory atmosphere. The total propagation length was 80cm with the 40 cm flaw in the middle.

We approached the challenge of picking out the modes in the same fashion as in the propagation study. Here we show the raw waveforms from the 10 incremental milling steps (Figure 3.48). Then passing the resulting filtered envelop through the DFWT we obtain similar thumb prints to the propagation study (Figure 3.49). In these images the triangular feature to the left is once again an indication of the start of the filtered envelop. The doublet hemisphere feature of the A0 mode

99
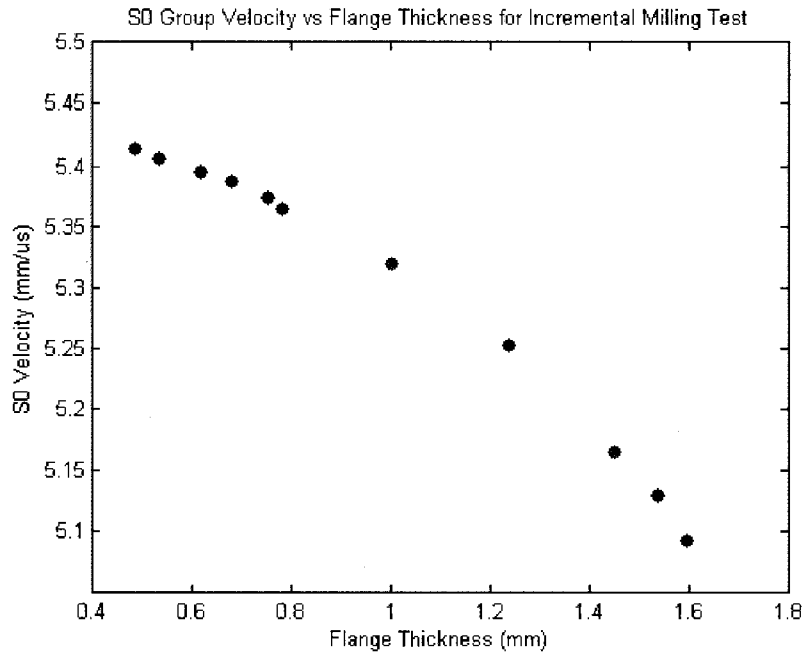
(a) S0 velocity versus flange thickness
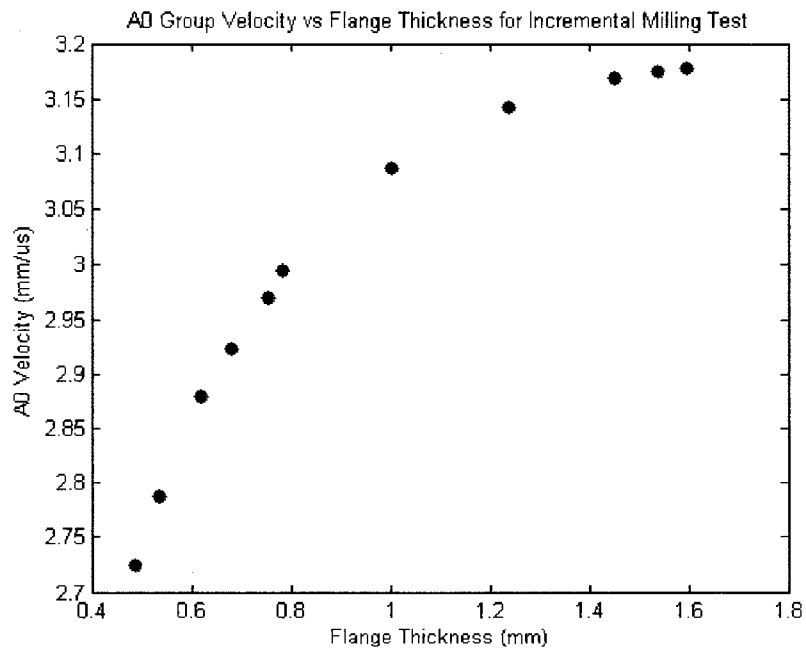
(b) A0 velocity versus flange thickness

Figure 3.47: The S0 mode speeds up as layers are milled from the flange of the stringer. The A0 mode slows down as layers are milled from the flange of the stringer.
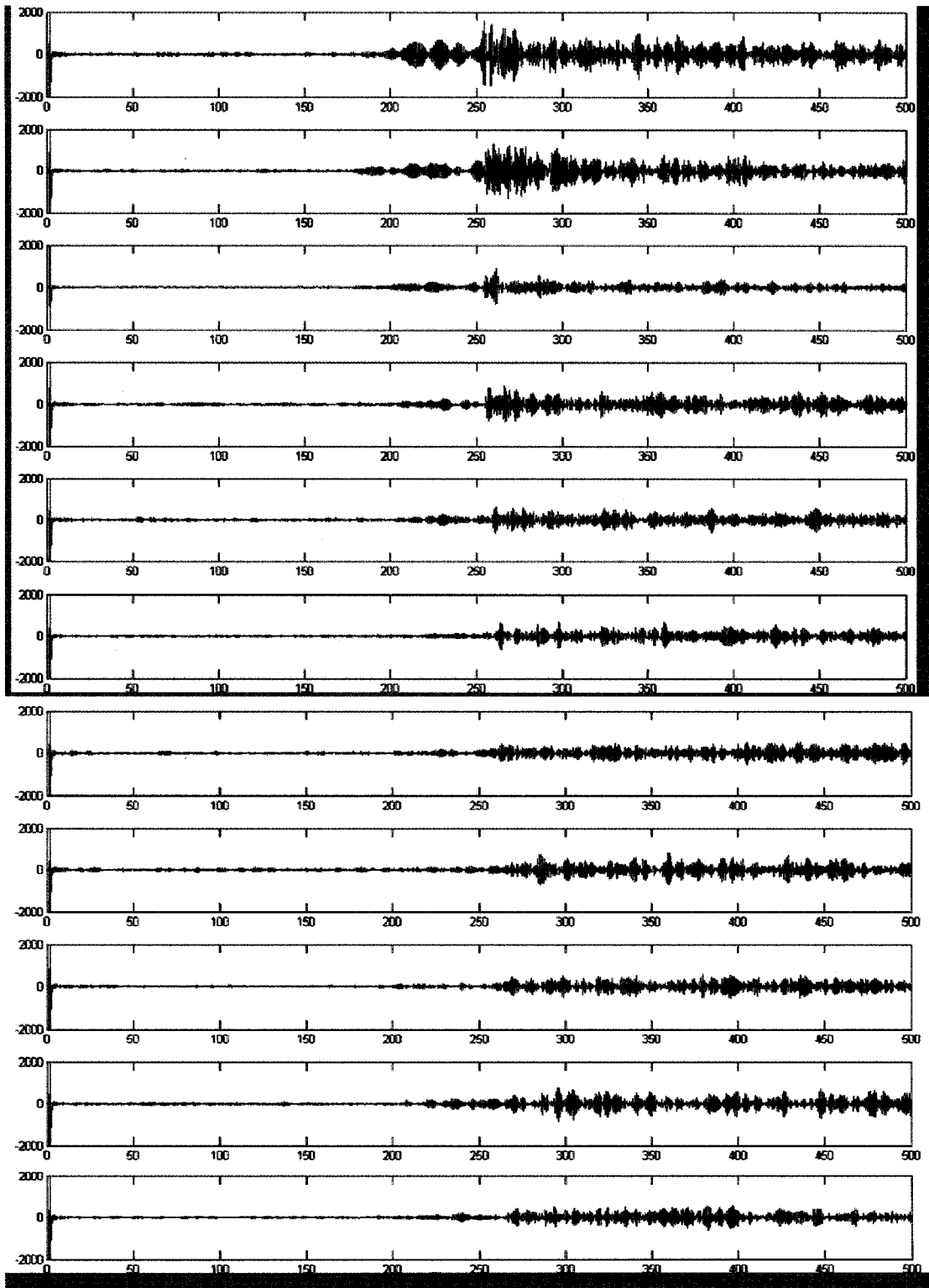
Figure 3.48: Raw data from incremental milling steps from top down.

is fairly well pronounced however we seem to lose the feature of the S0 because its propagating amplitude is not very large. However, since we are concerned with extracting accurate arrival times from the signals and not just picking out the presence of the modes we can take a closer look at the parts of signals that contain the modes themselves. By looking at the signals received we can notice that the A0 mode is more dominant than the S0 mode so we will turn our attention to the A0 at this time, altering the DFWT parameters to extract the arrival times.

We show the new progression of the data processing in Figure 3.50. This progression follows in the usual way starting with a SWT, then windowing a portion to pass to the DWFT algorithm to find the fingerprints. The window was determined using the expected arrival time for the A0 mode. Figure 3.51 shows the binary fingerprint images produced from the incremental milling tests. The top image is for the un-milled clean sample. In each of the images, a double circular feature was automatically extracted, indicated by the vertical blue lines. As material is removed from the flange, we would expect from the dispersion curves that the A0 mode would slow down. In these images a slowing of the mode would mean a later arrival time and a shift of the feature to the right. It can be seen in the images, the feature shifts right. Furthermore the movement of the double feature corresponds to the arrival time of the A0 mode. The extracted arrival times are labeled to the left. If we calculate the expected arrival times using the mode velocities from the dispersion curves (Figure 3.47b), taking into account that the waves are only traveling through the thinned region for half of the propagation length, we can compare to our experimentally extracted arrival times. As see in Figure 3.52 the extracted arrival times match the expected arrival times. As material is removed the extracted A0 mode arrival (blue dots) is delayed
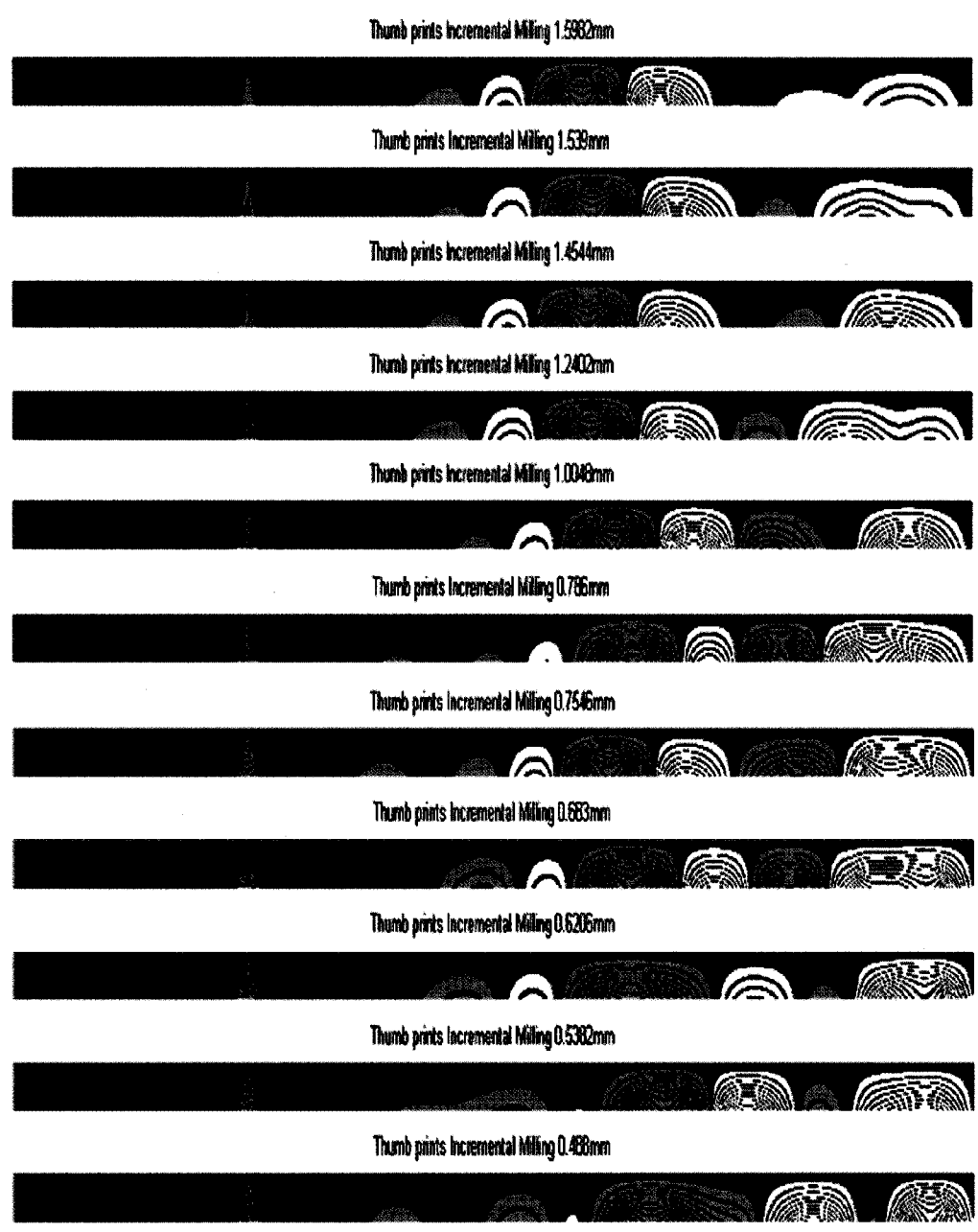
Figure 3.49: Thumb prints generated from the incremental data using the DWFT algorithm developed in the propagation study of the aircraft stringers.
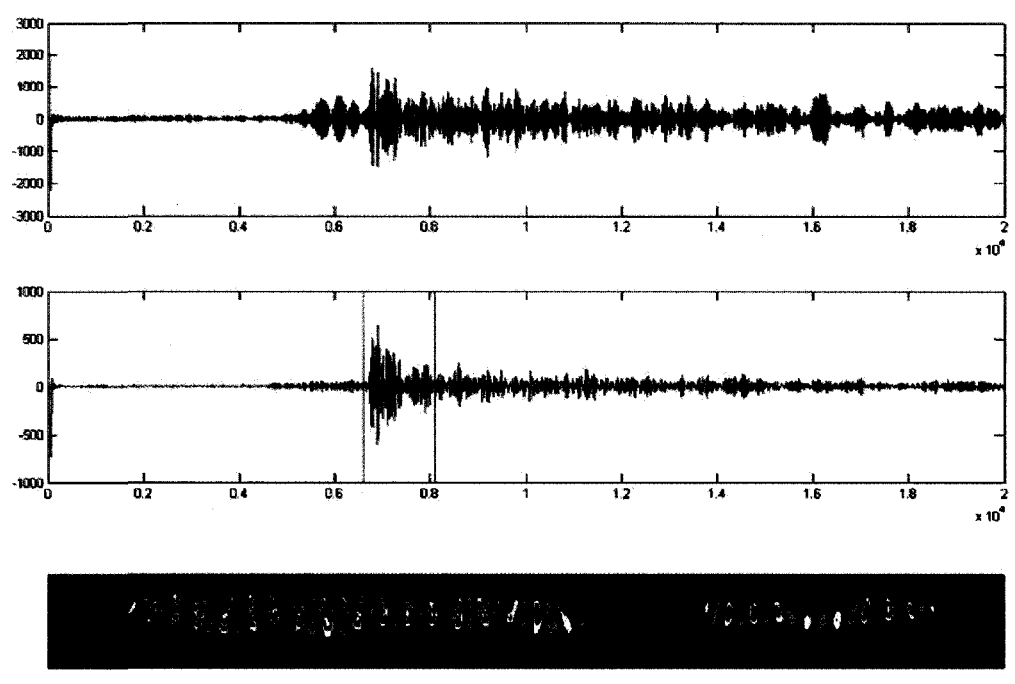
Figure 3.50: (Top) Raw waveform collected from clean, un-milled sample. (Middle) Filtered waveform using a discrete stationary wavelet filter. (Bottom) Extracted wavelet fingerprint for the A0 mode.

Figure 3.51: Material was removed incrementally from top to bottom with. Fingerprints show the automatically extracted A0 arrival, depicted by the red lines. The arrival time is noted to the left.
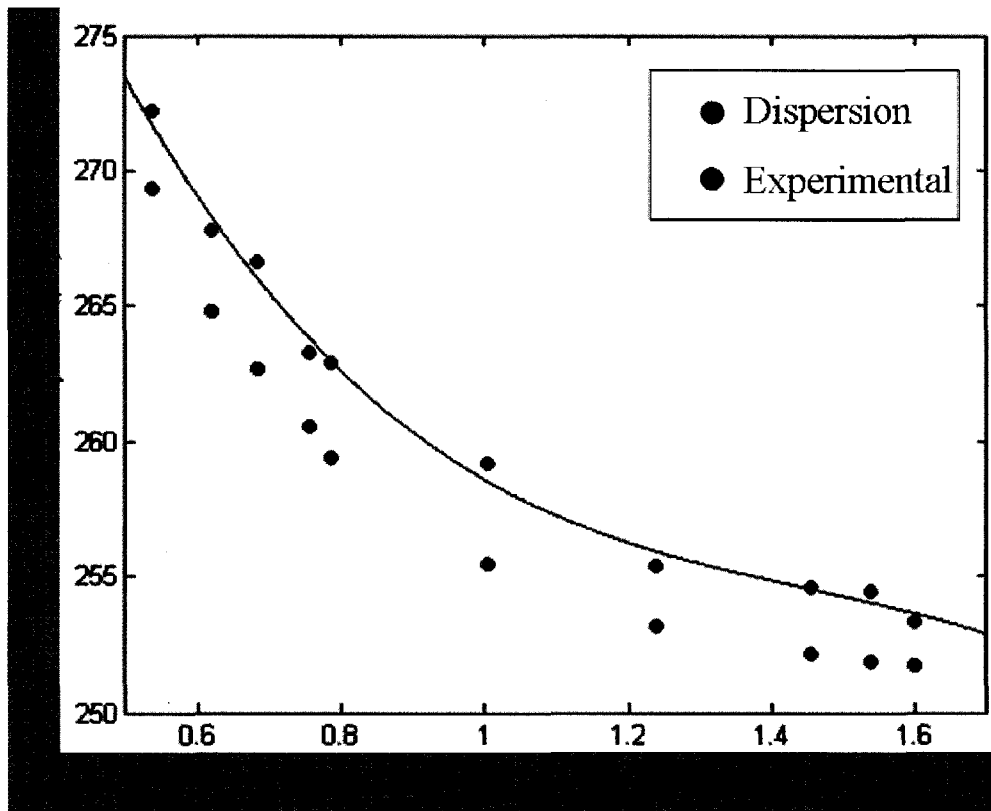
Figure 3.52: Incremental milling test comparison of A0 arrival times to the expected. The black dots show the expected arrival time for each thickness step while the blue dots show the extracted arrival time from the DFWT thumb prints.

in accordance with the expected slowing of the A0 mode (black dots).

Now that we have a good indicator of the change in mode velocity and arrival time we can look at our accelerated corrosion tests to find similar trends.

3.3.2 Accelerated Corrosion Test

In order to study the interaction between the guided waves and a more real world sample we set up an accelerated corrosion test in which we introduced corrosion on a portion of the flange of the stringer. To keep in accordance with the incremental milling tests, we masked off the test section leaving the middle 40 cm of the flange to be corroded. The accelerated corrosion test follows an ASTM standard test method known as the EXCO test [68]. This test is specially designed to corrode high-strength 2XXX and 7XXX series aluminum alloys. The solution is made up of sodium chloride, potassium nitrate, nitric acid and hydrogen peroxide for added acceleration. The EXCO solution produced an exfoliation form of corrosion which flakes off layers of the exposed surface. Our procedure was to record baseline waveforms, apply the EXCO solution to the test area then collect data every 12 hours. Data collection consisted of recording a waveform with the EXCO solution still on the surface, then putting the sample in a nitric acid bath to remove corrosion products then collecting another waveform before taking multiple thickness measurements. After data collection for a particular timestep, we reapplied the EXCO solution to sit for another 12 hours. Figure 3.53 shows a close up of the final extent of the corrosion.

The excitation and treatment of the guided waves were the same as for the milling tests. The contact transducers were placed 10cm from each of the ends of the 1m "T" stringer. However, the raw waveforms from these tests were much
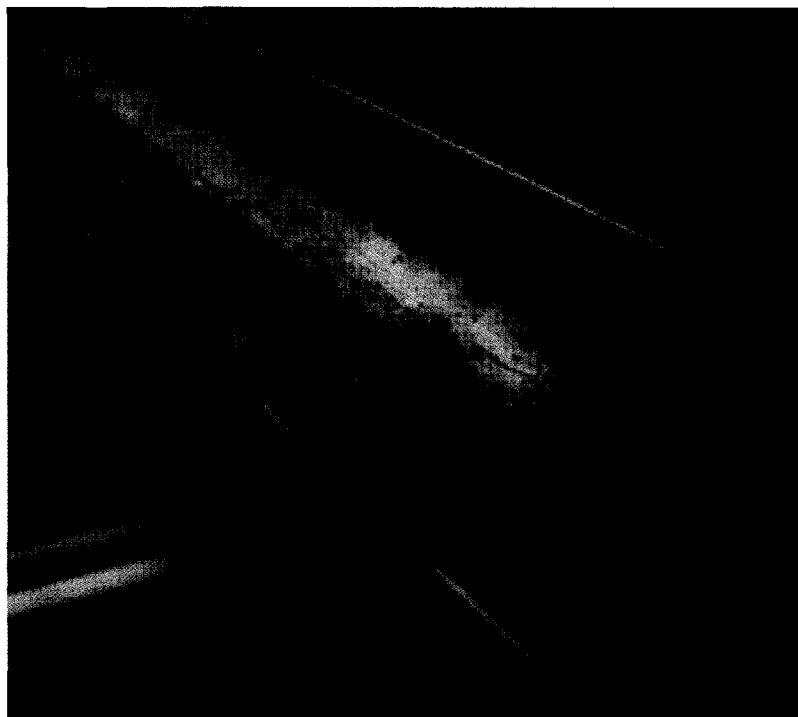
Figure 3.53: This is a close up of the final extent of the exfoliated surface of the "T" stringer. Result from 14, 12 hour cycles using the EXCO solution.

more complex than from the incremental milling tests. This is because of the nature of the exfoliation, each of the flakes becomes a scatterer of the elastic wave energy. We recorded data from both the fluid loaded stringers as well as after the rinse. Since we wish to compare results to our milling tests, here we included some of the raw waveforms after the rinse (Figure 3.54).

Once again from these raw signals we can not extract the useful mode information that tells us the extent of the thickness thinning corrosion. So using the a window of the SWT filtered signal (Figure 3.55) we can employ the DFWT developed with the incremental milling test to identify arrival information of the A0 mode. The resulting thumb prints are similar to those from the previous tests. Figure 3.56 shows the the progression of the accelerated corrosion in the thumb prints. Indicated by the blue lines, we see that the automatic extraction of the same double circular feature as was found in the milling tests shift around a arrival of 250 μs. It is also interesting that after the first few 12 hour corrosion shifts, we see a split of the the features that make up the S0 mode. The red lines in Figure 3.56 are placed on the first feature that goes from a left leaning inclination to the right, signifying the start of another possible mode. If we look at a plot of all of these extracted times verses 12 hour step (Figure 3.57) we see that there is a split between the the two feature extractions. The blue seems to stay for the most part at the arrival time of the original thickness while the red slows down dramatically.

In order to discern if there is actually a splitting of the A0 mode we have to understand more fully how the wave is propagating in this built up "T" structure better. This structure is more complicated than just the theoretical plate model that is used to compute the dispersion curves used in this section for the
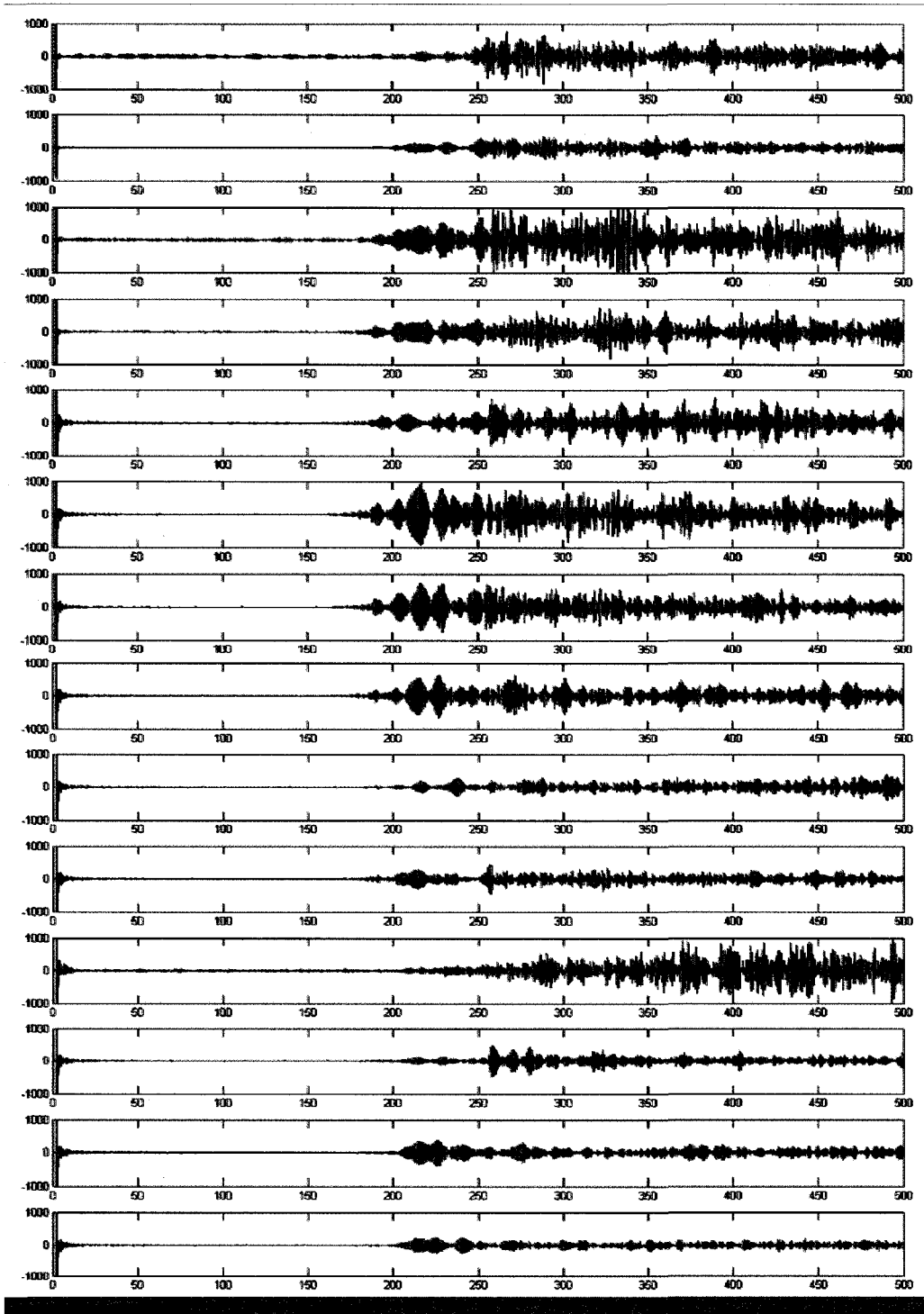
Figure 3.54: From top to bottom we have the collected time series waveforms from the accelerated corrosion tests where each of the waveforms represents 12 hour exposure to the EXCO solution on half the propagating surface of the "T" stringers.

110
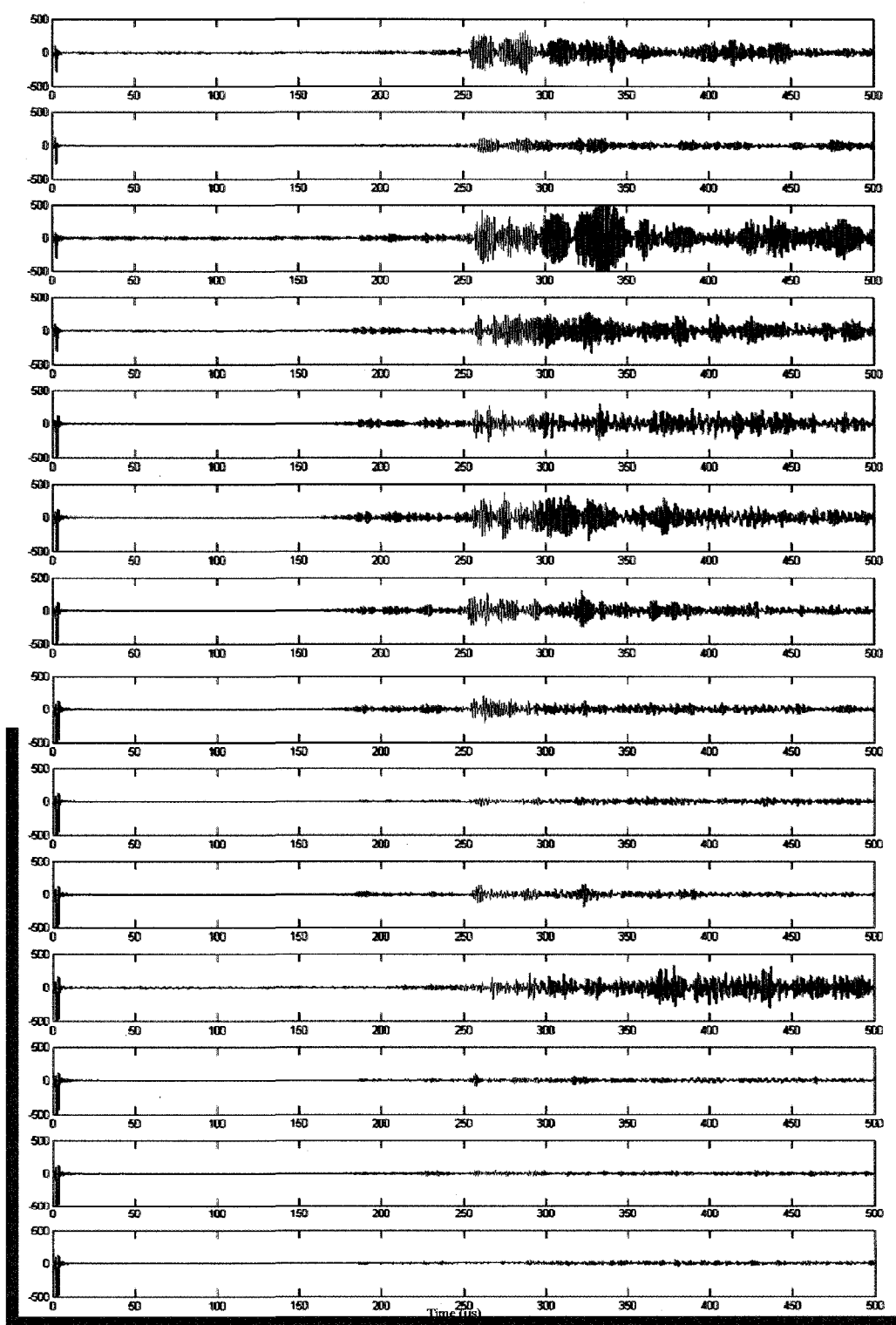
Figure 3.55: Wavelet filtered signals for 3.54 data. The portion shown in red is the window around the expected A0 arrival.

111
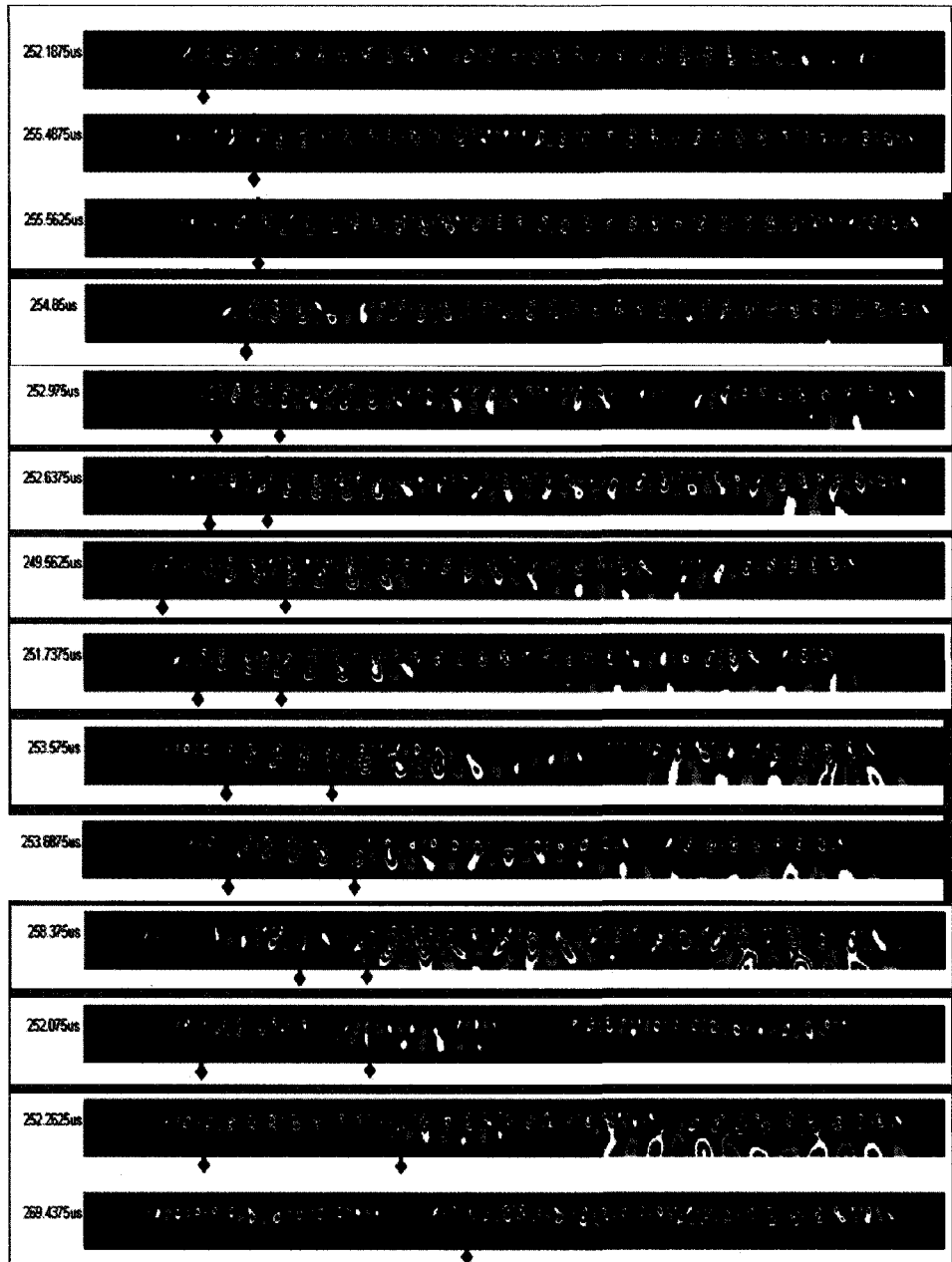
Figure 3.56: Twelve hour increments of accelerated corrosion EXCO test from top to bottom represented in thumb prints obtained by the DWFT. The blue vertical lines indicate the automatic extraction of a double circular feature from the thumb prints. The red lines indicate a second feature of interest that appears to split off from the first with increased corrosion.
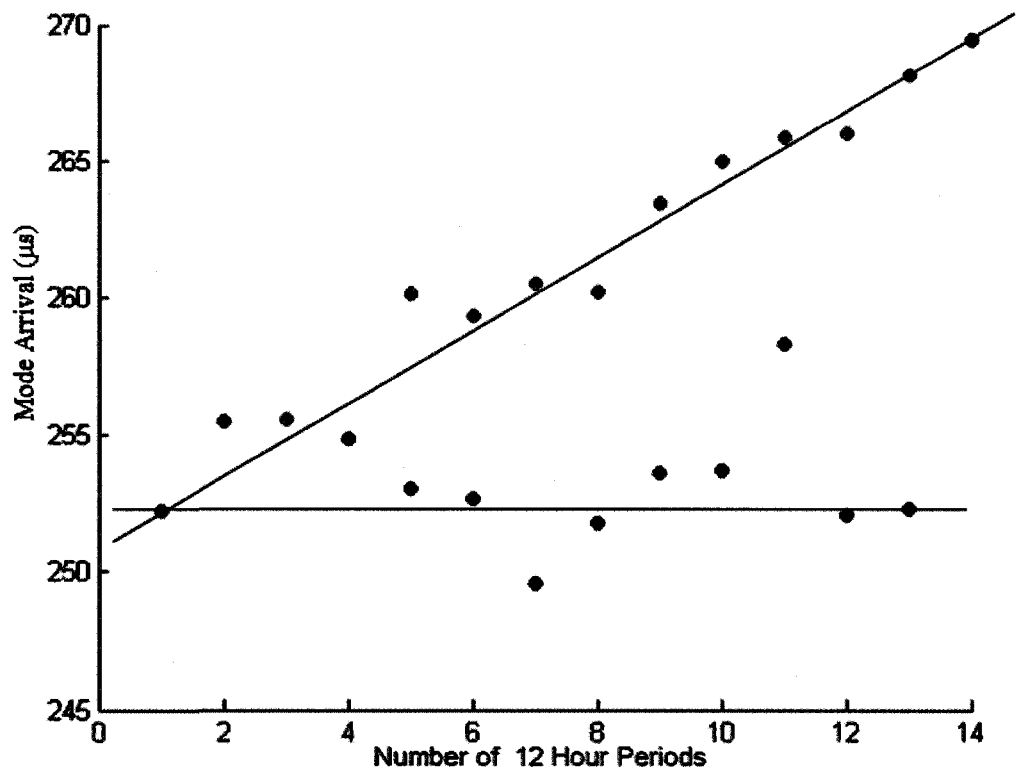
Figure 3.57: Corrosion time verses Extracted arrival of the A0 mode for the EXCO accelerated corrosion tests. The blue and red arrival times seem to indicate a splitting of the mode between the original arrival time (blue) and the a mode propagating through the thinning material (red).

approximate expected arrival times for the modes. Here we not only have the reflections from the top and bottom surfaces of the flange, but its width and the presence of the web also affect how the elastic energy propagates along the stringer. One method for taking all of these effects into consideration is by using full field modeling techniques, which are discussed the next chapter.

Chapter 4

EFIT Simulations

Our experimental approach to guided wave interpretation has brought us a long way towards developing practical techniques to find anomalies in plate-like and pipe-like structures. However, when dealing with complex, built-up structures like those found in real world practice, we need to understand the elastic wave propagation more deeply than for the idealized case of a thin plate or pipe. In order to start this task we developed parallel three-dimensional (3D) numerical simulations using the finite integration technique.

4.1 Basic Equations

The elastodynamic finite integration technique (EFIT) evolves from the basic wave equations for elastic solids [50]. We start with Hooke's law and Cauchy's equation of motion to give the fundamental equations. The differential form of the equation of motion

$$\rho \dot{v}_x = \frac{\partial \sigma_{xx}}{\partial x} + \frac{\partial \sigma_{xy}}{\partial y} + \frac{\partial \sigma_{xz}}{\partial z} + f_x \qquad (4.1)$$

115

$$\rho \dot{v}_y = \frac{\partial \sigma_{xy}}{\partial x} + \frac{\partial \sigma_{yy}}{\partial y} + \frac{\partial \sigma_{yz}}{\partial z} + f_y \qquad (4.2)$$

$$\rho \dot{v}_z = \frac{\partial \sigma_{xz}}{\partial x} + \frac{\partial \sigma_{yz}}{\partial y} + \frac{\partial \sigma_{zz}}{\partial z} + f_z \qquad (4.3)$$

and the first time derivative of Hooke's law in differential form

$$\dot{\sigma}_{ij} = \lambda \dot{\epsilon}_{kk} \delta_{ij} + 2\mu \dot{\epsilon}_{ij}, \qquad i,j = x,y,z \qquad (4.4)$$

where we sum over the repeated index k and

$$\dot{\epsilon}_{xx} = \frac{\partial v_x}{\partial x}, \dot{\epsilon}_{yy} = \frac{\partial v_y}{\partial x}, \dot{\epsilon}_{zz} = \frac{\partial v_z}{\partial z},$$

$$\dot{\epsilon}_{xy} = \frac{1}{2}\left(\frac{\partial v_y}{\partial x} + \frac{\partial v_x}{\partial y}\right), \dot{\epsilon}_{xz} = \frac{1}{2}\left(\frac{\partial v_z}{\partial x} + \frac{\partial v_x}{\partial z}\right), \dot{\epsilon}_{yz} = \frac{1}{2}\left(\frac{\partial v_z}{\partial y} + \frac{\partial v_y}{\partial z}\right)$$

give the components of the velocity vector, v_i, and the stress tensor, σ_{ij}, for a particle in the elastic solid. Here, the the material is defined by the Lamé constants λ and μ and the material density ρ. The source terms are represented by f_x, f_y, f_z in the velocity terms.

Now that we have described the displacement and stress of a particle in an elastic solid, we need to expand to the entire solid. If we look at the particle as a small cubic cell, we can think of the solid as many cells next to each other. From here we have to place all the components on the small cell. After careful consideration of continuity of displacement and stress, it is evident that there is only one arrangement of the components that will yield the desired results [50]. We place the velocity components on the edges of the cell with the diagonal elements of the stress tensor on the corners and the off-diagonal elements on the faces of the cell. Using this component placement found in Figure 4.1 we can then discretize

Figure 4.1: This is the unit cell for the elastodynamic finite integration technique. The velocity components are placed along the edges of the cell while the diagonal elements of the stress tensor are placed on the corners and the off-diagonal elements on the faces of the cell.

(4.1) - (4.4) as follows

$$\rho \dot{v}_x^{(n)}(t) = \frac{\sigma_{xx}^{(n+\hat{x})}(t) - \sigma_{xx}^{(n)}(t)}{\Delta x} + \frac{\sigma_{xy}^{(n)}(t) - \sigma_{xy}^{(n-\hat{y})}(t)}{\Delta y} + \frac{\sigma_{xz}^{(n)}(t) - \sigma_{xz}^{(n-\hat{z})}(t)}{\Delta z} + f_x(t)$$

$$\rho \dot{v}_y^{(n)}(t) = \frac{\sigma_{xy}^{(n)}(t) - \sigma_{xy}^{(n-\hat{x})}(t)}{\Delta x} + \frac{\sigma_{yy}^{(n+\hat{y})}(t) - \sigma_{yy}^{(n)}(t)}{\Delta y} + \frac{\sigma_{yz}^{(n)}(t) - \sigma_{yz}^{(n-\hat{z})}(t)}{\Delta z} + f_y(t)$$

$$\rho \dot{v}_z^{(n)}(t) = \frac{\sigma_{xz}^{(n)}(t) - \sigma_{xz}^{(n-\hat{x})}(t)}{\Delta x} + \frac{\sigma_{yz}^{(n)}(t) - \sigma_{yz}^{(n-\hat{y})}(t)}{\Delta y} + \frac{\sigma_{zz}^{(n+\hat{z})}(t) - \sigma_{zz}^{(n)}(t)}{\Delta z} + f_z(t)$$

$$\dot{\sigma}_{xx}^{(n)}(t) = (\lambda + 2\mu)\frac{v_x^{(n)}(t) - v_x^{(n-\hat{x})}(t)}{\Delta x} + \lambda\left(\frac{v_y^{(n)}(t) - v_y^{(n-\hat{y})}(t)}{\Delta y} + \frac{v_z^{(n)}(t) - v_z^{(n-\hat{z})}(t)}{\Delta z}\right)$$

$$\dot{\sigma}_{yy}^{(n)}(t) = (\lambda + 2\mu)\frac{v_y^{(n)}(t) - v_y^{(n-\hat{y})}(t)}{\Delta y} + \lambda\left(\frac{v_x^{(n)}(t) - v_x^{(n-\hat{x})}(t)}{\Delta x} + \frac{v_z^{(n)}(t) - v_z^{(n-\hat{z})}(t)}{\Delta z}\right)$$

$$\dot{\sigma}_{zz}^{(n)}(t) = (\lambda + 2\mu)\frac{v_z^{(n)}(t) - v_z^{(n-\hat{z})}(t)}{\Delta z} + \lambda\left(\frac{v_x^{(n)}(t) - v_x^{(n-\hat{x})}(t)}{\Delta x} + \frac{v_y^{(n)}(t) - v_y^{(n-\hat{y})}(t)}{\Delta y}\right)$$

$$\dot{\sigma}_{xy}^{(n)}(t) = \mu\left(\frac{v_x^{(n+\hat{y})} - v_x^{(n)}}{\Delta y} + \frac{v_y^{(n+\hat{x})} - v_y^{(n)}}{\Delta x}\right)$$

$$\dot{\sigma}_{xz}^{(n)}(t) = \mu\left(\frac{v_x^{(n+\hat{z})} - v_x^{(n)}}{\Delta z} + \frac{v_z^{(n+\hat{x})} - v_z^{(n)}}{\Delta x}\right)$$

$$\dot{\sigma}_{yz}^{(n)}(t) = \mu\left(\frac{v_y^{(n+\hat{z})} - v_y^{(n)}}{\Delta z} + \frac{v_z^{(n+\hat{y})} - v_z^{(n)}}{\Delta y}\right).$$

(4.5)

117

Given that $\hat{x}$, $\hat{y}$, and $\hat{z}$ are unit steps in the x, y, and z directions respectively and n denotes the current cell.

We have to apply stress free boundary conditions on our simulation boundaries, since our interest is in guided elastic waves in structures at MHz frequencies where the solid-air interfaces can be considered traction-free surfaces. This means that on the x boundaries σ_{xx}, σ_{xy}, and σ_{xz} all vanish while on y and z boundaries σ_{yy}, σ_{xy}, σ_{yz} and σ_{zz}, σ_{xz}, σ_{yz} are zero respectively. If we require the velocity components to be placed on the physical surface of our model, we find that the shear stress terms are also on the surface so we can set them to zero [51]. To ensure that the longitudinal stress at the surface vanishes, we set $\sigma_{ii}^{(surf)} = -\sigma_{ii}^{(surf+\hat{i})}$ for a lower boundary and $\sigma_{ii}^{(surf+\hat{i})} = -\sigma_{ii}^{(surf)}$ for an upper boundary [54]. This produces the equations for the surface velocity components for a lower boundary

$$\rho \dot{v}_i^{(surf)} = \frac{2\sigma_{ii}^{(surf+\hat{i})}}{\Delta s} + f_i \tag{4.6}$$

and for an upper boundary

$$\rho \dot{v}_i^{(surf)} = -\frac{2\sigma_{ii}^{(surf)}}{\Delta s} + f_i \tag{4.7}$$

for $i = x, y, z$.

The temporal discretization is based on a central difference operator, "leap-frogging" through time across the staggered grid,

$$v_i^{[k]} = v_i^{[k-1]} + \dot{v}_i^{[k-1/2]} \Delta t \tag{4.8}$$

$$\sigma_{ij}^{[k+1/2]} = \sigma_{ij}^{[k-1/2]} + \dot{\sigma}_{ij}^{[k]} \Delta t \tag{4.9}$$

where the superscript k denotes full and $k \pm 1/2$ denotes half-time steps of Δt with the total time given by $T = k\Delta t$. First the velocity components are updated, then we update the stress tensor components using the previously updated velocity components.

In order for the 3D-EFIT algorithm to be numerically stable, we must satisfy the Courant-Friedrichs-Levy-criterion:

$$\Delta t \leq \frac{1}{c_l \sqrt{1/(\Delta x)^2 + 1/(\Delta y)^2 + 1/(\Delta z)^2}} \tag{4.10}$$

where c_l is the fastest longitudinal wave speed in the elastic medium. For simplicity, we use equal lengths for the sides of the cells, Δs, so (4.10) becomes

$$\Delta t \leq \frac{1}{c_l \sqrt{3/(\Delta s)^2}}. \tag{4.11}$$

Here Δs is determined such that the shortest wavelengths present are adequately discretized using

$$\Delta s \leq \frac{1}{8} \lambda_{min} = \frac{1}{8} \frac{c_{min}}{f_{max}} \approx \frac{1}{10} \frac{c_{s,min}}{f_{max}}. \tag{4.12}$$

This assigns approximately 10 grid points per shear wavelength, adjusting the exact size to correspond to the desired space thickness.

In this work we are dealing with thin plate-like structures so our simulation space thickness is small compared to the length and width. In order to inspect materials for changes in thickness we have to use signals that have wavelengths on the same order as the thickness of our sample. This means that when dealing with a sample that is about 1 mm thick we have to be in the 1 MHz frequency range, resulting on the order of 10 grid points per millimeter. If we set out to

119

model one of the aircraft stringers from the previous chapter, we use the Δs for aluminum, 0.000145 m, and the sample is 3.5 cm tall, 5.8 cm wide and 1 m long. The simulation space is then 244 by 399 by 6875, or rather 669,322,500 grid points. Then when we consider that the simulation keeps track of ten separate components and material information for each of the cells, we need 53.54 GB of physical memory in order to run the simulation. Most desktop PC computers have 2-4 GB of physical memory, so instead we have developed the simulations to run on a large computer cluster in parallel.

4.2 Parallel Processing

Parallel implementation of the three dimensional EFIT code is necessary for modeling large real world structures. The College of William and Mary possesses a high performance cluster, the SciClone. At this time SciClone consists of 271 nodes with a total of 623 processing cores, 1.1 TB of physical memory and 34.1 TB of disk capacity. At peak performance the cluster has measured 2.3 TFLOP/S floating point operations. By assigning multiple processors separate parts of a calculation the final results are obtained faster. In some instances parallel processors are used to analyze large amounts of data, but here we are using them to create and track large amounts of data. In this implementation, rather than splitting up the task of doing calculations we split the actual simulation space therefore reducing the number of cells to a manageable size for the physical memory on each processor. In this fashion, we can accommodate the entire model across the cluster.

We split our EFIT simulation space across multiple processors using a typical

two-dimensional domain decomposition [54]. This domain decomposition consists of taking the three dimensional Cartesian simulation space and slicing it in the xz plane, then again in the yz plane. This results in having the entire thickness of the simulation intact on each processor, allowing the algorithm to loop through the thickness without having to account for an edge of the processor in this direction. In the x and y dimensions, however, we do need to pay attention to the processor boundaries. For each half time step, the cells on the processor edges need information from their neighbors in order to update themselves according to (4.5). Each processor updates the velocity components then sends the edge velocity components to its neighbors before updating the stress components, then it sends the edge stress components before increasing the time step.

From the equations it is apparent that not all the neighbors need all of the velocity and stress values from the adjacent processors. We end up with 7 different computation cells (Figure 4.2) for the 9 components since the normal stress components all use the same computation cell. Since the components only need the value of any given component from one direction we can use a one way communication scheme for each half time step. After updating the velocity components, each processor passes the v_x edge values to the processor in the $-y$ direction (front) and in the $+x$ direction (right), the v_y in the $-x$ direction (left) and $+y$ direction (back), and the v_z to the front and left in order to update the stress components. The stress values on the processor edges are then passed in a similar fashion: the σ_{xx} to the left, the σ_{yy} to the front, the σ_{xy} to the back and right, the σ_{xz} to the right, and the σ_{yz} to the back. In this fashion the the entire domain becomes a seamless simulation space.

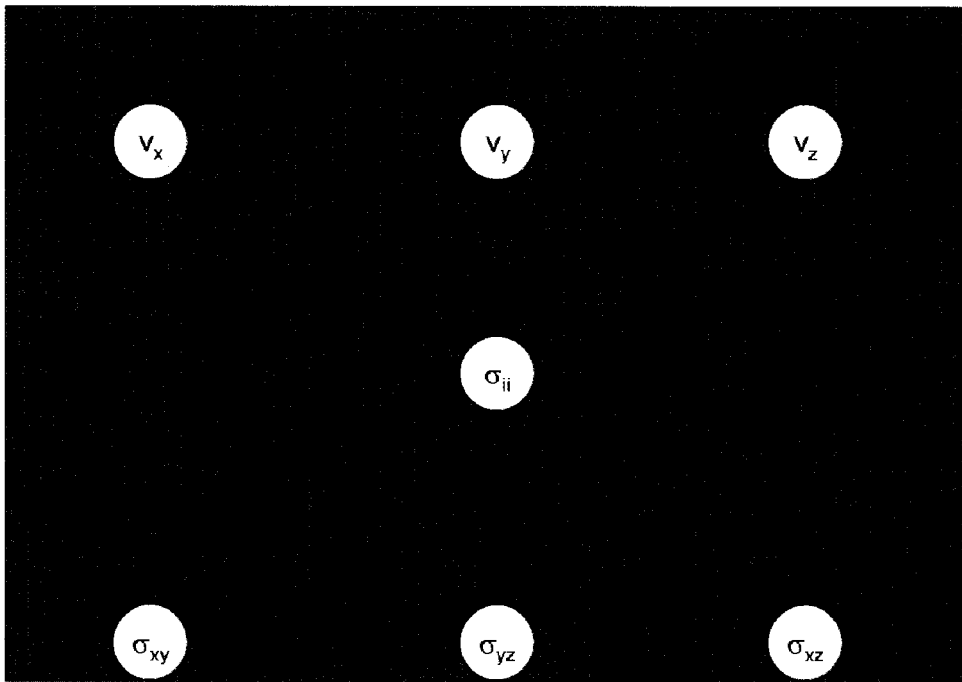With the parallel implementation of the EFIT code there are several issues

121

Figure 4.2: Each of the EFIT components requires different information to update each half time step. This creates 7 computation cells with one way communication.

that need attention. First of all, since each processor has a different part of the simulation space, it has to update a different part of the model. For instance, in a model of a flat plate with a milled rectangular section, only a few of the processors will actually deal with the flaw, and the edges of the plate. In order to accommodate these features we wrote a function that updates the interior of a rectangular volume, applying only specified boundary conditions on the edges. This is straight forward for the edges of the simulation space; if a processor is on the edge of the domain, then it applies that boundary condition. However, when dealing with a flaw in the interior of the space we have to be more careful. When a flaw is present in a simulation there are 17 possibilities for the orientation of the flaw on each processor. The trick we use to sensibly keep track of the possibilities is that when we map the flaw onto the CPU we keep track of whether or not an edge of the flaw is present. To make it more complicated, the upper and lower boundaries are treated differently so we assign the numbers: 1 for a lower y boundary, 2 for an upper y boundary, 10 for a lower x boundary, 20 for an upper x boundary, 0 for no flaw and 4 for the flaw covering the entire processor. After mapping the edges of the flaw to a particular processor, we add the values so that we know which configuration to apply, Figure 4.3 shows the 17 possible configurations with their respective flaw values.

For each case, we split the individual processor simulation model into rectangular regions and apply the needed boundary conditions. For instance, for flaw value 2, we have 3 regions that are updated (Figure 4.4). If the processor is positioned on the upper y edge of the domain, we apply the upper and lower z boundaries on region A, under the flaw, the lower z and upper y boundaries on region B and finally the upper and lower y and upper z boundaries on region C.
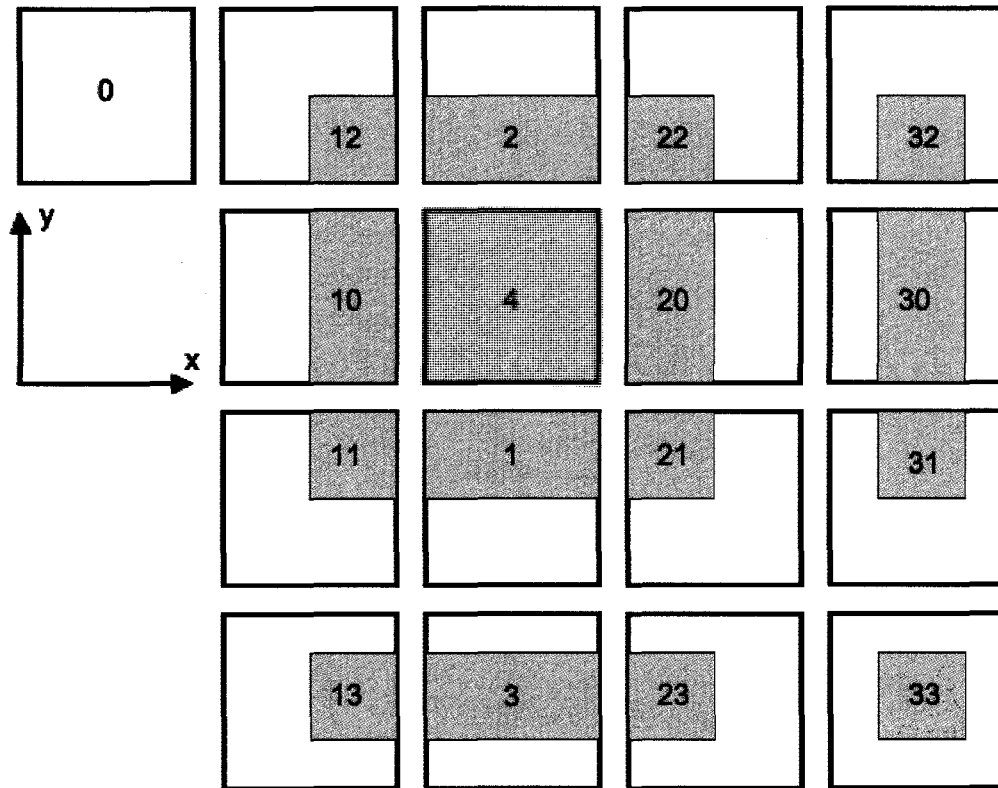
Figure 4.3: Seventeen possible orientations of a rectangular flaw positioned on individual processors.
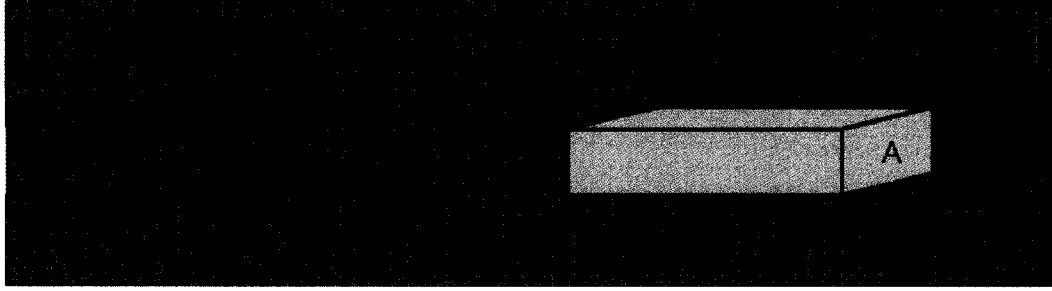
Figure 4.4: For flaw value 2 we split the model on the processor into three regions to apply the appropriate boundary conditions for the individual regions to obtain the overall model.

This creates a seamless model across the multiple processors without having to hard code the geometry beforehand, instead we can simply use input files with the dimensions of the simulation space, model and flaw.

Before simulating more complicated structures, we first benchmark our EFIT simulation method by comparing it to experiment with simple plates. For this we use aluminum plates that are 30.5 cm square and 3.171 mm thick [16]. For comparison, we consider both a flaw free plate and plates with a rectangular thinning. Figure 4.5 shows the layout of the test pieces. In the flawless sample, the rectangular region has the full thickness of the plate whereas the region in sample F1 is 2.768 mm thick and 1.97 mm in sample F2. In both the experiment and in simulation we place 1" wide, longitudinal contact transducers 5 cm from the sides of the plate. The longitudinal transducers vibrate in the z-direction in order to excite the guided elastic waves which propagate omni-directionally. Our experimental apparatus uses a 2 cycle tone burst of a 500 kHz sine wave. We simulate this drive function by creating a 2 cycle windowed sine wave function of time, $f_z(t)$ and add it as the source term f_z in (4.5). For the simulation we split the simulation space across 56 processors, in an 8 by 7 topology.

125
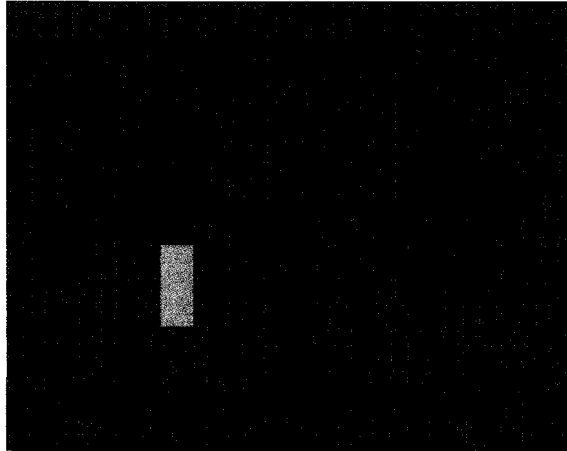
Figure 4.5: This is a schematic of the test samples used to calibrate the EFIT simulation method. The aluminum plate is 30.5 cm square and 3.171 mm thick, with the flawed samples having rectangular thinning with thickness of 2.768 mm for sample F1 and 1.97 mm for sample F2. A longitudinal transmitting transducer is placed on the red (left) dot while a passive receiver transducer is placed on the right (green) dot.

Below are snapshots of the simulated Lamb wave propagation in the clean plate (Figure 4.6). The red and white ovals in the first two frames indicate the position of the S0 and A0 modes respectively. Notice as they propagate they separate from each other because of their different velocities. We then collected A-line waveforms from both the simulated model and the experimental plate (Figure 4.8). The transducer in the experimental and the computer in the simulation record the movement of the plate in z-direction to obtain the waveforms. From the aluminum dispersion curves (Figure 4.7) we expect to see only the presence of two propagating guided wave modes, the S0 and the A0 because the higher order modes are cut off. Traveling through the thinned region should speed up the S0 mode while at the same time slowing down the A0 mode. However, due to the size of the flaw the arrival time shifts are fairly minimal. Figure 4.8 shows the raw waveforms collected from experiment (blue) and EFIT (red) with the expected

Figure 4.6: Snapshots of the simulated propagation of the elastic waves through a clean 3.171 mm thick clean plate.

127
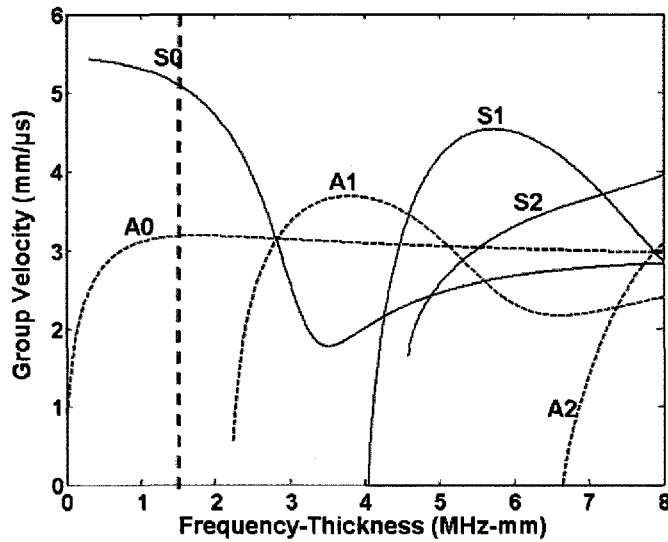
Figure 4.7: Aluminum dispersion curve. For a frequency-thickness product of 1.5 mm-MHz (dotted line) we expect the arrival of 2 guided wave modes, S0 and A0.

S0 and A0 arrival times indicated by the vertical red and blue lines. As with our NDE applications we need to employ the DWFT in order to extract the mode arrival times from the waveforms. Figure 4.9 shows the resulting thumbprints and automatically extracted arrival times for the comparison. From these thumbprints we see that we can determine the arrival times of the first two modes automatically. We do see the effects of the faster S0 mode in the data as well as the slowing of the A0 mode. The shifts are slghtly off from what we would expect strictly from the dispersion curves, but this is a real sample and if we look at snapshots (Figure 4.10) of the EFIT simulation for the flawed samples we see that there are scattering effects that should also be taken into account for the mode arrival times. As we look at the snapshots from the flawed sample propagation we can see the internal reflections from the sides of the flaw as well as some scattering from the edges of the milled rectangular thinning. The similarities between the raw waveforms

128
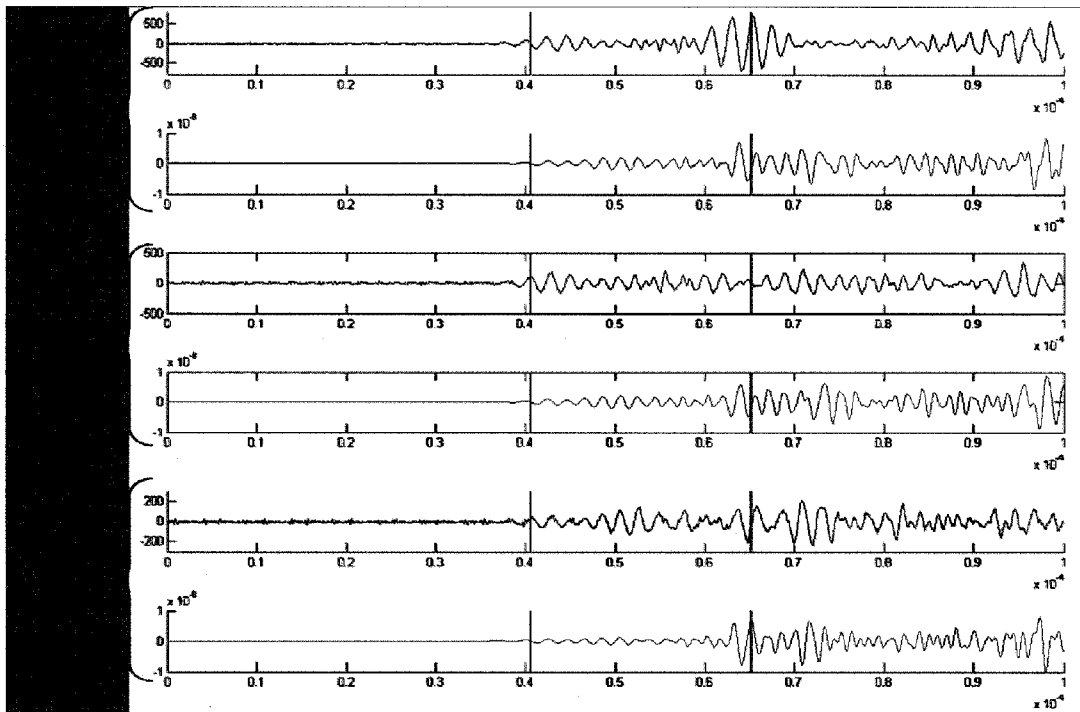
Figure 4.8: Comparison of EFIT generated waveforms (red) with their experimental (blue) counterparts from an aluminum plate with increasing rectangular flaw milled in it. The red and blue vertical lines indicate the expected arrival times for the S0 and A0 modes respectively.
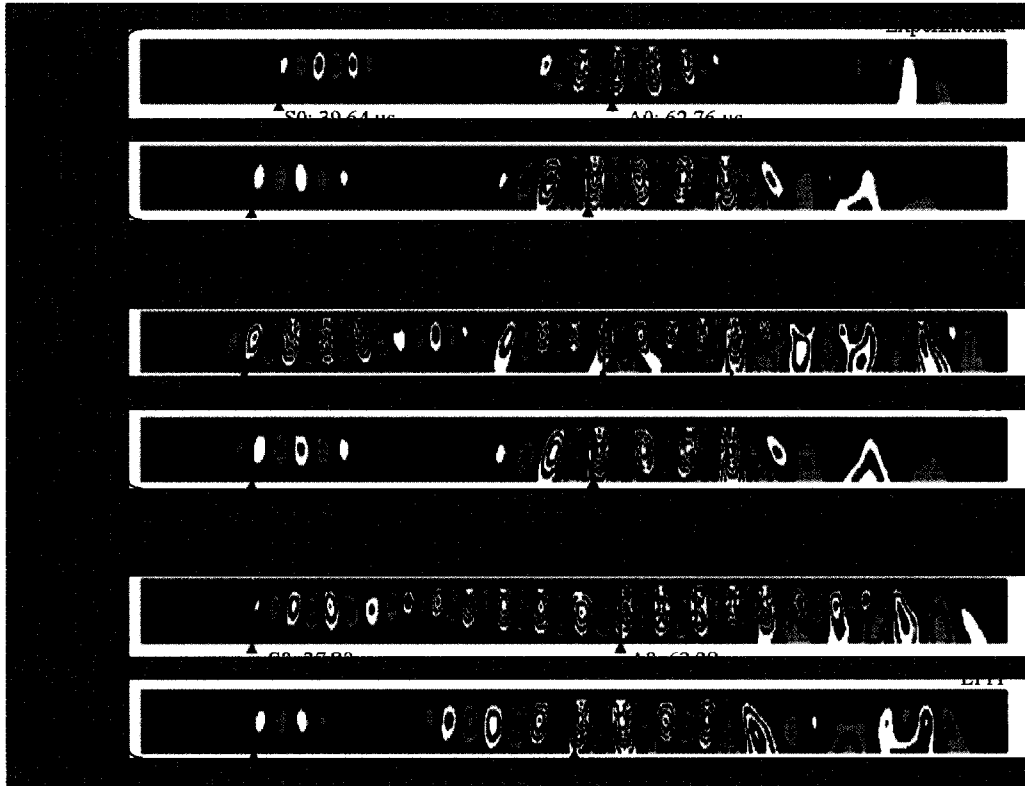
Figure 4.9: Thumbprints generated from the waveforms in 4.8. The automatically extracted mode arrival times are listed below each thumbprint.
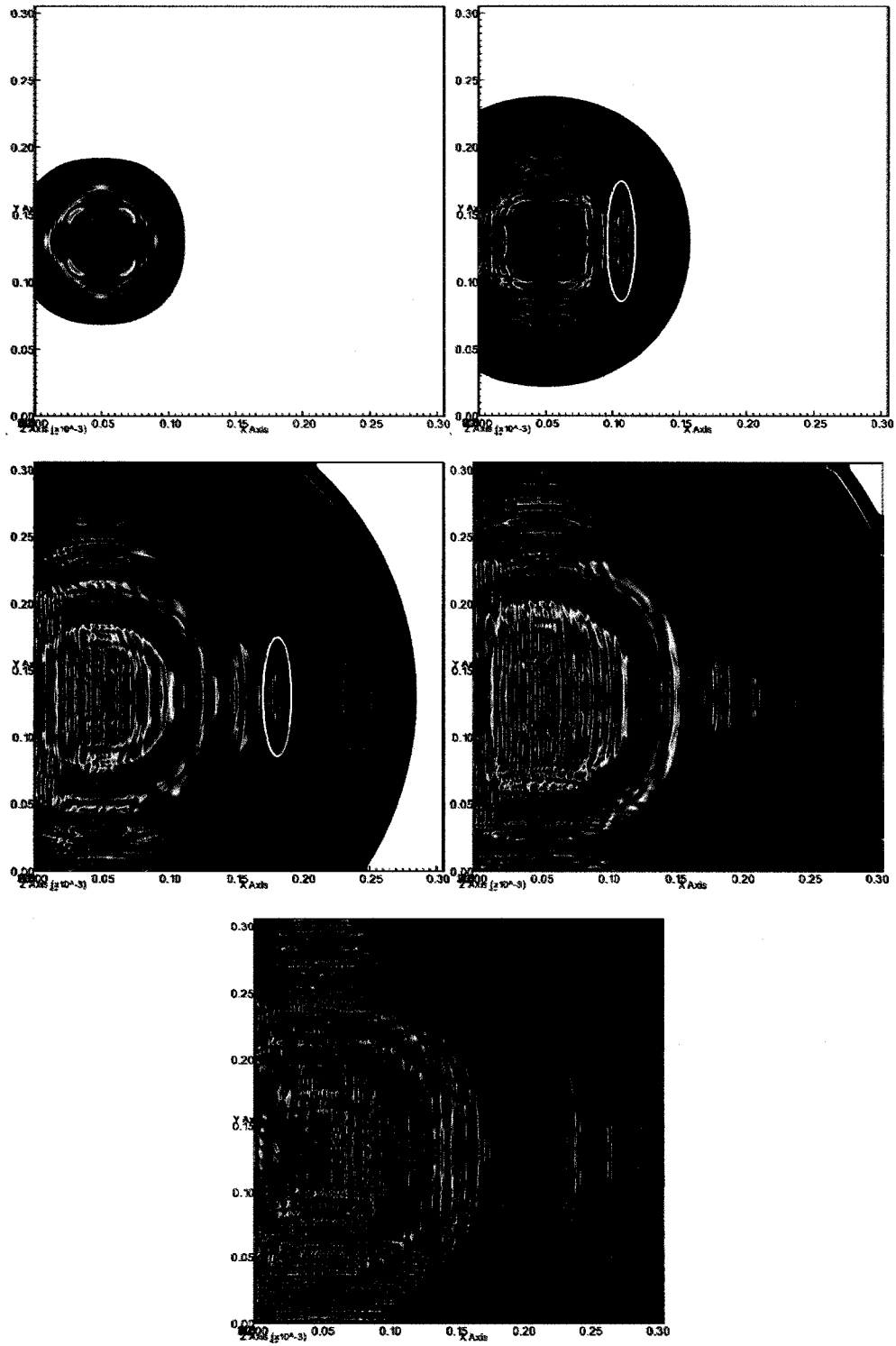
130
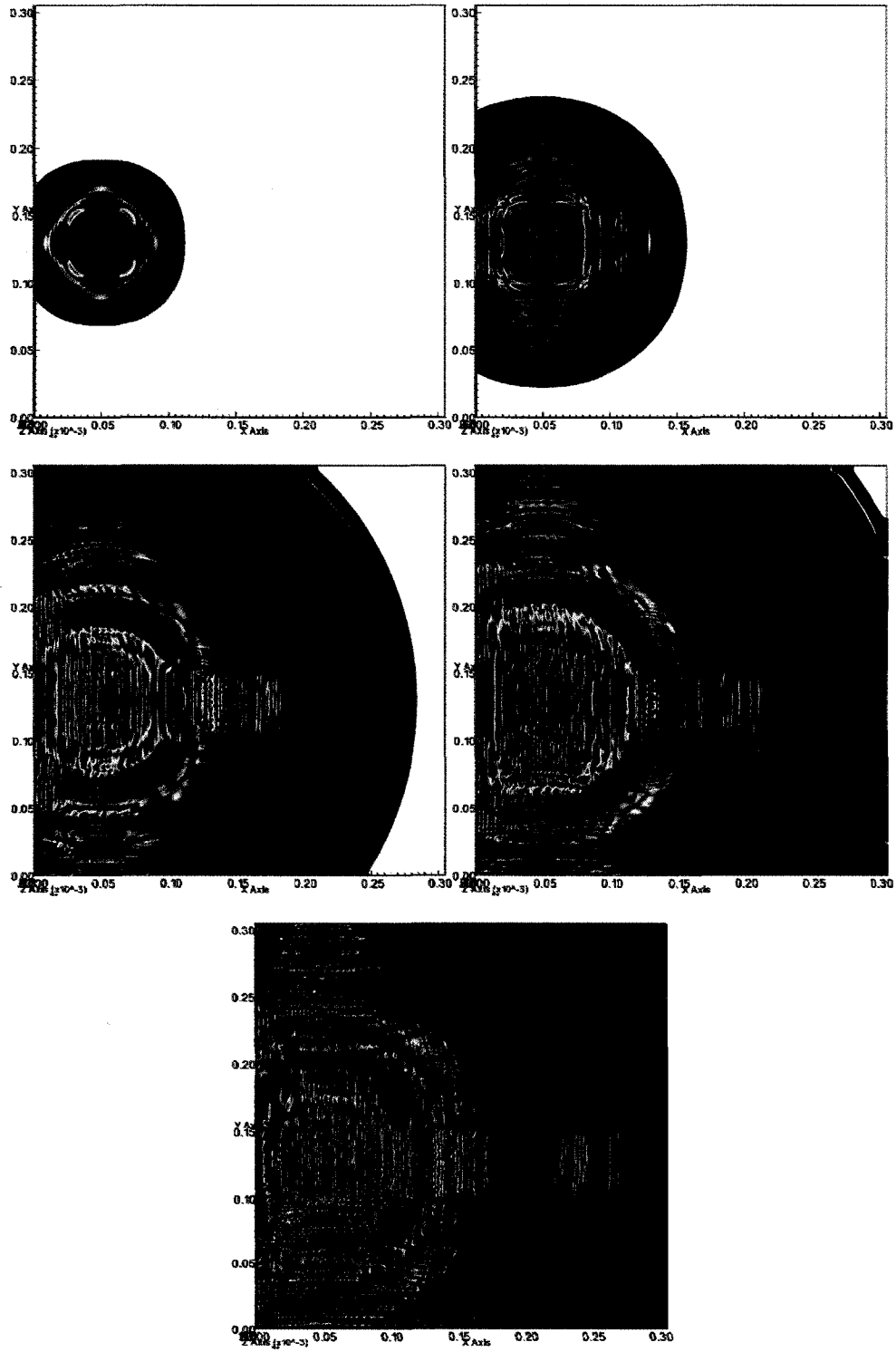
Figure 4.10: Snapshots of the simulated propagation of the elastic waves through a clean 3.171 mm thick clean plate.
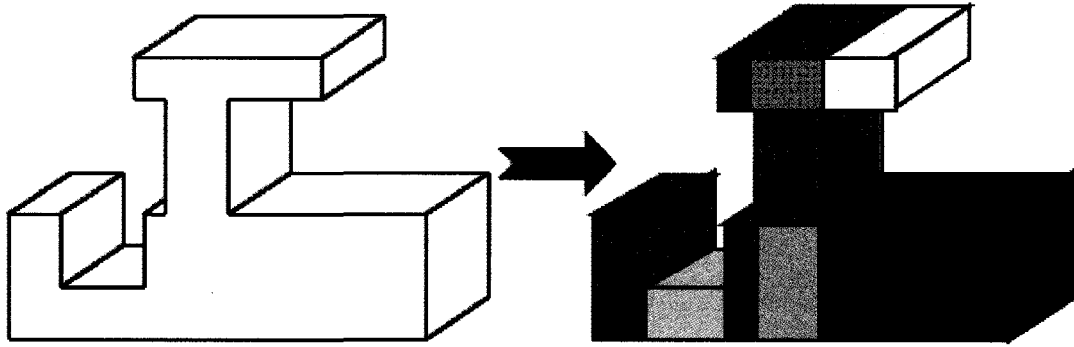
Figure 4.11: Example of breaking down a 3D shape using the rectangular regions in order to apply the necessary boundary conditions.

from experiment and simulation, as well as the fact that we can extract the arrival times consistently using both techniques, leads us to believe that we are correctly simulating the elastic guided waves with our implementation of EFIT.

4.3 Three Dimensional Structures

It is reasonably straightforward to simulate flat plates and other rectangular shapes, but the real challenge is to examine more complex 3D shapes. In order to incorporate built up structures into the simulations, we build the model piece by piece, keeping track of the boundaries conditions on each piece similar to our treatment of the regions with the flawed plate. For example, if we were to build a shape like the one found in Figure 4.11, it would require 11 different regions. But not all of these regions are on one processor so we again use our mapping to figure out what part of the structure we have on each processor. Once we know the extent of the model, the EFIT code marches through the simulation without trouble. See Figure 4.12 for a snapshot of elastic waves propagating through the shape found in Figure 4.11.
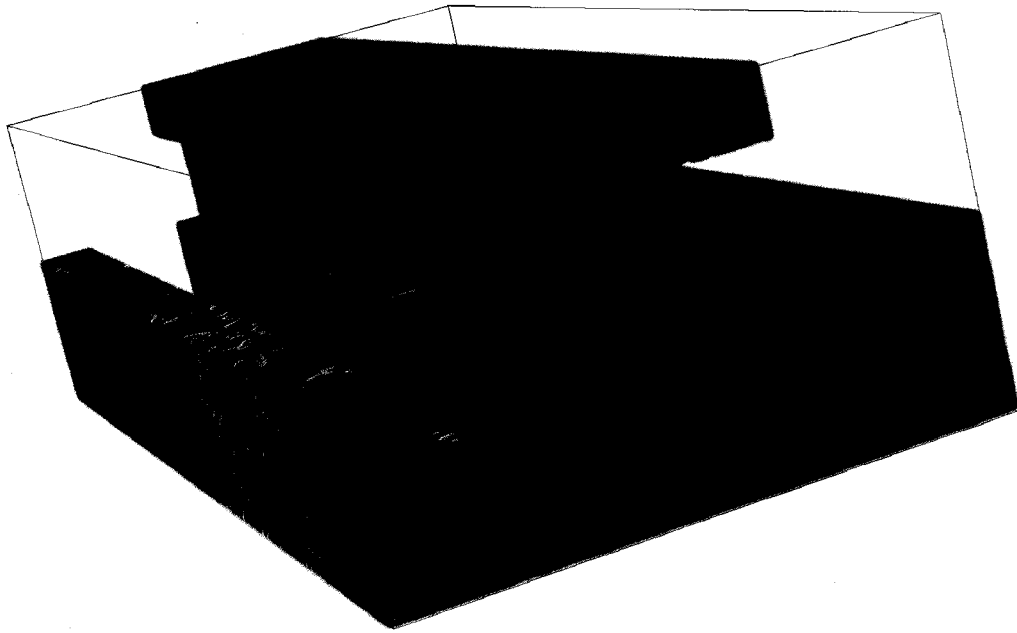
Figure 4.12: Example of elastic waves propagating through 3D shape.

Looking at (4.5), we see that the only material parameters that are present are the density, ρ, and the Lamé constants, λ and μ. For solid elastic materials, the interface with air is well approximated by a solid-vacuum interface so we can set the density of cells not in our test material to zero (or a large negative number in practice for convenience). In this fashion we can also include multiple materials, however we have to take care to ensure continuity of stress and velocity across cell surfaces. If we choose the material parameter cell to coincide with the σ_{ii} integration cell, we can average the the material parameters ρ and μ for use in

(4.5) [52].

$$\rho^{(n,x)} = \frac{\rho^{(n)} + \rho^{(n+\hat{i})}}{2}$$

$$\rho^{(n,y)} = \frac{\rho^{(n)} + \rho^{(n+\hat{j})}}{2}$$

$$\rho^{(n,z)} = \frac{\rho^{(n)} + \rho^{(n+\hat{k})}}{2}$$

$$\mu^{(n,xy)} = \frac{4}{\frac{1}{\mu^{(n)}} + \frac{1}{\mu^{(n+\hat{i})}} + \frac{1}{\mu^{(n+\hat{j})}} + \frac{1}{\mu^{(n+\hat{i}+\hat{j})}}}$$

$$\mu^{(n,xz)} = \frac{4}{\frac{1}{\mu^{(n)}} + \frac{1}{\mu^{(n+\hat{i})}} + \frac{1}{\mu^{(n+\hat{k})}} + \frac{1}{\mu^{(n+\hat{i}+\hat{k})}}}$$

$$\mu^{(n,yz)} = \frac{4}{\frac{1}{\mu^{(n)}} + \frac{1}{\mu^{(n+\hat{j})}} + \frac{1}{\mu^{(n+\hat{k})}} + \frac{1}{\mu^{(n+\hat{j}+\hat{k})}}}$$

(4.13)

For layered materials we still update the model by rectangular volumes, but if two regions next to each other have different densities we change the material parameters at the interface. The influence of the different material properties at the interface is clearly seen when looking a bulk waves in a cube. Figure 4.13 is a simple cube of steel 5 cm x 5 cm x 3 cm, a longitudinal transducer was pulsed for half a cycle of a 1 MHz sine wave in order to excite a bulk wave response in the cube. Clearly seen is the fast longitudinal (L) wave in the first frame. When this wave hits the bottom surface we get a reflected L and shear (S) wave as seen is the second frame. In contrast when we add another material layer to this simulation space we see many more features. Figure 4.14 shows snapshots of elastic bulk wave interactions with a block of steel with a 1 mm thick plating of gold on top. We see that the L waves travel much faster in the steel than the gold layer. Gold ($\rho = 19.7g/cm^3$) is much denser than steel ($\rho = 7.9g/cm^3$), but much softer so the waves are slower. When the original L wave hits the interface at $z = 2$ mm, it transmits both L and S waves into the steel substrate as well as reflecting L and S back towards the surface. This repeats for each of the new

134
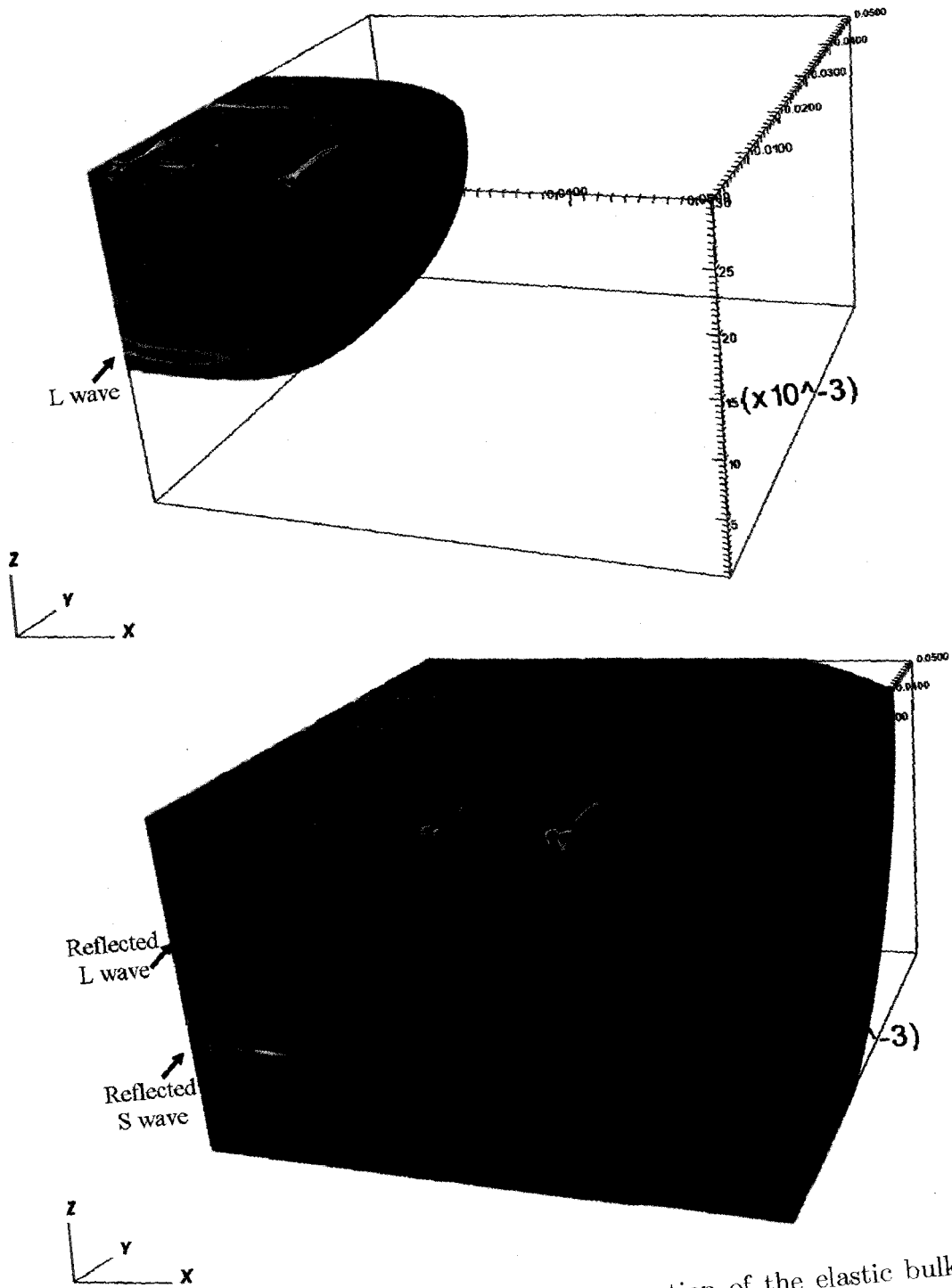
Figure 4.13: Snapshots of the simulated propagation of the elastic bulk waves through a block of steel.
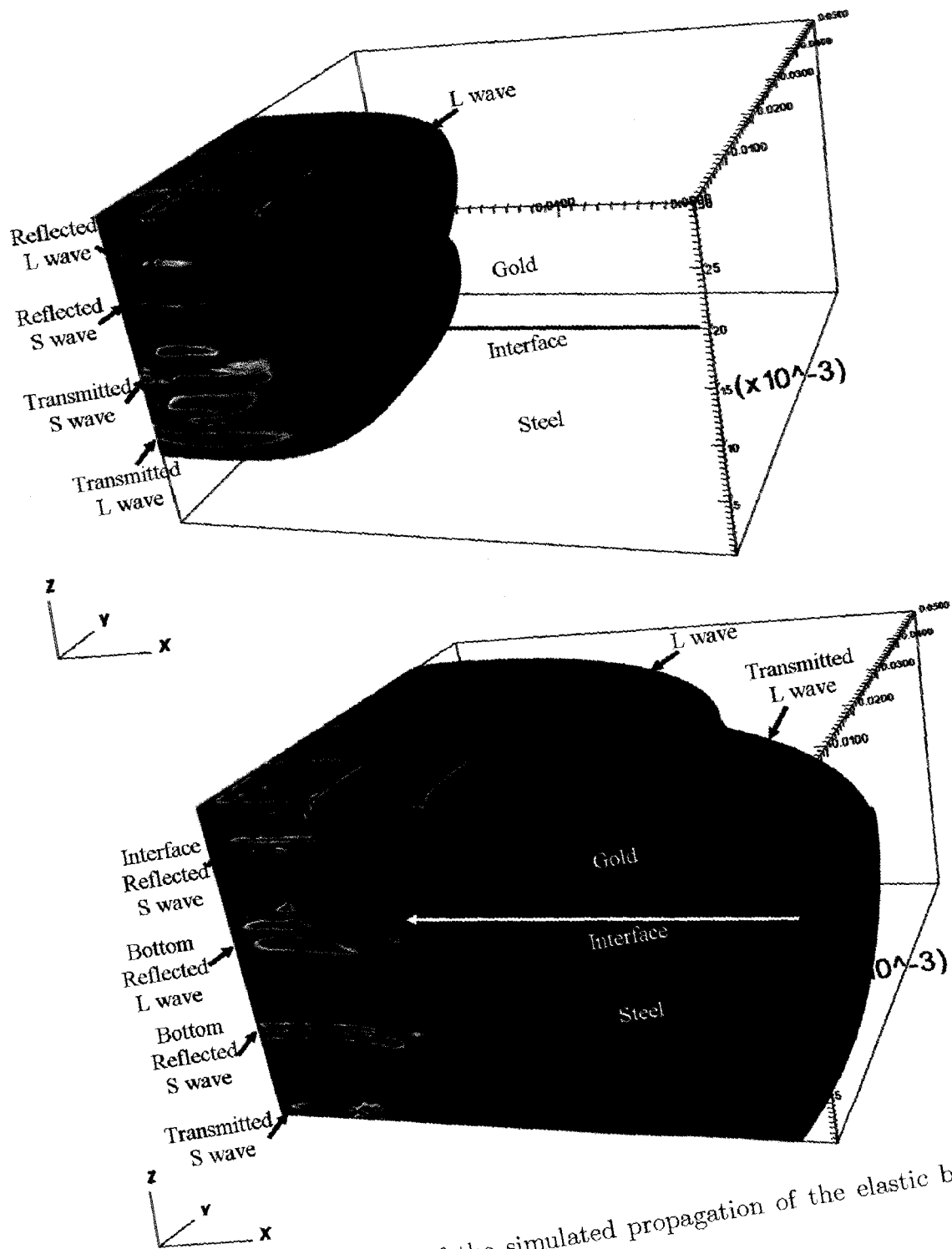
Figure 4.14: Snapshots of the simulated propagation of the elastic bulk waves through a block of steel with gold plating.

waves hitting an interface, either the outside of the cube or in between the layers. It is interesting to notice in Figure 4.14a that we can see the transmitted shear wave in the steel ($v_S = 3220m/s$) has close to the same velocity as the L wave in gold ($v_L = 3340m/s$). If there is a delamination between the gold and steel layers, the waves respond accordingly. Figure 4.15 shows how the bulk waves are affected if there is a delamination between the steel substrate and the gold plating. This model contains a delamination from $x = 5$ mm to $x = 4$ cm across all y values. The delamination is achieved through applying boundary conditions as though there is a small pocket of air between the two layers.

Another flexibility of our EFIT code is that we can either apply boundary conditions to an entire flaw region or keep track of the density and Lamé material parameters cell by cell and step through the space applying the needed boundary conditions. This allows us to insert surfaces into our models. One of the main difficulties of adding a surface to the model is keeping in mind the stability criterion so that the EFIT model still behaves properly with the rough surface. This is achieved either by smoothing the surface somewhat or by reducing the cell size in the model. Figure 4.16 shows a close up view of elastic waves propagating through as small plate of aluminum with an uneven surface mapped onto a section. It can be seen here that the uneven surface distorts the shape of the guided waves scattering from the obtrusions on the surface.
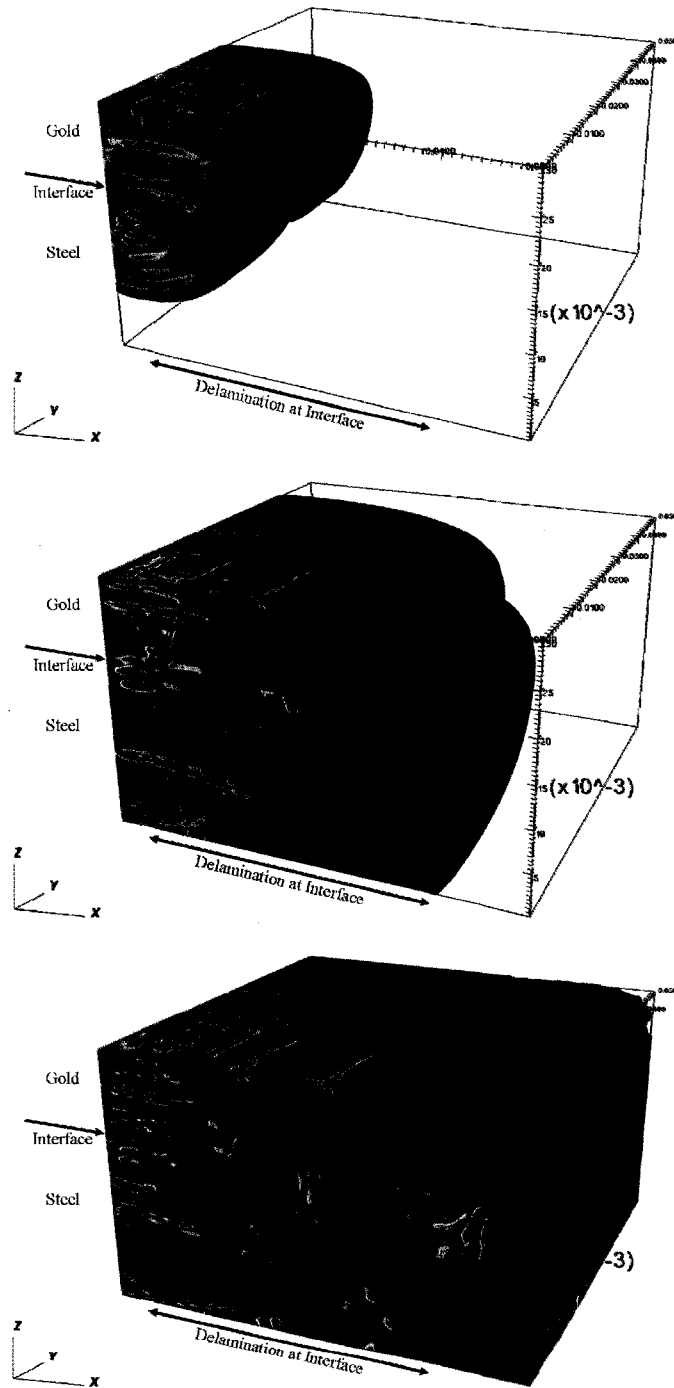
Figure 4.15: Snapshots of the simulated propagation of the elastic bulk waves through a block of steel plated with gold with a delamination.
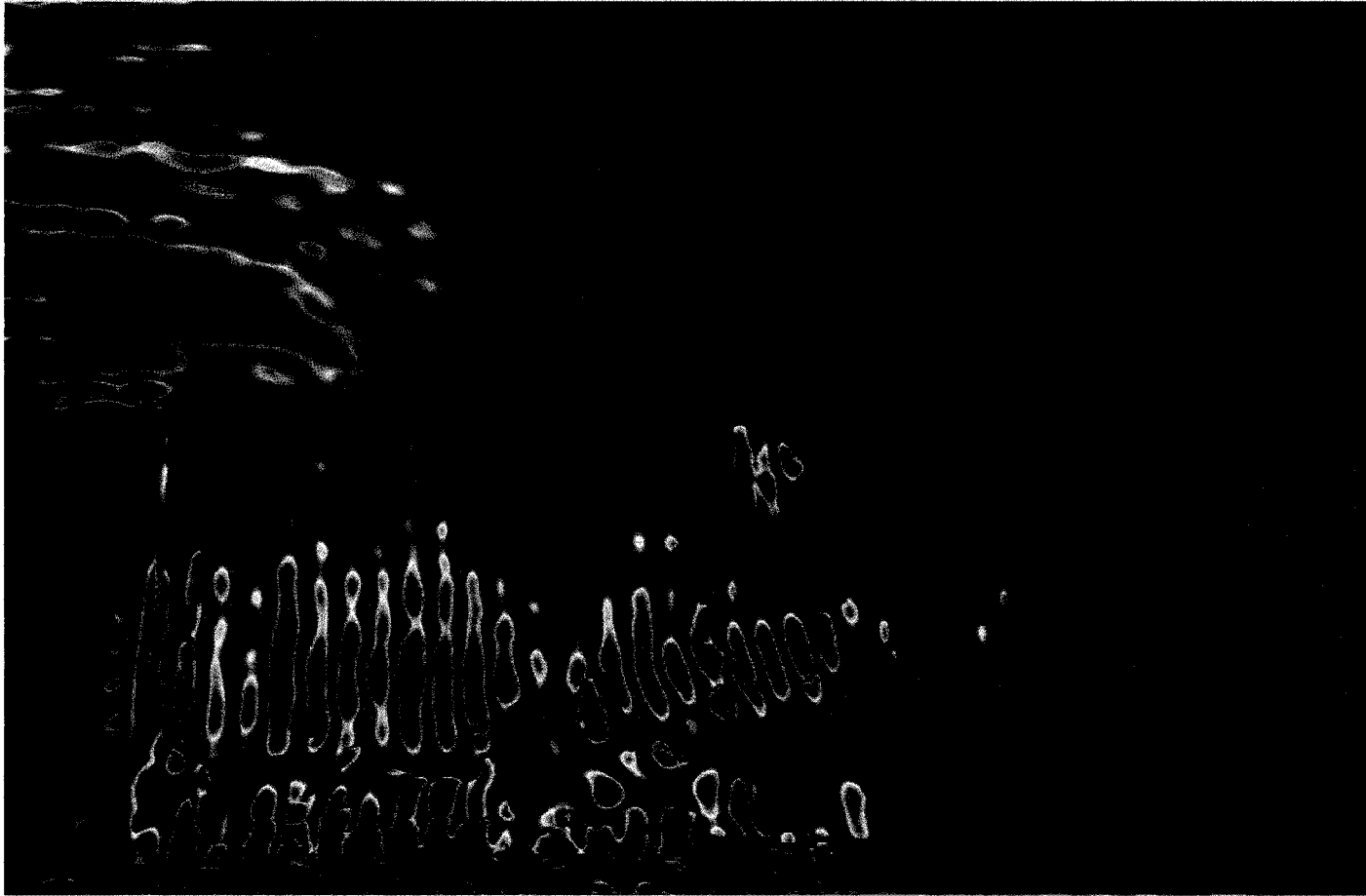
Figure 4.16: Elastic waves still propagate with uneven surfaces, although the guided wave mode change shape due to the scattering from topographic features.

This is the final piece in the development of our 3D EFIT package that we need to simulate guided elastic wave propagation in real structures.

4.4 Results

This 3D-EFIT simulation method can be used to better understand our NDE applications. Showing that we can accurately model the physics of the elastic waves in these different geometries is critical for having a robust analytical tool.

4.4.1 Aircraft Stringers

The aircraft stringer problem lends itself well to EFIT simulations. The geometry of the "T" stringers is easily built up in the simulation space, and the problem is interesting because the structure is complicated. Until now we have been assuming that the bottom flange of the stringer acts like a simple plate with the guided waves propagating in the usual fashion. We have done a series of simulations to study how reliable this approximation is.

First we look at how the guided waves propagate down a plate which has dimensions identical to the flange of the experimental "T" stringer. The simulation space is 1m x 5.8 cm x 1.6 mm, split across 62 processors for a simulation time of 400 μs. The ultrasonic excitation is modeled after the procedure used in Section 3.3 for the experimental approach. We use a 5-cycle sine wave, with shear vertical (SV) excitation of a 1 MHz, .5" square contact transducer for the $f_x(t)$ source term in equation (4.5), placed 10 cm from $x = 0$ and 1 cm from $y = 0$ on the surface of the simulated plate.

In Figure 4.17, we can see that the S0 and A0 modes separate out as they

Figure 4.17: Propagation of the Lamb waves as modeled by the 3D EFIT simulation. 1 MHz transducers were placed 10 cm from each end. For each of the frames the S0 and A0 modes are indicated by a red and blue triangle respectively. Reflected modes from the ends of the sample are also seen present.

propagate down the length of the flange. We even see the reflections off the end of the test piece that is nearer the transmitting transducer. What is interesting is that if we now include the web of the "T" stringer we can still see the propagation of the expected guided waves (Figure 4.18). Due to the size of the full "T" stringer model we had to cut down on the amount of data stored from the simulation. Figure 4.18 shows the magnitude of the displacement of each of the computation cells instead of the displacement itself. The guided wave modes are still decipherable as indicated by the red and green arrows. For a close up look at the modes as they propagate the length of the "T" stringer and spread out, see Figures 4.19-4.23.   One of the interesting features from this simulation is that the web of the stringer seems to damp out the S0 mode so that by the time it propagates the length of the stringer (Figure 4.22), it is barely visible. This is consistent with the findings from our experimental tests where we were expecting to see a change in the S0 arrival times as well as the A0, but we had difficulty extracting the arrival information for the S0 mode.

If we take a closer look at the waveforms from the two simulations and compare them to our experimental results from the original stringer (Figure 4.24) we see many similarities. First of all we don't immediately see the presence of the S0 mode in either the full "T" simulation or the experimental waveform, but this is now expected because of the damping from the web of the "T". Secondly, there seems to be a similar feature in all three waveforms that arrives near the expected arrival time of the A0 mode. Our next step is to apply the same DWFT algorithm to these new simulation results to see if we can extract similar features from the simulation data as we could for the experimental data. Since the simulation wave amplitudes are so much lower than the experimental, we reduced the number of
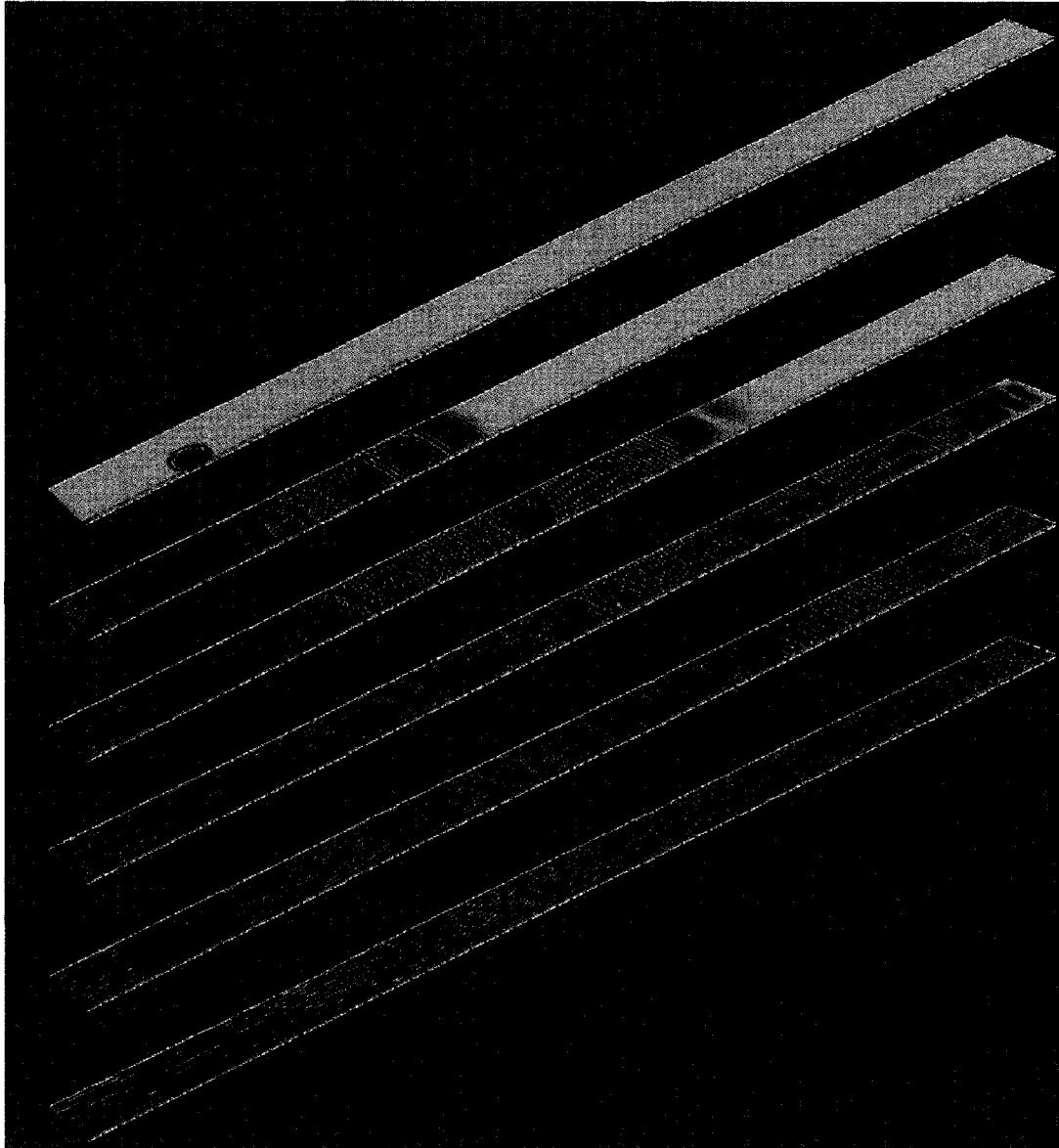
142
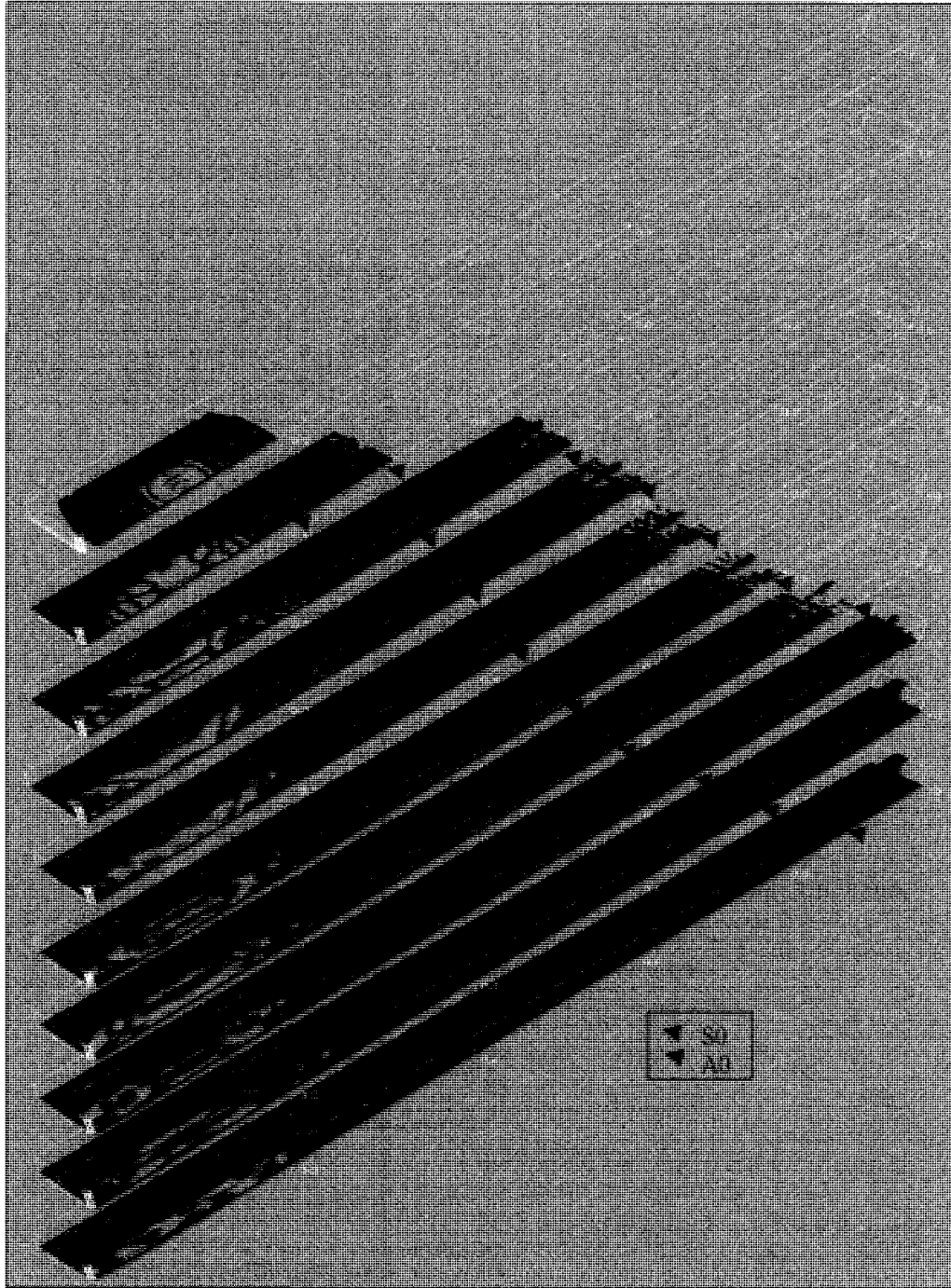
Figure 4.18: Propagation of the Lamb waves as modeled by the 3D EFIT simulation. 1 MHz transducers were placed 10 cm from each end. For each of the frames the S0 and A0 modes are indicated by a red and green triangle respectively.

143
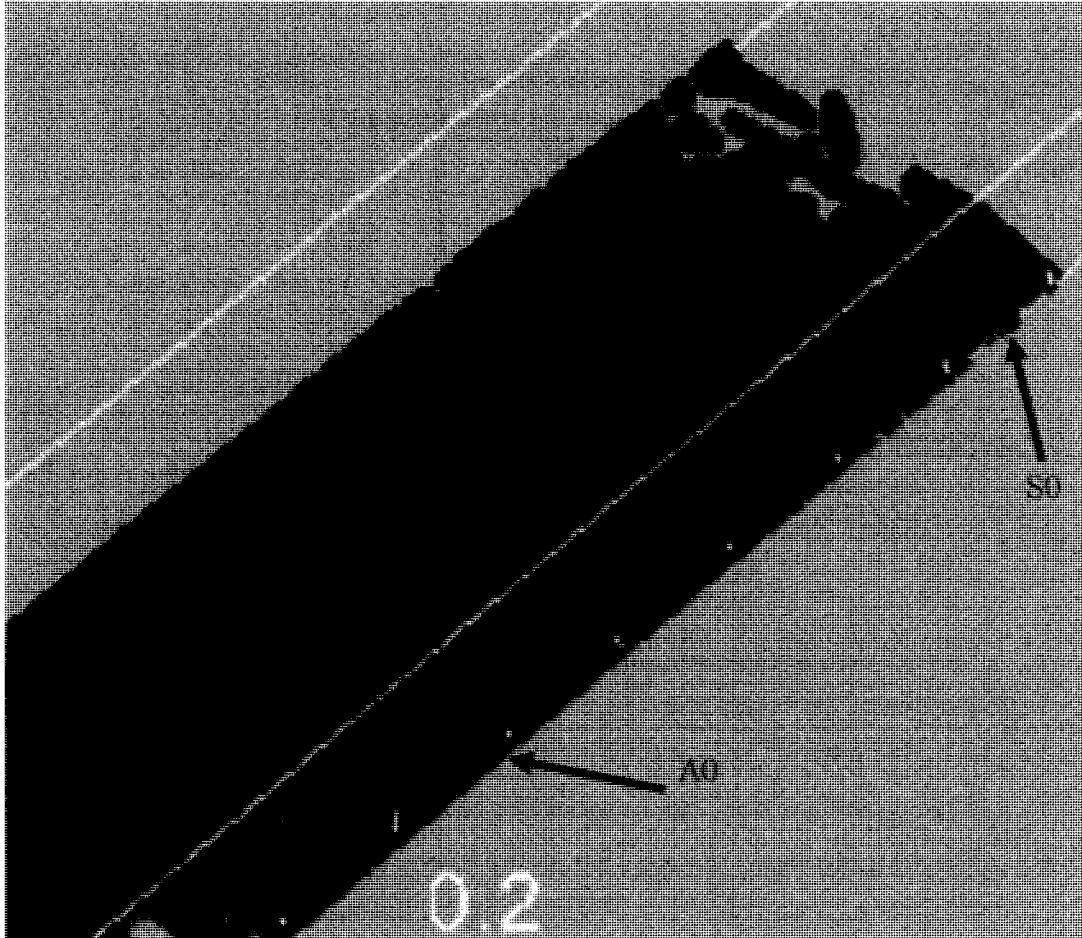
Figure 4.19: Zoom of "T Stringer mode propagation 1.
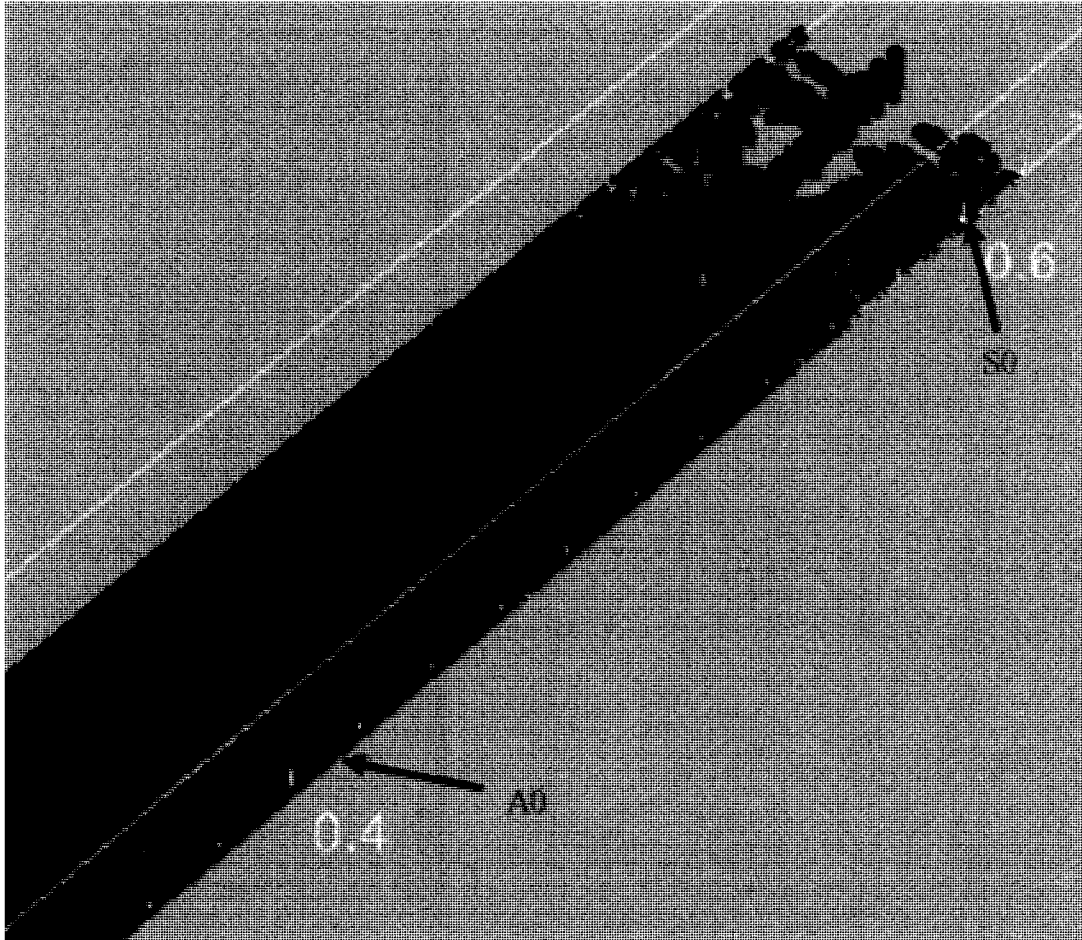
Figure 4.20: Zoom of "T Stringer mode propagation 2.
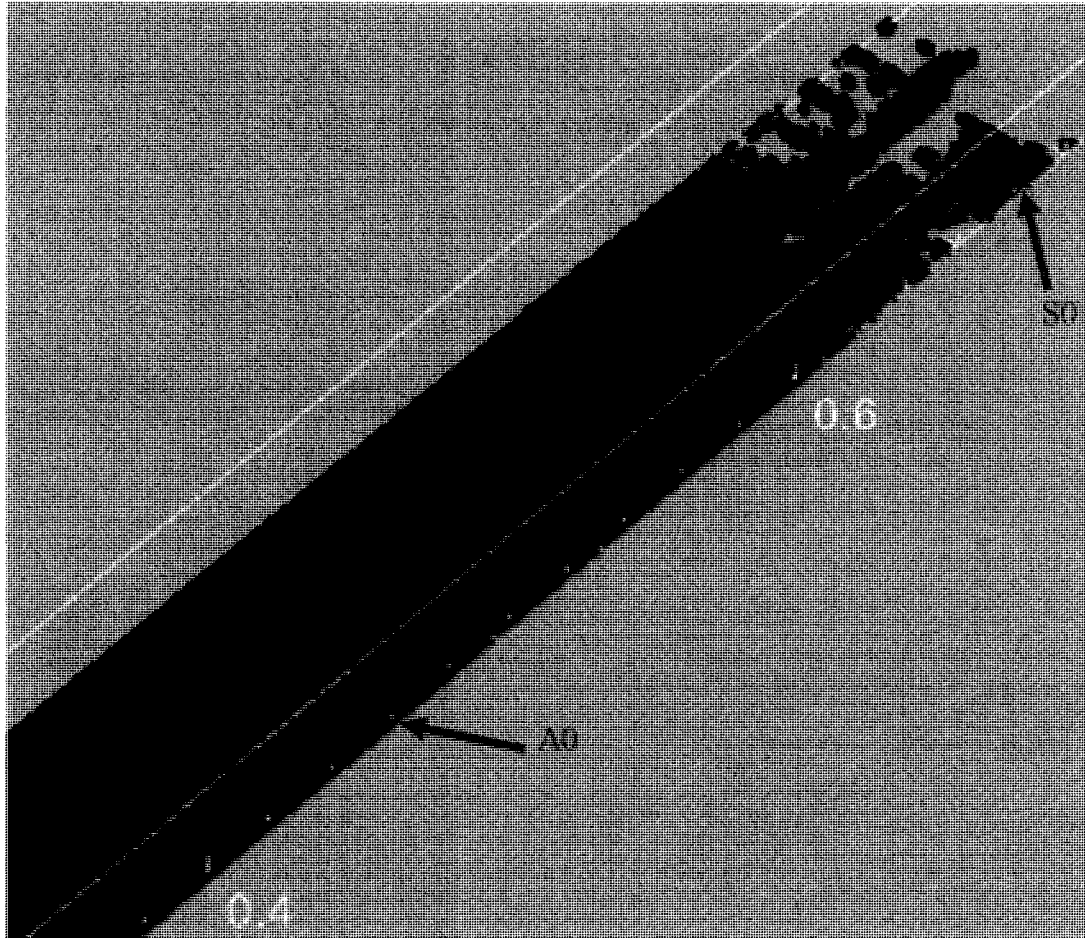
Figure 4.21: Zoom of "T Stringer mode propagation 3.
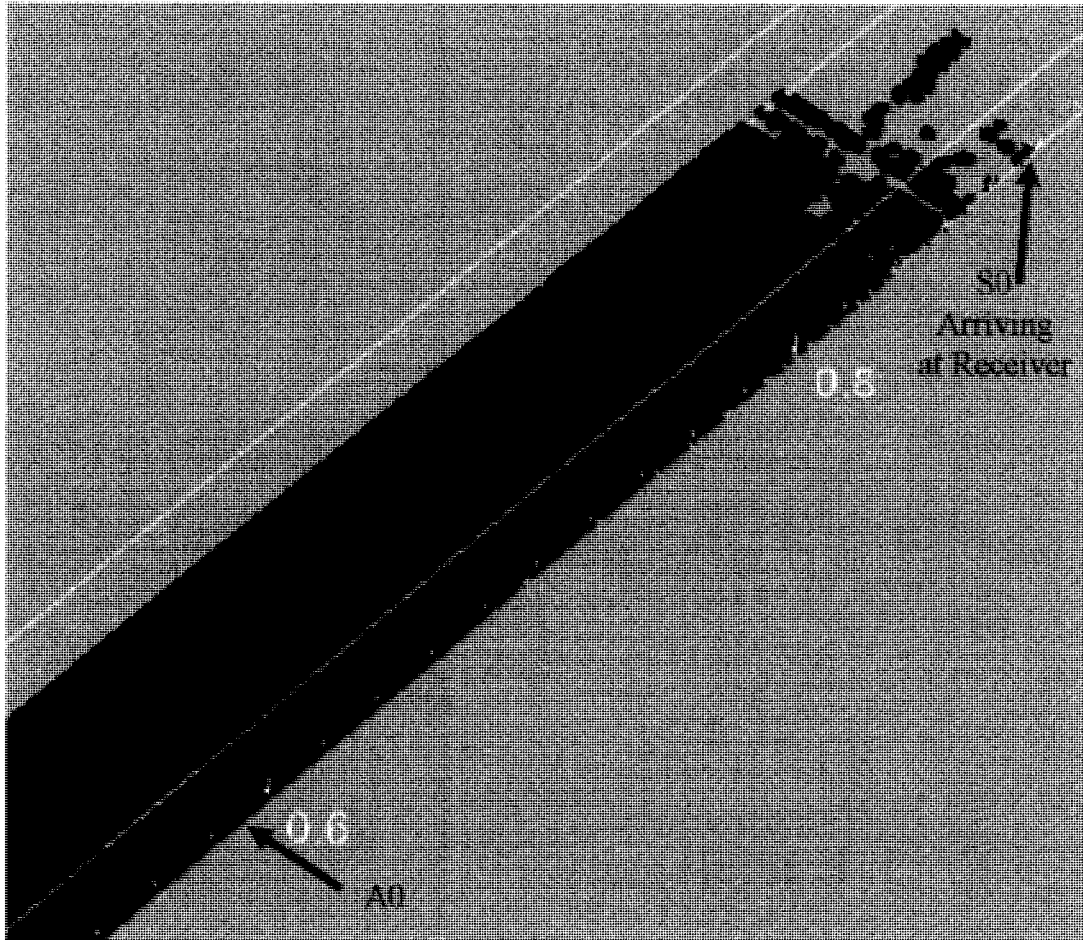
Figure 4.22: Zoom of "T Stringer mode propagation 4.
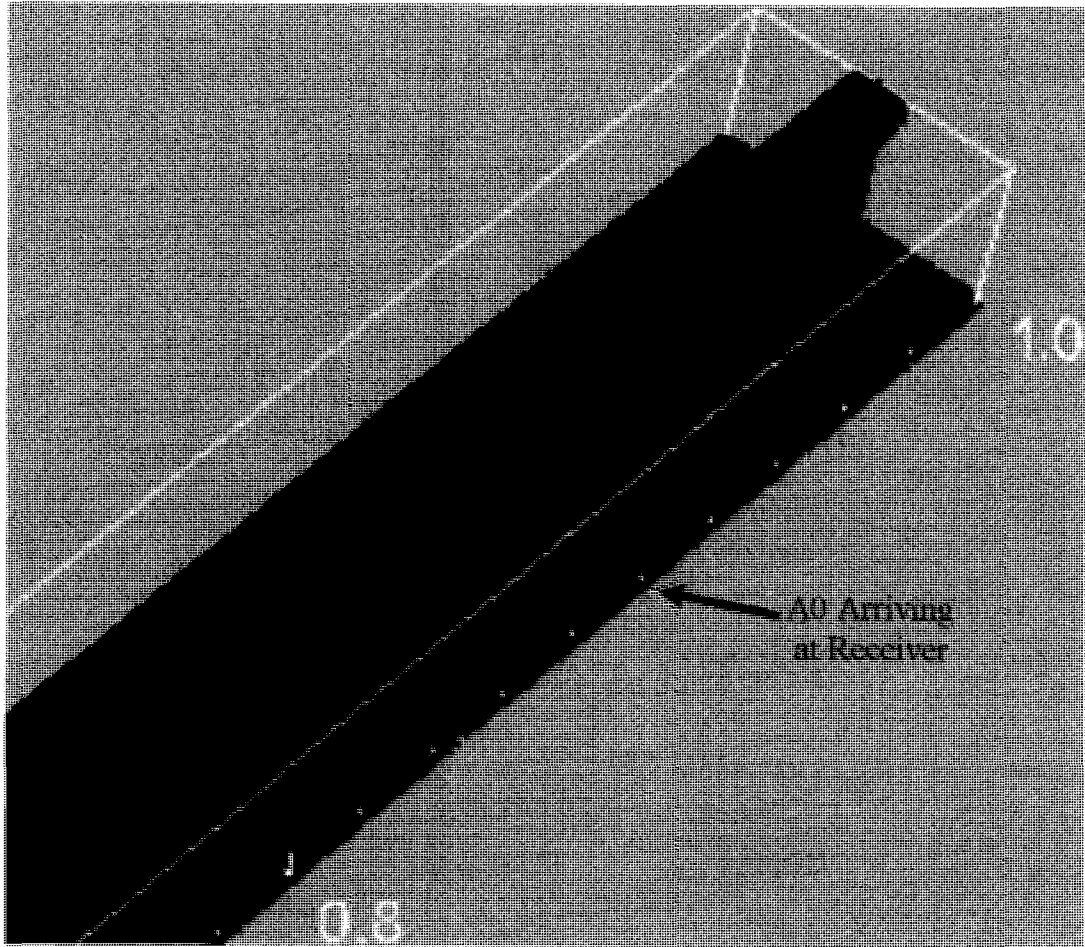
Figure 4.23: Zoom of "T Stringer mode propagation 5.
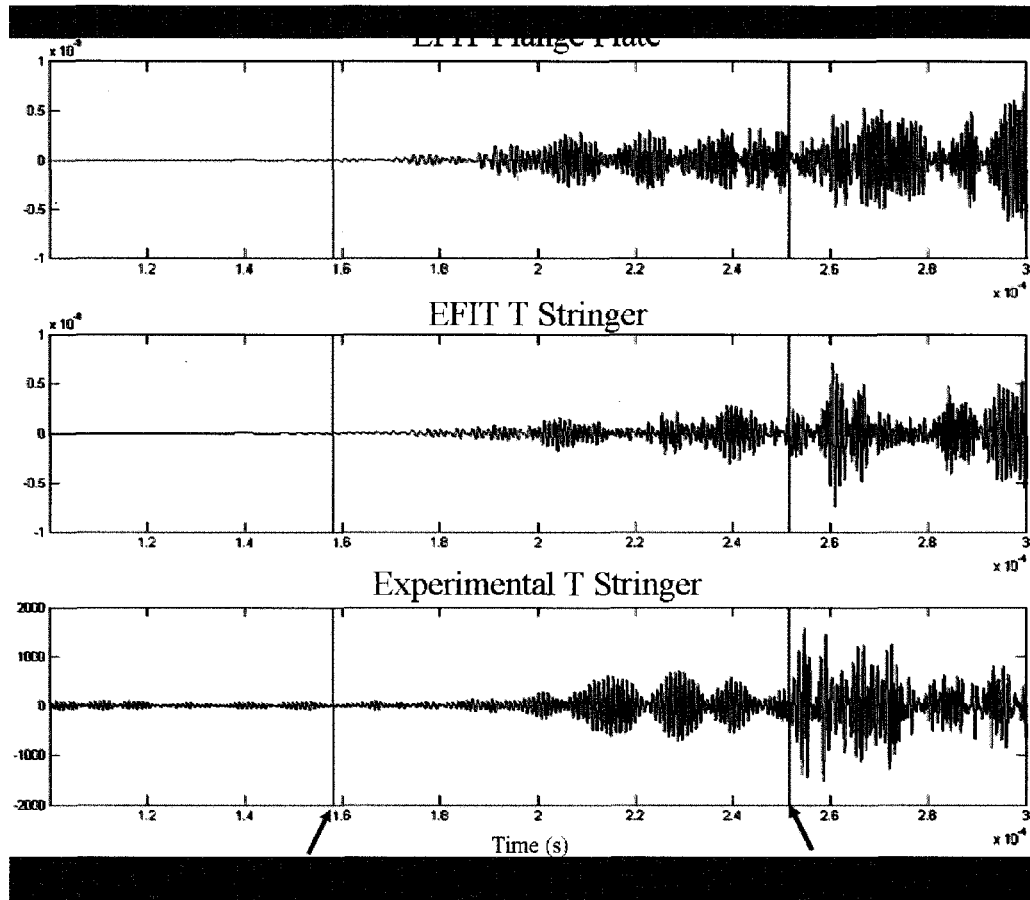
Figure 4.24: Raw waveforms collected from an EFIT simulation of a plate the dimensions of the flange of the aircraft stringer (top), an EFIT simulation of the entire T stringer structure (middle) and the experimental results from the original stringer.
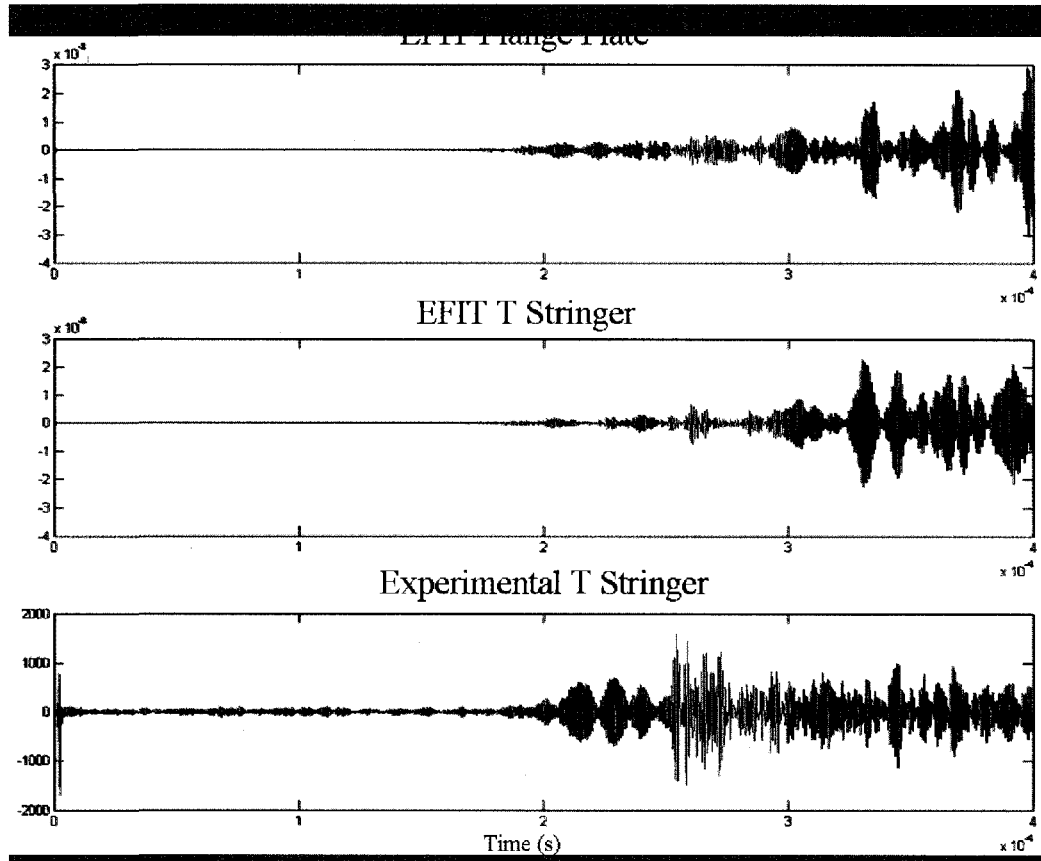
Figure 4.25: Filtered data that corresponds to the flat plate simulation, full T simulation and experiment.

wavelet levels that we filter out by one. In Figure 4.25 we see that the filtering process identifies the A0 wave packet well in all three cases. Applying the DWFT, we see in Figure 4.26 that we can again extract the A0 mode arrival. In the EFIT simulations it seems that the extracted arrival time is consistently 9 μs after the expected arrival from the dispersion curves, as well ~ 6 μs after the experimental times. Other than this discrepancy the structure of the thumb prints are quite similar between the the simulations and the experimental data. This consistency gives us yet more confidence that we are modeling the guided waves correctly with our 3D EFIT.

Figure 4.26: Resulting thumbprints from experiment and simulation.

From here we simulated two steps in the milling experiment. In the simulation space we masked off a 40 cm x 2.15 cm rectangular area of the flange and left its thickness at 1 mm and .488 mm for two different runs. These two steps were chosen from the 11 steps in the milling test because they represent a midpoint and end of material loss from the experiment. Figure 4.27 shows the data progression ending with the extracted A0 arrival times of 259.4, 264.9 and 281.4 μs for the full flange thickness, milled to 1 mm, and .488 mm respectively. If we compare these extracted arrival times for the A0 mode to those found in Figure 3.52 we can see in Figure 4.28 that the same trend is present. As more material is removed from the flange, the A0 mode slows down more and more. We also see the same 9 μs delay in the extracted arrival time from before.

We have shown that our EFIT simulation accurately models the elastic wave propagation for the 3D structure of the aircraft stringer, but we need to better understand the propagation under the corroded surface, which is what lead us toward the simulation method in the beginning. In order to simulate this case we
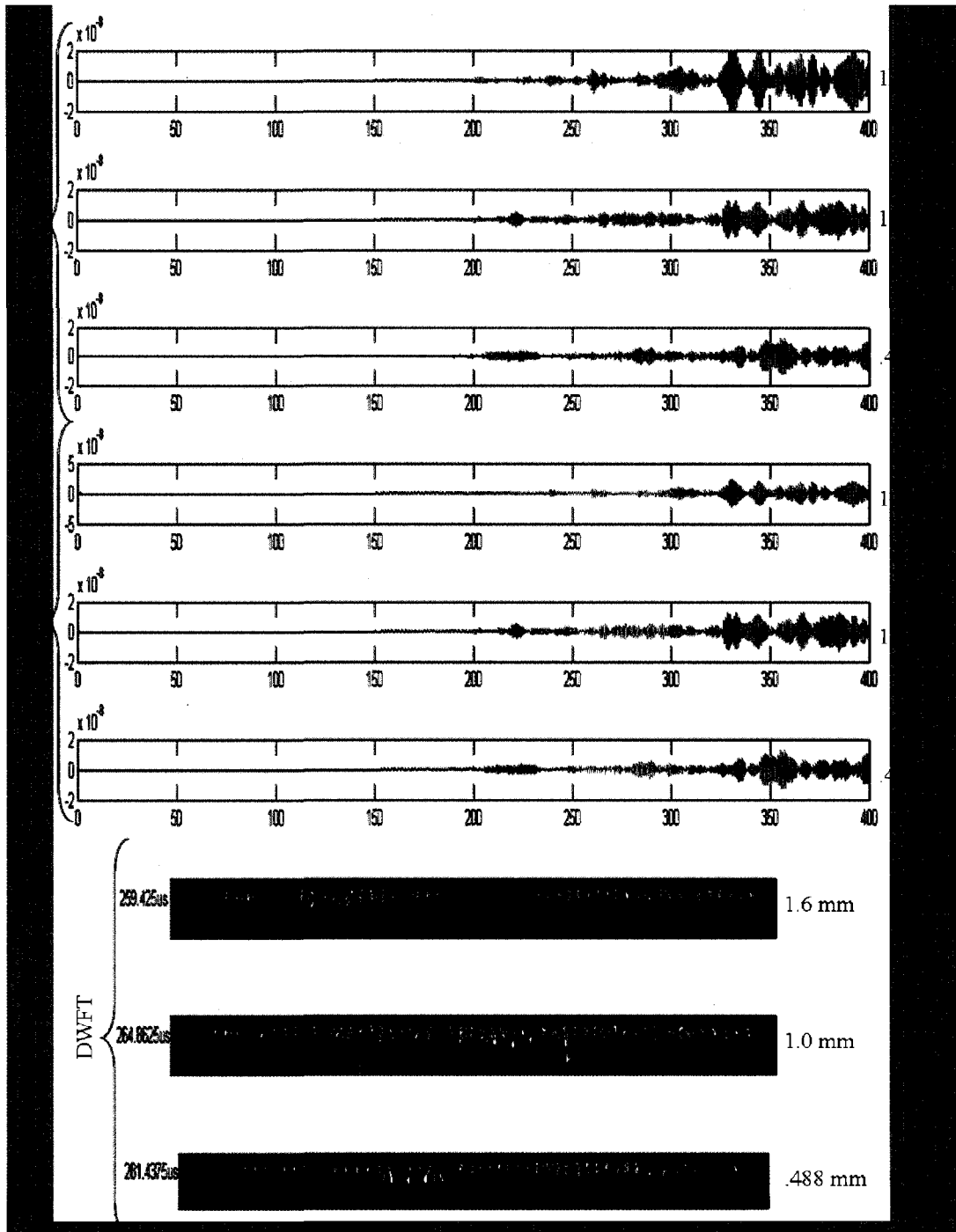
Figure 4.27: Shows the processing of the data from the EFIT simulated milling test.
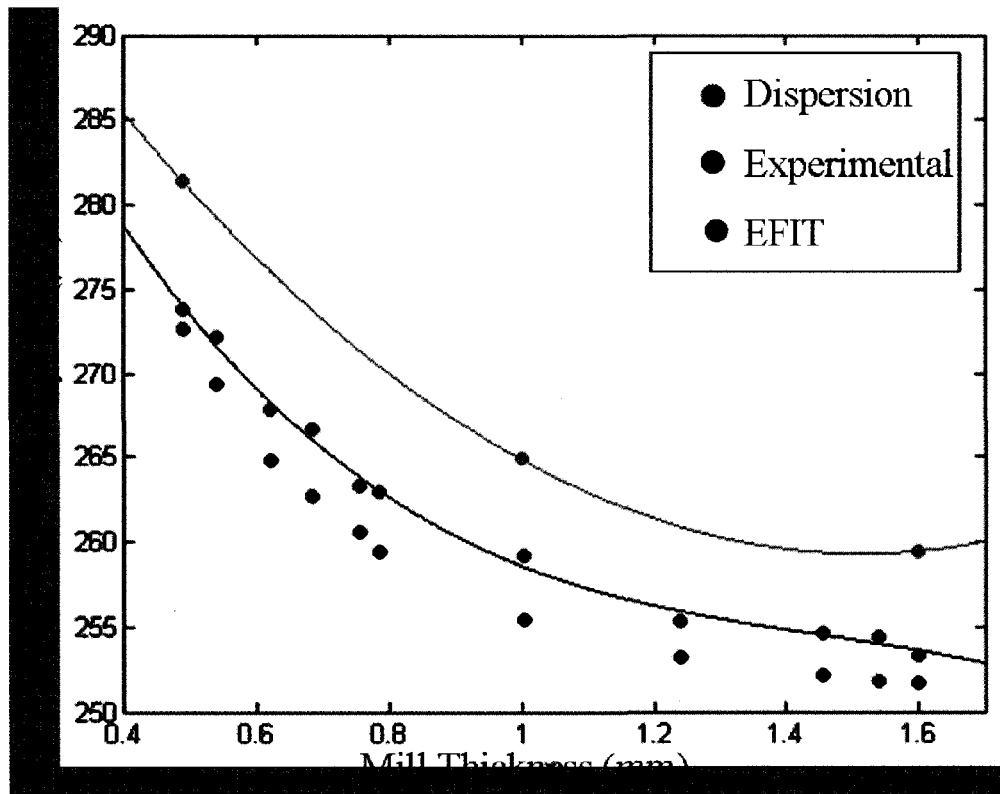
Figure 4.28: Incremental milling test comparison of A0 arrival times to the expected. The black dots show the expected arrival time for each thickness step derived from the dispersion curves, the blue dots show the extracted arrival time from the DFWT thumb prints from experiment and the green dots are extracted from simulated data.

need an accurate map of the hidden surface of the corrosion. In particular, we need a thickness map of the stringer flange under the corroded surface. To find this surface we performed an ultrasonic C-scan of the stringer, in pulse-echo mode. The C-scan is a point by point measurement with the test piece submerged in a water tank, using a focused 20 MHz transducer that raster scans across the corroded area. The ultrasonic energy is focused on the test piece, and the reflections off of the various surfaces are recorded. Instead of scanning from the top of the corroded surface, we turn the T stringer upside down to make the measurements (Figure 4.29). There are reflections from both the top and bottom surface of the test piece, as well as from the bottom of the tank and multiple reverberations due to internal reflection inside the test piece. The corroded surface is mapped by gating the signal around the reflection of interest and recording the time-delay of this echo at each point in the scan.

Once we have recorded the gated signals we relate the shift of the reflection back to the thickness of the flange. This is done by taking the difference of the latest arrival time of the reflection and the arrival of the top surface reflection as the full thickness of the flange. A reflection arriving between these two values can be given a percentage thickness of the whole. Figure 4.30a shows the C-Scan map of the corrosion surface normalized in order to fit the cell size of our EFIT simulation. Recalling the stability criterion (4.12), we make sure that there are enough grid points per "ripple" in the surface. There are various ways to approach this: make the stepsize smaller, which increases the size of the simulation space adding computation time, memory usage and disk storage space; or smooth out the surface somewhat to make sure that the ridges and bumps have enough lateral size to them. Figure 4.30b shows the final surface that we used in the simulation;

Figure 4.29: C-Scan ultrasonic tank filled with water. The focused transducer raster scans across the back of the T stringer recording the reflections from the top and bottom surfaces in order to obtain the thickness map of the corroded surface.

we used a convolution averaging filter with a 10 cell radius in order to obtain this smoothed surface.

Now that we have a matrix that contains the surface we have to map it into the simulation space. This model was run on 100 processors, 25 in the x-direction and 4 in the y-direction. Since we know the step size and model dimensions for this simulation we simply created individual files for the processors that each have a portion of the surface on them. Figure 4.31 shows how the surface was split up between the processors. The processors that do not contain a portion of the flaw are updated as usual. The ones that have the corrosion surface on them update around and under the flaw region as usual, then they step cell by cell through the simulation space for the surface. The matrix for the surface gave a cell number for the top of the surface under which there is a density, above which the density is set to zero. Another array was then created holding a value for the boundaries of the cell. This number is 0 if it is in the interior of the solid, has a 1 or 2 if it is on a boundary in a certain direction. The x direction is determined by the hundreds place, the y by the tens, and z by the ones position. According to this boundary array, we apply the needed equations each time step for each cell. Figure 4.32 shows a snapshot of the guided wave propagation through the corroded region of the aircraft stringer. We see here that the A0 mode is much more distorted due to the corroded surface than is the S0 mode. This is because the through-thickness displacement profile of the A0 mode has the greatest magnitude at the surface of the plate, while the S0 is uniform through the center of the thickness [4]. This allows more of the A0 energy to be scattered in different directions by the uneven surface.
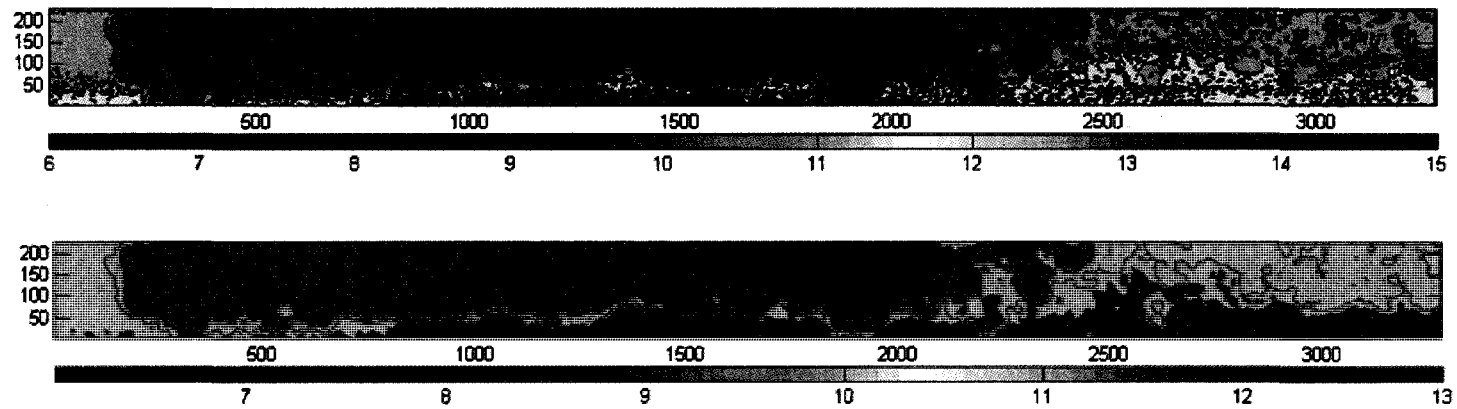
Figure 4.30: C-Scan thickness map of the flange under the corrosion. (Top) No smoothing, (bottom) with a image convolution filter.
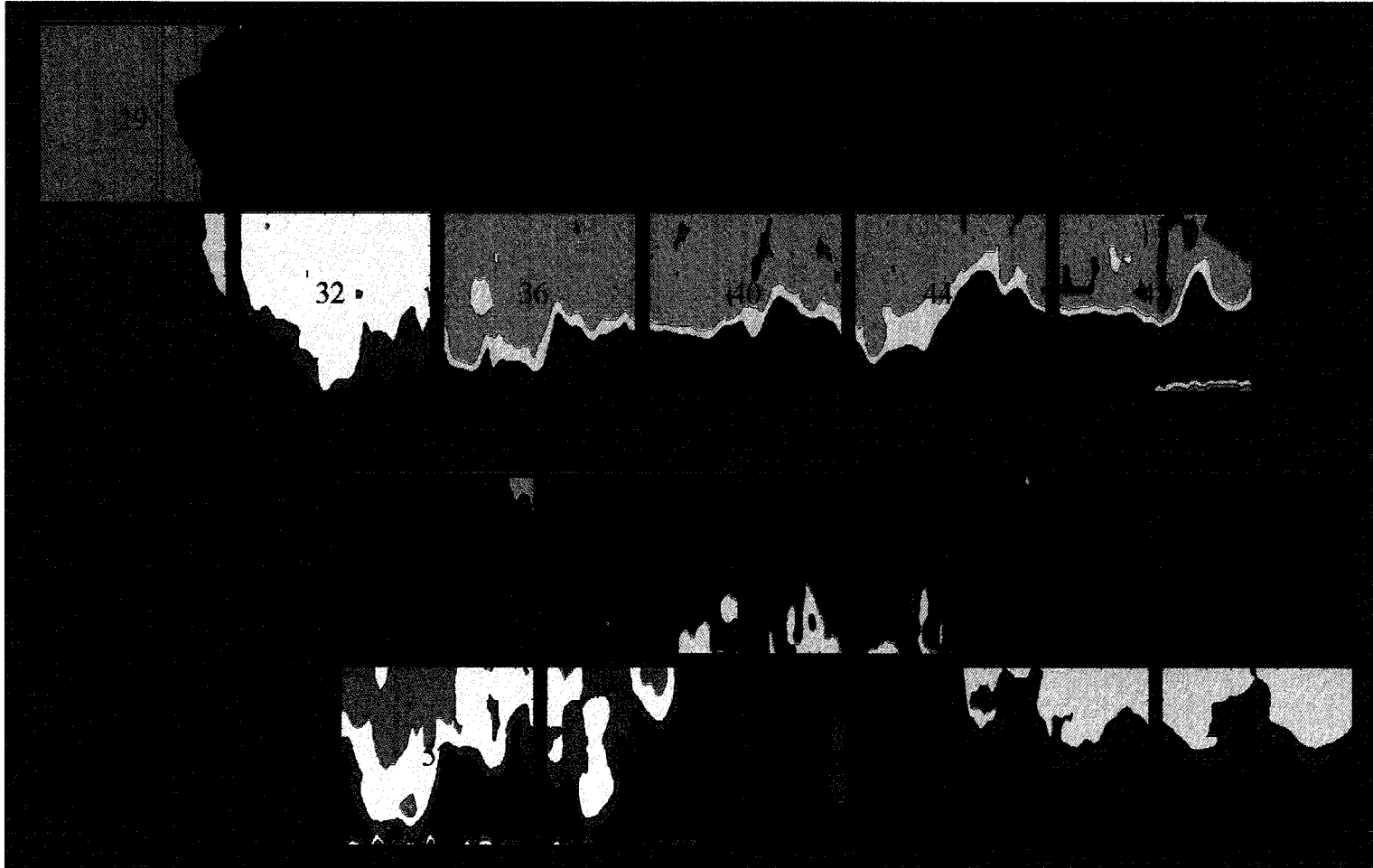
Figure 4.31: The smoothed C-Scan surface was split between the 22 processor that contain the flaw domain.
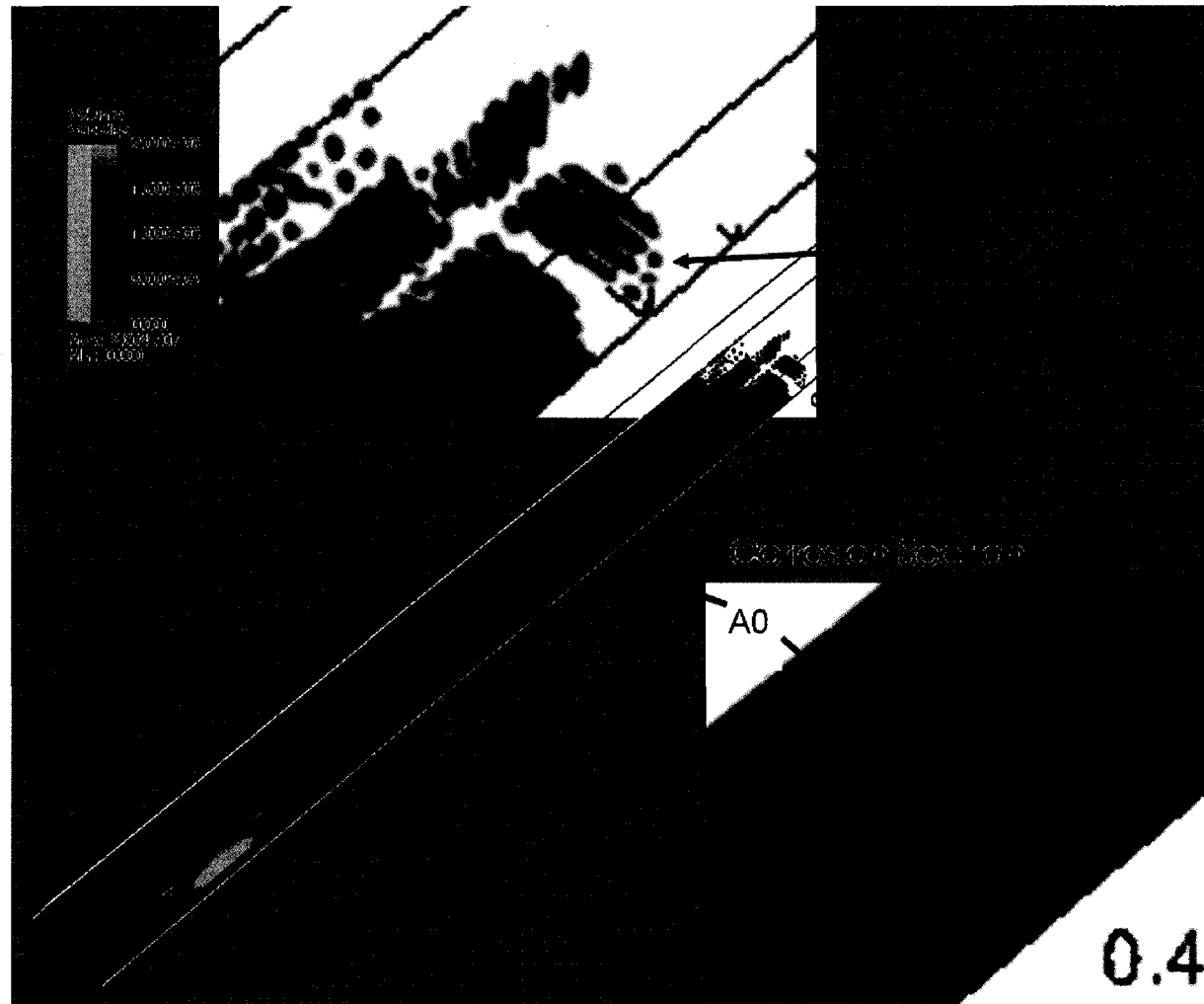
Figure 4.32: Snapshot of EFIT propagation through corrosion surface. The A0 mode is much more distorted by the corroded surface than the S0.

Considering the extracted arrival of the A0 mode from the corroded stringer simulation in the same fashion as before with the experimental data we again see consistency (Figure 4.33). When we compare the thumb prints to those found in Figure 3.56 we see the same features including an early doublet that is followed by the larger doublet feature corresponding to the A0 arrival for a thinned region. From the snapshot images we can tell that the A0 wavefront is very much broken up by the corrosion surface, which could explain the splitting of the features that we discussed in section 3.3.2. In order to examine this in finer detail, we would need a much larger computer which we could track all of the displacement and stress components carefully instead of just recording the magnitude of the displacement vector. This would allow us to watch how the energy is scattered from the surface in great detail. Nevertheless, this simulation shows that the guided wave modes are still propagating under the corroded surface as expected. Further simulations could also systematically investigate which frequency thickness products excite modes that are sensitive to the thickness loss but not as affected by the corrosion surface roughness. Even with these few results from the 3D EFIT simulation we have been able to further identify features and results from the experimental studies that were difficult to explain analytically. With extensive examination of the complete aircraft stringer model we could extend our automatic corrosion detection algorithms to more of the aircraft structure.

4.4.2 Ship Hulls

The EFIT simulation can also be used to investigate the effects of a limpet mine on a simulated ship hull. This scenario at its basic level is more simple to simulate than the aircraft stringers. The ship hull acts as a thick steel plate and the limpet

160
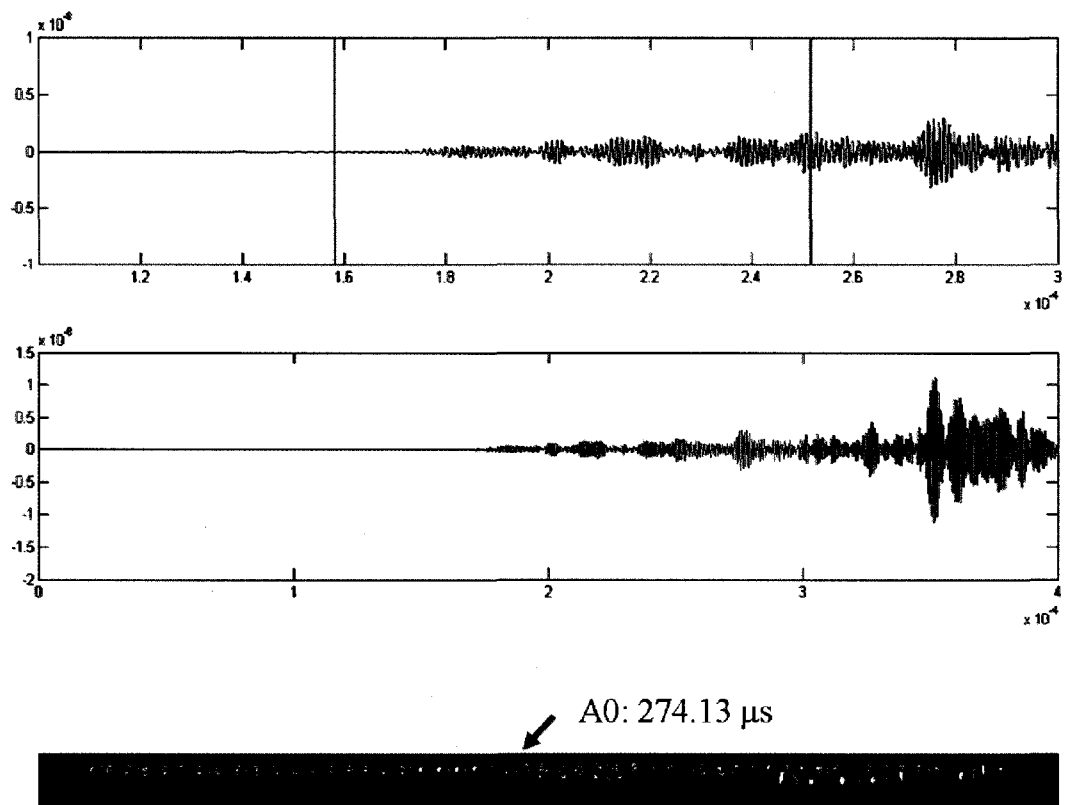
Figure 4.33: Raw waveform, filtered signal and resulting DWFT thumb print for EFIT simulated corrosion sample.

mine, as was seen in our quarter scale dry dock test can be estimated as a 3 kg mass adhered to the plate. For this simulation we modeled the simulation space after the Aberdeen Test 1 (3.1.1). The steel plate was 5/16", which corresponds to the quarter scale midsection hull. We wanted to make the 3 kg mass about the same footprint as the weight and magnets used in the tests. This was achieved by using 6" square by 1.66 cm thick mass. Due to the constraints of the computer cluster, the plate dimensions were limited to .8 m x .8 m for a total propagation length of .3937 m (15.5") which is the same as the shortest distance from Aberdeen Test 1, where the receiver was placed at location A, the transmitter at C and the mine at B from figure 3.1a.

Figure 4.34 shows the simulation space geometry of the mass loading on the plate as well as the elastic guided wave propagating in the expected manner. In order to compare these results to the experimental Aberdeen results we needed alter the DWFT algorithm slightly. This is due to the differences between the experimental data taken in the field versus the idealized computer simulation. Looking at the raw waveforms from the EFIT simulation and comparing them to their experimental counterpart with out the mine present, we can draw some initial conclusions (Figure 4.35). Some of the features are similar to the experimental data sets, but what is interesting is that more of the modes have higher amplitudes which makes the signal more complicated. When we performed the same DWFT algorithm that was used experimentally, the later arriving A0, A1 and S0 features washed out the details of the S0 mode from which we wish to extract mode arrival information from. In order to extract this information we simply narrowed the filtered window to just include the beginning part of the signal containing the S0 arrival. From here we could extract the center of a circular gray feature
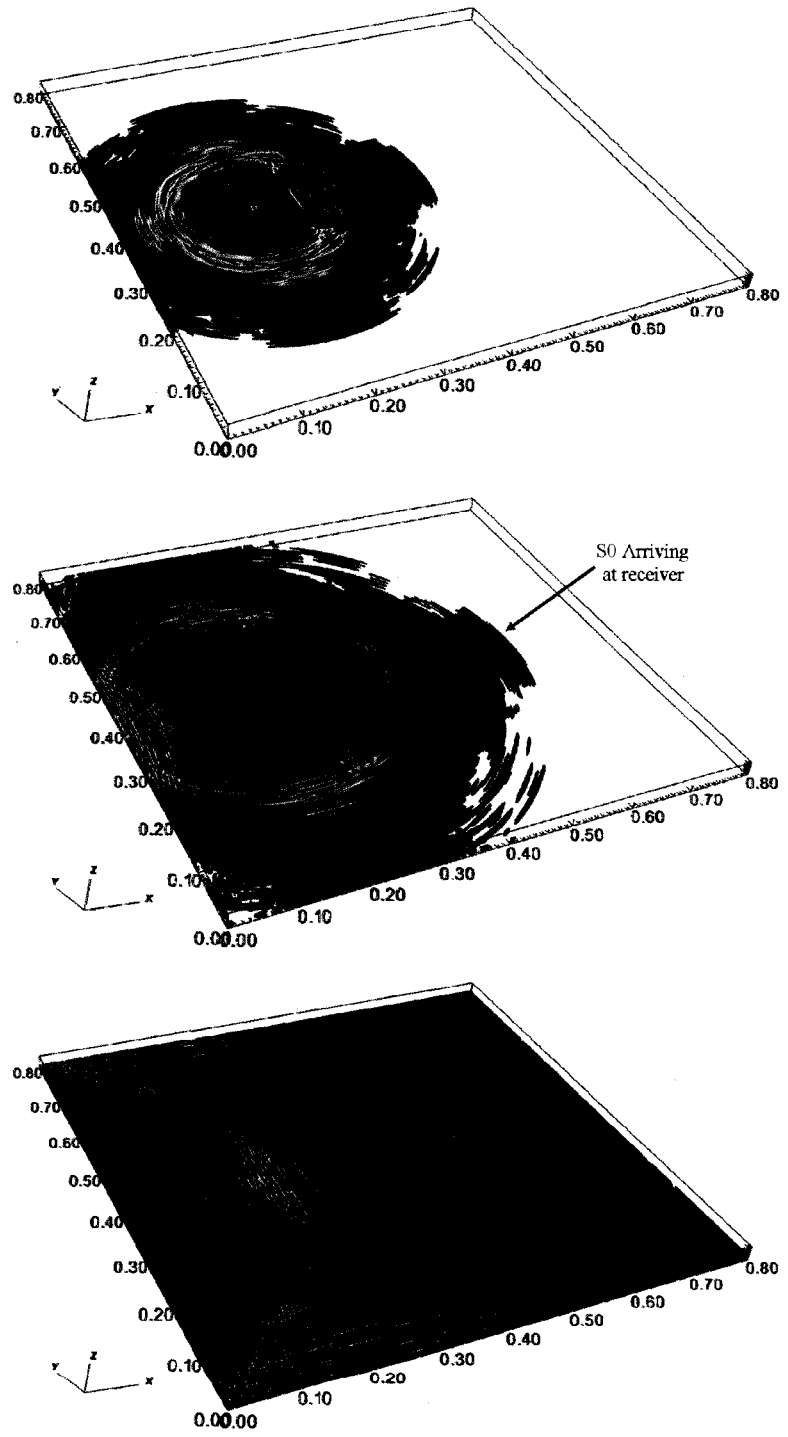
Figure 4.34: As the EFIT simulation steps through time the guided waves interact with the mass loading and keep on propagating through the plate.

163
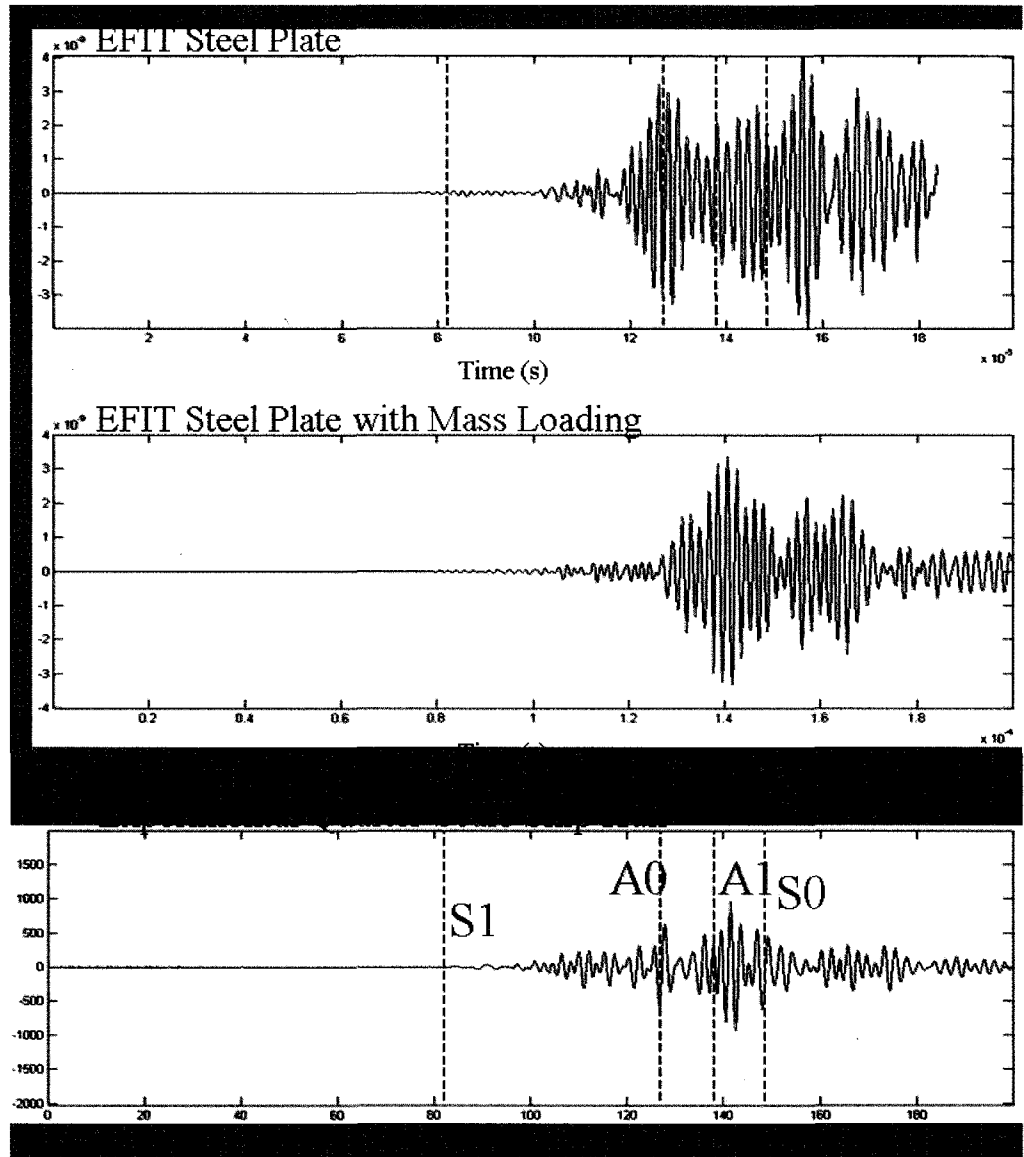
Figure 4.35: Waveforms recorded by EFIT without (top) and with (middle) the mass loading simulating the mock mine using in the experimental test at Aberdeen. The experimental waveform without the mine is also shown (bottom).

164

S1: 92.4 µs
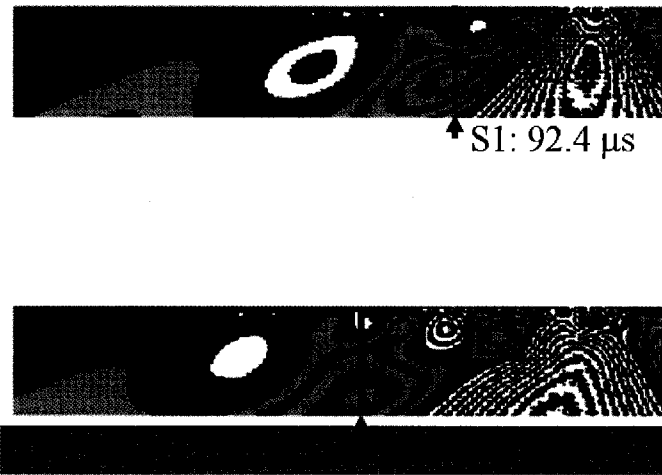
Figure 4.36: The EFIT simulation of a mass loading on a steel plate indicates a speeding up of the S0 mode similar to the results found from experiment.

which corresponds to the S0 mode arrival (Figure 4.36). As with the experimental results, the EFIT simulation reveals a quickening of the S0 mode when there is a mass on the surface of the plate.

These results show that 3D EFIT is capable of simulating the guided waves with sensitivity to a mass loading on the surface. In this simulation the mass was placed directly in the path of the guided waves between the transmitting and receiving transducers. More simulations could study the effect of moving the mass out of the direct path. As seen in Figure 4.34 there are some interesting scattering patterns from the elastic waves as they skirt around the outside of the mass. Studying the simulations, researchers could determine if mode arrival and features from these scattered guided waves could held pinpoint the location of a mass. Another aspect of the guided wave propagation in this application that we saw to be vitally important from the experimental efforts is the transmitting transducer excitation. Using EFIT to systematically optimize the excitation for the detection of the mass loading would tremendously help efforts for robotically automating

this inspection application. The next steps of this line of research would to build up a simulation space with structural pieces attached to the underside of the plate to systematically study their influence on the guided wave mode interaction with the mass loading, and then to continue with the inclusion of surrounding water on one side of the plate in the simulation. Having the results from such a simulation would be very helpful before doing more in water tests. This way the researchers could tell the computer to modify its excitation parameters precisely in order to flesh out the optimum design that could then be automated for further in-situ testing. With the end application in mind, one could imagine the use of multiple robotic sensors operating in both the transmit and receiving modes, searching a large ship hull for an anomaly in the direct guided wave mode arrival times. Then using feature extraction from scattered modes to collectively hunt for the location of the attached mine between the sensors.

4.4.3   Pipeline Coatings

For the application of characterizing unknown protective pipeline coatings, we continued with our development of the EFIT simulation package. EFIT is a full field numeric tool that can be used to visualize and follow what is happening to the elastic energy in a model. The interesting part about the pipeline coatings are that they are viscoelastic. These materials tend to have lower densities, and shear wave velocities (c_s). Therefore considering (4.12) which states that the cell size is determined by setting 10 grid points per slowest shear wavelength, including viscoelastic layers in the simulations increases the simulation space drastically. For the coal tar, Bitumastic 50, the $c_s = 750$m/s which gives a cells size $\Delta s = 7.4e^{-5}$m. In order to create a simulation space of 2' x 1.5' which is on the order of the same

Material	$\rho\ (kg/m^3)$	$v_l\ (m/s)$	$v_s\ (m/s)$
Steel	7800	5940	3220
Carboline Bitumastic 50	1500	1860	750
Mereco 303 (Epoxy 1) [49]	1080	2390	990
DE & C 2057 / Ca9 (Epoxy 2)	1600	2960	1450

Table 4.1: Material properties for the three simulated coatings as well as that of the steel plate substrate used in the 3D EFIT

dimensions as experiment, requires 6.91×10^9 cells. In order to perform the EFIT simulation this means that we need around 552.9 GB of physical memory. We accomplished this by using 260 cores for the parallel processing. With this huge simulation space, the cluster completed 83336 time steps in just over 98 hours.

We completed EFIT simulations for 2 different epoxy coatings as well, although they are slightly different materials than the experimental epoxies since all the needed viscoelastic properties are unavalable. Table 4.1 lists the material densities and wave speeds for all three of the coatings simulated.

Fortunately, as expected from experiment, the shear wave velocities for both of the epoxies were greater than that of the Bitumastic 50, so we could more easily manage the use of the available computational cluster resources. This also results in shorter simulation times. We did run into some computer availability issues since these simulations require almost the entire parallel cluster at William and Mary.

The preliminary results from these simulations look promising and point toward more research to study the guided waves in multi-layered systems. From the raw waveforms (Figure 4.37), we can see that there is some difference in the signals from experiment (Figure 3.36). In the EFIT waveforms we can relate the structures seen in the plain steel simulation to the guided wave modes expected

167

from the dispersion curves (Figure 3.34). The waveforms for both the plain steel plate and the Bitumastic 50 coating are cut short because of computational cluster availability. Since the overall structure of the waveforms is so different from their experimental counterparts, the previously developed DWFT feature extraction algorithm does not produce meaningful results for these waveforms. We do however, expect that there exists a scheme that would easily extract mode arrival data from these signals. Preliminary efforts show some interesting detail of some DWFT features. Figure 4.38 shows an example of this line of investigation. It appears that the DFWT results in some fairly distinct features for each of the first three mode arrivals. The arrival of the later S0 mode isn't included because in order to have a wavelet thumb print window that was comparable across all of the EFIT signals we had to reduce its length. With complete simulations we could extend the window to examine all of the features. The blue brackets indicate the features corresponding to the S1 mode, the green ovals to the A0 and the red box to the A1. For the A0 and A1 modes, even though a shift in arrival is readily apparent, it seems there is a correlation to their size and shape to the material properties of the coating. However, without more data, and full recorded signals from all of the coating configurations it is hard to say if these artifacts are happenstance or if they represent actual trends in the data.

Utilizing the EFIT simulations to examine what is happening in these signals would help identify the aspects of the experimental approach that are different from these. The signals are not so different that the underlying physics is being misrepresented in either case, but rather there are experimental effects that are that are hiding useful information in the noisy experimental data. The EFIT simulations could shed some light on how to either recreate the experimental data

168
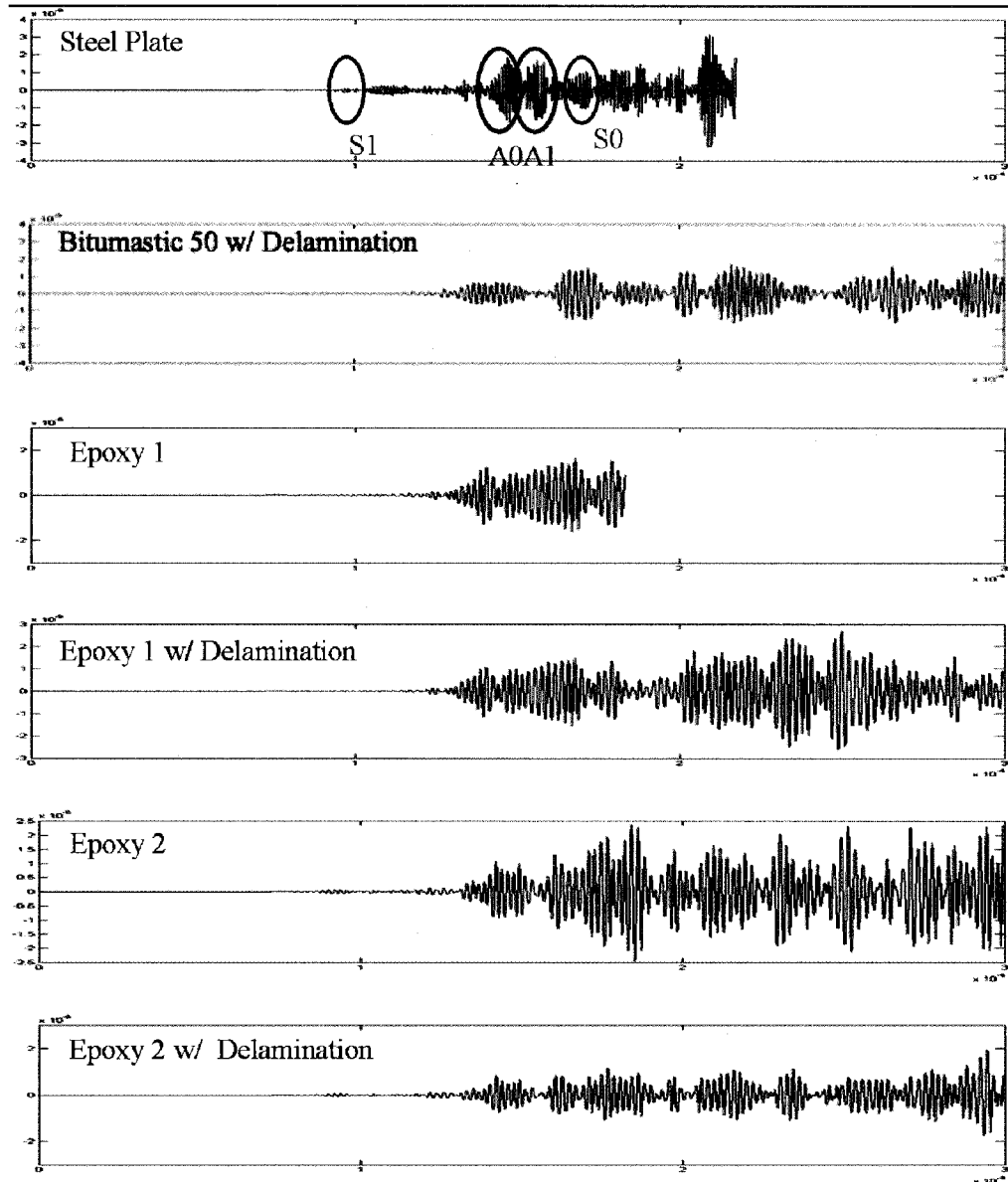
Figure 4.37: The EFIT simulation results appear different from their experimental counterparts. In the steel plate waveforms we can see the structure of each of the guided wave modes expected from the dispersion curves.
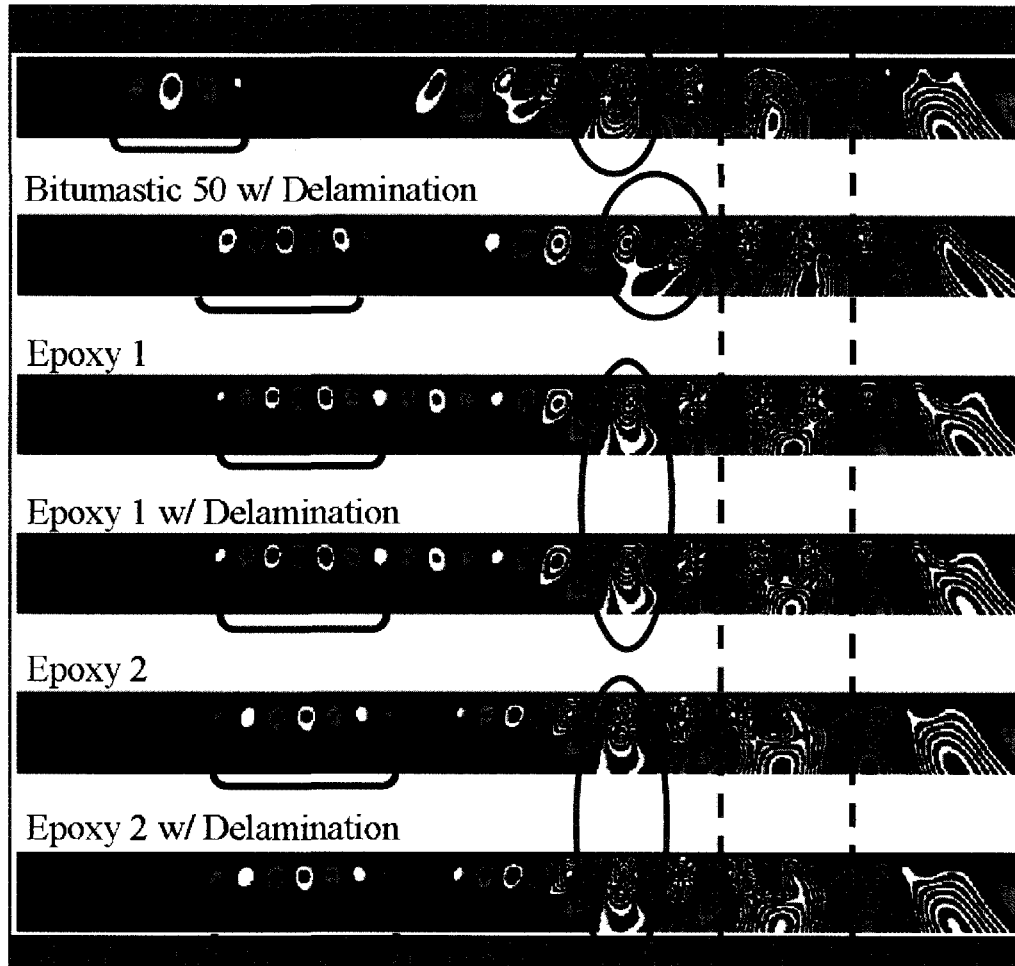
Figure 4.38: The EFIT simulation viscoelastic coatings on a steel plate with a delamination produce some interesting features in the DWFT thumb prints. Features from the first three modes are indicated by the blue brackets, green ovals and red box

or how to process the data in a more informative way that also is upheld by the simulated data.

Chapter 5

Conclusions & Future Work

In this work we have shown how elastic guided waves are a good tool for inspecting structures for quantitative information about their structural status and environment. Knowledge of how elastic guided waves behave for idealized cases allows for initial investigation of real structures. Full understanding of a system is derived from combining full field computational results with expertise from experimental aspects of an application. Even though we have presented work related to three specific structural health applications we contend that the same approach may be used for numerous other SHM applications. This is because we approach the problem from the point of extracting the meaningful guided wave information not the application itself. Our three applications of searching large ship hulls for attached Limpet mines, characterizing material properties and deterioration of protective coatings on large diameter pipelines, and corrosion thickness loss detection of aircraft structural stringers, all represent quite different configurations. However, once we have the waveform data, the extraction of the guided wave mode information is quite similar. The meaning of this information is where the

specific differences arise. We have shown results from interpreting guided wave interactions with thickness reduction (thinning) flaws, delaminations of material layers with unknown material parameters, and localized mass loadings on a plate. All of these utilize the dispersive nature of the guided wave modes to provide information about the structure. Since full analytic solutions for the real structures are not even conceptually possible, full field computer simulations using 3D EFIT are used to help interpret the signals from experiments and give us better insight in to what is happening to the guided wave energy as it interacts with various flaws.

It was demonstrated that the DWFT algorithm could successfully be used to show that differences can be identified between different unknown coatings on pipes. Furthermore, it was shown that the guided waves in layered material are sensitive to delaminations of the coating from the pipe wall. Because of the dispersive nature of the guided waves, they would change propagation velocity or mode convert depending on if the propagation path was directly through the delamination or not. We found that the developed wavelet filtering with the DWFT could extract the feature corresponding to this change in guided wave propagation and render it as a change in the thumb print feature which is automatically interpretable as a change in the properties of the pipe and coating structure. The motivation from the Department of Transportation was to be able to identify multiple types of coatings, with our preliminary findings from implementation of the EFIT simulation it appears that the DWFT features correspond in shape and size to the material properties of the coating as well as holding information of the arrival of the guided wave modes. Further research is needed to systematically examine placement and sizing of flaws under many kinds of coatings in order to

173

optimize the most informative feature extraction.

We also demonstrated that guided waves interact in a predictable way when propagating along a ship hull with a mass loading on it. This proof-of-concept research was conducted both on a new proptptype vessel in dry dock and on a older ship in turbid waters. In the latter test the need for a better way to find Limpet mine attachment to the underside of ship hulls was very apparent, since the divers could not see more than an inch in front of them. We demonstrated that the guided waves do travel extended distances along the curved geometry of the ship hull gaining information about the hull as they propagate. When a mine or a mock mine was present in the propagation path, the symmetric modes of interest increased their speed. Using a filtering scheme with the DWFT we were able to identify a feature in the thumb prints that corresponds to this change in propagation. Since the experimental tests were conducted in the field, both from the dry dock quarter scale destroyer at Aberdeen and on the hull of the Del Monte in the water at Little Creek, the data was at times noisy due to environmental factors, but we found that the DWFT was still able to extract meaningful arrival times of the guided wave modes from the signals. From these experiments it became apparent that in order to fully understand features extracted from the signals, we needed a more controlled environment. However, even under the circumstances of having little communication and control over the test apparatus we were able to collect informative data about the status of the ship hull.

The next step in this line of research is to continue optimizing the excitation of the guided waves in the ship hull. Our EFIT simulations showed that we could used their results to examine the details of the guided waves with the mass loading of the surface of the simplified ship hull. With further work we would be able to

down-select the excitation parameters so that a robotic implementation of the the REMORA testing scheme is feasible. Furthermore, by including more of the ship hull structure in the EFIT models we could select a guided wave mode that was most sensitive to the mass loading, with minimum effect from the rest of the ship structure. Another interesting area of research that came to light through the EFIT simulations is the scattering of the guided wave modes from the surface mass. Algorithms that would extract features from these scattered signals could help locate a mine on the ship hull even with a sparse data grid.

Our final application of guided wave interaction with corrosion on aircraft structural stringers showed further robustness of the DWFT. Automatic extraction of the A0 mode with minimal prior knowledge of stringer state was shown to correspond to the thickness loss of a section of the stringer. Starting with the initial dimensions of the stringer, and knowledge of the guided wave mode behavior, we extracted guided wave arrival automatically. For use in the field this would be implemented as a inspection technique where the extracted arrival time would tell the thickness of the stringer, deviation from the expected would be a flag for maintenance of that structure.

An interesting observation in the experimental work on the stringers was that it was difficult to extract the first arriving mode from the signals. Instead we used information from the later arriving A0 mode. In addition to confirming findings of the material-thickness loss causing a slowing of the A0 mode, the EFIT simulations shed light on the missing S0 features. In the initial analysis, as with traditional guided wave analysis, the "T" stringer was approximated by a thin plate with the dimensions of the flange of the stringer. The EFIT simulation showed that this model, although correctly predicting the propagation of the A0 mode, is too

simple to explain the S0 propagation. From the simulation visualization we see that the S0 mode is attenuated by the web structure so much that by the time that mode propagates the stringer length it is not resolvable from the noise, which was the exact situation that we were seeing from the experimental data. Furthermore, the EFIT simulation accurately modeled the effect of the corroded surface on the guided waves. Here we saw the A0 mode breaking up from scattering by the rough surface because of its displacement magnitude being concentrated on that surface. With such EFIT simulations further research could study in detail how much surface roughness is required to to perturb the A0 mode propagating down the stringer, this could be used as a simple threshold alarm mechanism in a field able inspection device.

In each of these applications, the idealized analytical approach was sophisticated enough to predict a portion of the results, but when considering the larger picture of the system we found that the EFIT simulations provided needed analysis of the subtle guided wave propagation. Our 3D implementation of EFIT has shown its usefulness to simulate guided waves in each of the diverse applications. Using EFIT in future work will continue to bring to light the subtleties of the propagation of guided waves in real structures. One of the best uses for this algorithm is in the planning of experimental tests where there is complex geometry that can not be solved for analytically. One of the fastest ways of gaining initial understanding of the results from the EFIT simulations is by visualizing the data. Due to storage constraints we collapsed the amount of data down to just recording the magnitude of the displacement vector every 200 time steps. We are thus discarding 99% of the generated data. It would be of great interest to look at not only the displacement magnitudes but their direction and even some of the stress

176

tensor field components. Visualizing the stresses as the guided waves propagate, or even as a test piece was under stress loading while being inspected would be a valuable resource to gain much more information about the structure under test.

Guided Lamb wave modes have been shown to propagate and interact with structure and flaws for each of our applications. The modes of interest in each case change their propagation according to the structure allowing us to see changes due to mass loadings, delaminations of coatings and corrosion thickness loss. We have developed DWFT algorithms that have proven to be able to extract features from the guided wave signals that give information about the structures. Finally we've shown that using developed the EFIT simulation package we can understand and predict the propagation of the guided wave modes better than with analytical tools alone.

Appendix A

TDR GUI User Manual for DWFT
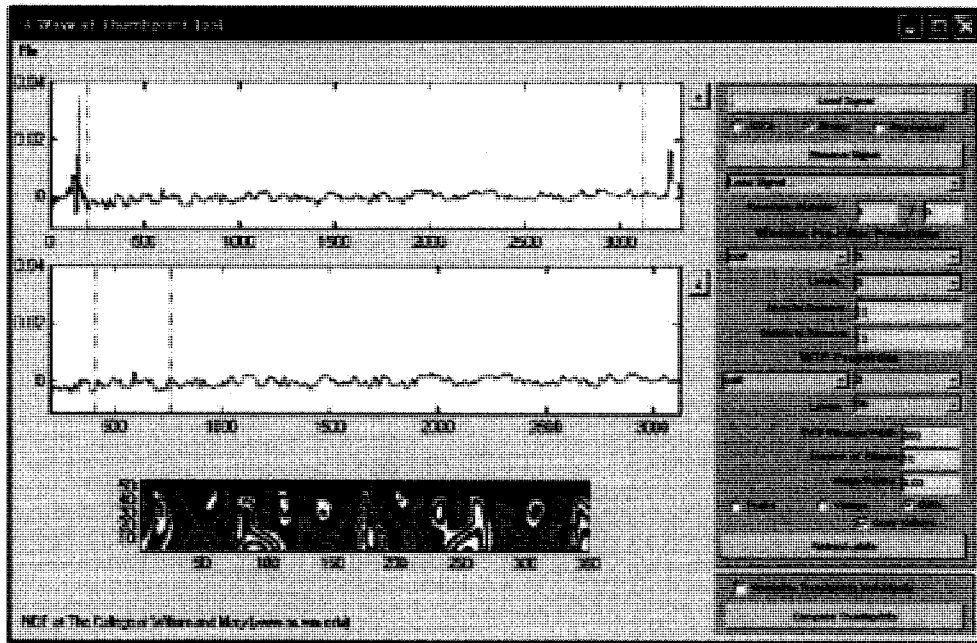
The Wavelet Thumbprint Tool (WTPtool) provides a simple and interactive user interface that can be used to create and view Wavelet Thumbprints for time series signals in order to recognize characteristic patterns associated with wiring flaws.

A.1 To Run the Wavelet Thumbprint Tool

To use the Wavelet Thumbprint Tool you must have a current version of MATLAB with the Wavelet Toolbox. To run the Wavelet Thumbprint Tool, enter wf in the MATLAB command window.

A.2 Loading and Viewing signals

TDR signals are loaded using the Load Signal button. Depending on the typed data select either "Binary" or "ASCII" or if the signal is contained in a workspace variable: "Workspace." More than one signal can be loaded during a single session. The pop-down menu located below the Remove Signal button can be used to select a signal to be viewed. When pressed, the Remove Signal button will remove the current signal. Once a signal is loaded, you will see three plots on the left hand side of the window. An example is shown below for a Time Domain Refectometry (TDR) signal.

Left and Right Boundary
(Movable by left and right
clicking on the Raw Data Plot)

Wavelet Thumbprint Window
(Movable by clicking on the Filtered
Data Plot)

Wavelet Thumbprint
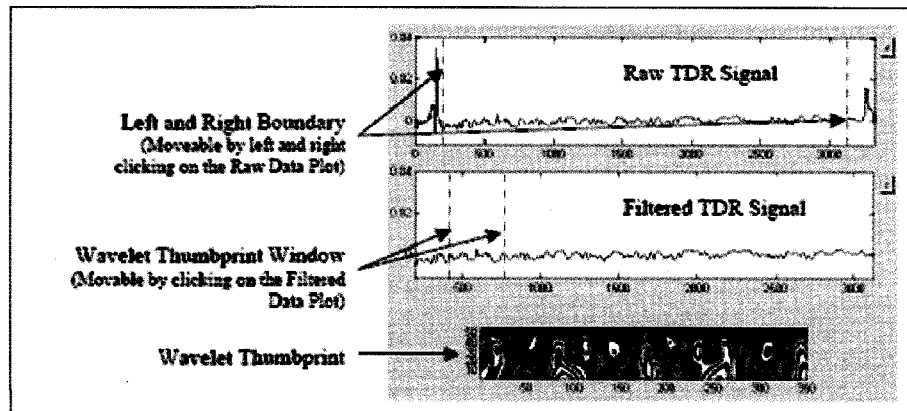
A.2.1   Raw TDR Signal

The top plot displays the raw TDR signal. The purple lines represent the left and right cropping boundaries. These can be set by clicking the left and right mouse button.

A.2.2   Filtered TDR Signal

The second plot displays the filtered TDR signal. The data is filtered according to the Wavelet Pre-filter (denoise) properties on the right hand side of the window. The purple lines on this plot indicate the section of the filtered data that will be used in making the Wavelet Thumbprint. This Wavelet Thumbprint window can be moved by clicking on the plot or using the left and right arrow keys.

A.2.3   Wavelet Thumbprint of the TDR Signal

The last plot displays the Wavelet Thumbprint that is created according to the Wavelet Thumbprint (WTP) properties on the right hand side of the window. Right clicking on this plot or the filtered data plot will place a red reference line on both plots. This can be used to indicate which two-dimensional features in the Wavelet Thumbprint correspond to the one-dimensional features in the TDR signal.

A.3   Wavelet Pre-Filter Properties

A Wavelet Pre-Filter is performed on the raw signal using a discrete stationary wavelet transform. This separates the signal into its details (high scales) and its approximations (low scales). These parts can then be individually removed

180

— Wavelet name used in the pre-filter
— Number of levels used in the wavelet transform
— Approximation levels to remove in the inverse transform
— Detail levels to remove in the inverse transform

— Wavelet name used in the continuous wavelet transform
— Number of levels used in the wavelet transform
— Width of the Wavelet Thumbprint window
— Number of ridges used to create the Wavelet Thumbprint
— Width of the ridges (Normalized to 1)

from the signal. The default settings do not remove any approximation or detail levels. For example, if you wanted to remove the first three levels of the details (commonly used to denoise a signal), then the appropriate entry in the Details to Remove: field would be [1 2 3] or [1:3].

A.4 Wavelet Thumbprint (WTP)

A.4.1 Properties

The Wavelet Thumbprint is created by taking a continuous wavelet transform of the filtered signal. The coefficients of the wavelet transform are then represented as a set of ridges that resemble fingerprints.

A.4.2 Different Views of the Wavelet Thumbprint

Selection buttons are provided to display only the peaks (positive values), the valleys (negative values), or both peaks and valleys of the Wavelet Thumbprint. When both peaks and valleys are displayed, the Gray Valleys option will shade the valleys in gray so that they are distinguishable from the peaks.

— View selection buttons
— Option to gray the valleys (negative values) of the WTP
— Refresh the plots using the current settings

181
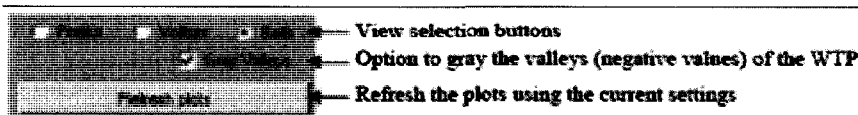
A.4.3 Compare Thumbprints

The Compare Thumbprint button will display Wavelet Thumbprints for all of the loaded signals using the current settings. The thumbprints are displayed from top to bottom in the same order as they were loaded and appear in the pop-down menu. The Normalize Thumbprints Individually option will normalize each signal separately before the thumbprints are created.

Appendix B

Matlab Code for Ship Hull Data Extraction

Appendix C

Matlab Code for Pipe Coatings

Appendix D

Matlab Code for Aircraft Stringers

Appendix E

FORTRAN 90 Source Code for EFIT

Bibliography

[1] J. D. Achenbach. *Wave Propagation in Elastic Solids*. North Holland, New York, 1984.

[2] B. A. Auld. *Acoustic Fields and Waves in Solids*. Kreiger, Malabar, FL, 2nd edition, 1990.

[3] K. E. Graff. *Wave Motion in Elastic Solids*. Dover, New York, 1991.

[4] J. L. Rose. *Ultrasonic Waves in Solid Media*. Cambridge University Press, New Your, 1999.

[5] I. A. Viktorov. *Tayleigh and Lamb Waves - Physical Theory and Applications*. Plenum Press, New York, NY, 1967.

[6] Joseph L. Rose. A baseline and vision of ultrasonic guided wave inspection potential. *Journal of Pressure Vessel Technology*, 124:273–282, August 2002.

[7] Ajay Raghavan and Carlos E. S. Cesnik. Review of guided-wave structural health monitoring. *The Shock and Vibration Digest*, pages 91–114, 2007.

[8] James C. P. McKeon. *Tomography Applied to Lamb Wave Contact Scanning*. PhD thesis, William and Mary, Williamsburg, 1998.

[9] J. C. P. McKeon and M. K. Hinders. Lamb wave scattering from a through hole. *Journal of Sound and Vibration*, 224(5):843–862, 1999.

[10] J. C. P. McKeon and M. K. Hinders. Parallel projection and crosshole lamb wave contact scanning tomography. *Journal of the Acoustical Society of America*, 106(5):2568–2577, 1999.

[11] J. C. P. McKeon and M. K. Hinders. Lamb wave contact scanning tomography. *Review of Progress in Quantitative Nondestructive Evaluation*, 18:951–958, 1999.

[12] Eugene V. Malarenko. *Lamb Wave Diffraction Tomography*. PhD thesis, William and Mary, Williamsburg, 2000.

[13] E. V. Malyarenko and M. K. Hinders. Fan beam and double crosshole lamb wave tomography for mapping flaws in aging aircraft structures. *Journal of the Acoustical Society of America*, 108(4):1631–1639, 2000.

[14] E. V. Malyarenko and M. K. Hinders. Ultrasonic lamb wave diffraction tomography. *Ultrasonics*, 39(4):269–281, 2001.

[15] K. R. Leonard, E. V. Malyarenko, and M. K. Hinders. Ultrasonic lamb wave tomography. *Inverse Problems*, 18(6):1795–1808, 2002.

[16] Mark K. Hinders, Kevin R. Leonard, and Eugene V. Malyarenko. Blind test of Lamb wave diffraction tomography. *Review of Progress in Quantitative Nondestructive Evaluation*, 21:278–283, 2002.

[17] K. R. Leonard and M. K. Hinders. Guided wave helical ultrasonic tomography of pipes. *Journal of the Acoustical Society of America*, 114(2):767–774, 2003.

[18] Kevin Leonard. *Ultrasonic Guided Wave Tomography of Pipes*. PhD thesis, College of William and Mary, 2004.

[19] K. R. Leonard and M. K. Hinders. Lamb wave helical ultrasonic tomography of pipes. *Review of Progress in Quantitative Nondestructive Evaluation*, 23:173–179, 2004.

[20] K. R. Leonard and M. K. Hinders. Lamb wave tomography of pipe-like structures. *Ultrasonics*, 43(7):574–583, 2005.

[21] K. R. Leonard and M. K. Hinders. Multi-mode lamb wave tomography with arrival time sorting. *Journal of the Acoustical Society of America*, 117(4):2028–2038, 2005. Part 1.

[22] K. R. Leonard and M. K. Hinders. Lamb wave tomography of pipes and tanks using frequency compounding. *Review of Progress in Quantitative Nondestructive Evaluation*, 24:867–874, 2005.

[23] J. Hou. *Ultrasonic signal detection and recognition using dynamic wavelet fingerprints*. PhD thesis, College of William and Mary, 2004.

[24] J. Hou, K. R. Leonard, and M. K. Hinders. Multi-mode lamb wave arrival time extraction of improved tomographic reconstruction. *Review of Progress in Quantitative Nondestructive Evaluation*, 24:736–743, 2005.

[25] Lord Rayleigh. On Waves Propagated Along the Plane Surface of an Elastic Solid. *Proceedings of the London Mathematical Society*, 17:4–11, 1885.

[26] Horace Lamb. On waves in an elastic plate. *Proceedings of the Royal Society of London Series A*, XCIII:114–128, 1917.

[27] R. D. Mindlin. Influence of rotatory inertia and shear on flexural motions of isotropic elastic plates. *Journal of Applied Mechanics*, pages 31–38, March 1951.

[28] D. C. Worlton. Ultrasonic testing with lamb waves. *Nondestructive Testing*, 158(4):218–222, July-August 1957.

[29] D. C. Worlton. Experimental confirmation of lamb waves at megacycle frequencies. *Journal of Applied Physics*, 32(6):967–971, June 1961.

[30] D. C. Gazis. Three-dimensional investigation of the propagation of waves in hollow cylinders. i: Analytical foundation. *Journal of the Acoustical Society of America*, 31:568–573, 1959.

[31] D. C. Gazis. Three-dimensional investigation of the propagation of waves in hollow cylinders. ii: Numerical results. *Journal of the Acoustical Society of America*, 31:573–578, 1959.

[32] J. Li and J. L. Rose. Natural beam focusing of non-axisymmetric guided waves in large-diameter pipes. *Ultrasonics*, 44(1):35–45, 2006.

[33] Wei Luo, Xiaoliang Zhao, and Joseph L. Rose. A Guided Wave Plate Experiment for a Pipe. *JOURNAL OF PRESSURE VESSEL TECHNOLOGY*, 127:345–350, AUG 2005.

[34] Adnan H. Nayfeh and Elsayed Abel-Ati M. Nassar. Simulation of the Influence of Bonding Materials on the Dynamic Behavior of Laminated Composites. *Journal of Applied Mechanics*, 45:822–828, DEC 1978.

[35] Richard O. Claus and Ronald A. Kline. Adhesive bondline interrogation using stoneley wave methods. *Journal of Applied Physics*, 50(12):8066–8069, December 1979.

[36] Michael Schoenberg. Elastic wave behavior across linear slip interfaces. *Journal of the Acoustical Society of America*, 68(5):1516–1521, 1980.

[37] Y. Tsukahara and K.Ohira. Detection of smooth bondings of polymer coating by ultrasonic spectroscopy. *Ultrasonics*, 27:3–7, 1989.

[38] P.-C. Xu and S. K. Datta. Guided waves in a bonded plate: A parametric study. *Journal of Applied Physics*, 67(11):6779–6786, June 1990.

[39] Adnan H. Nayfeh. The general problem of elastic wave propagation in multi-layered anisotropic media. *JOURNAL OF THE ACOUSTICAL SOCIETY OF AMERICA*, 89(4):1521–1531, APRIL 1991.

[40] J. Laperre and W. Thys. Experimental and theoretical study of lamb wave dispersion in aluminum/polymer bilayers. *Journal of the Acoustical Society of America*, 94(1):268–278, July 1993.

[41] P.-C. Xu, K.-E. Lindenschmidt, and S. A. Meguid. A new high-frequency analysis of coatings using leaky lamb waves. *Journal of the Acoustical Society of America*, 94(5):2954–2962, November 1993.

[42] J. L. Rose, A. Pilarski, K. Rajana, and J. J. Ditri. Coating influence on generation and reception of ultrasonic lamb type plate waves. *Review of Progress in Quantitative Nondestructive Evaluation*, 13:1903–1910, 1994.

[43] Michael J. S. Lowe. Matrix Techniques for Modeling Ultrasonic Waves in Multilayered Media. *IEEE TRANSACTIONS ON ULTRASONICS, FERRO-ELECTRICS, AND FREQUENCY CONTROL*, 42(4):525–542, JULY 1995.

[44] Emmanuel Moulin, Jamal Assaad, Christophe Delebarre, and Daniel Osmont. Modeling of Lamb waves generated by integrated transducers in composite plates using a coupled finite element-normal modes expansion method. *JOURNAL OF THE ACOUSTICAL SOCIETY OF AMERICA*, 107(1):87–94, JAN 2000.

[45] Emmanuel Moulin, Jamal Assaad, Christophe Delebarre, Sebastien Grondel, and Daniel Balageas. Modeling of integrated lamb waves generation systems using a coupled finite element-normal modes expansion method. *Ultrasonics*, 38:522–526, 2000.

[46] Laurent Duquenne, Emmanuel Moulin, Jamal Assaad, and Sebastien Grondel. Transient modeling of Lamb waves generated in viscoelastic materials by surface bonded piezoelectric transducers. *JOURNAL OF THE ACOUSTICAL SOCIETY OF AMERICA*, 116(1):133–141, JULY 2004.

[47] Jose M Galan and Ramon Abascal. Remote characterization of defects in plates with viscoelastic coatings using guided waves. *Ultrasonics*, 42:877–882, 2004.

[48] James N. Barshinger and Joseph L. Rose. Guided Wave Propagation in an Elastic Hollow Cylinder Coated with a Viscoelastic Material. *IEEE TRANSACTIONS ON ULTRASONICS, FERROELECTRICS, AND FREQUENCY CONTROL*, 51(11):1547–1556, NOV 2004.

[49] Wei Luo and Joseph L. Rose. Phased array focusing with guided waves in a viscoelastic coated hollow cylinder. *JOURNAL OF THE ACOUSTICAL SOCIETY OF AMERICA*, 121(4):1945–1955, APRIL 2007.

[50] P Fellinger, R Marklein, KJ Langenberg, and S Klaholz. Numerical Modeling of Elastic-Wave Propagation and Scattering with EFIT - Elastodynamic Finite Integration Technique. *Wave Motion*, 21(1):47–66, FEB 1995.

[51] F Schubert, A Peiffer, B Kohler, and T Sanderson. The elastodynamic finite integration technique for waves in cylindrical geometries. *JOURNAL OF THE ACOUSTICAL SOCIETY OF AMERICA*, 104(5):2604–2614, NOV 1998.

[52] F Schubert and B Koehler. Three-dimensional time domain modeling of ultrasonic wave propagation in concrete in explicit consideration of aggregates and porosity. *JOURNAL OF COMPUTATIONAL ACOUSTICS*, 9(4):1543–1560, DEC 2001.

[53] F Schubert. Numerical time-domain modeling of linear and nonlinear ultrasonic wave propagation using finite integration techniques - theory and applications. *ULTRASONICS*, 42(1-9):221–229, APR 2004.

[54] Kevin E. Rudd, Kevin R. Leonard, Jill P. Bingham, and Mark K. Hinders. Simulation of guided waves in complex piping geometries using the elastodynamic finite integration technique. *JOURNAL OF THE ACOUSTICAL SOCIETY OF AMERICA*, 121(3):1449–1458, MAR 2007.

[55] A. Abbate, J. Koay, J. Frankel, S. C. Schroeder, and P. Das. Application of wavelet transform signal processor to ultrasound. *IEEE Ultrasonics Symposium*, pages 1147–1152, 1994.

[56] Daniel Masscotte, Jacques Goyette, and Tapan K. Bose. Wavelet-transform-based method of analysis for lamb-wave ultrasonic nde signals. *IEEE Transactions on Instrumentation and Measurement*, 49(3):524–529, 2000.

[57] D. V. Perov, A. B. Rinkevich, and Ya G. Smorodinskii. Wavelet filtering of signals for ultrasonic flaw detector. *Russian Journal of Nondestructive Testing*, 38(12):869–882, 2002.

[58] Hong Wei Lou and Guang Rui Hu. An approach based on simplified klt and wavelet transform for enhancing speech degraded by non-stationary wideband noise. *Journal of Sound and Vibration*, 268:717–729, 2003.

[59] J. Zou and J. Chen. A comparative study on time-frequency feature of cracked rotor by wigner-ville distribution and wavelet transform. *Journal of Sound and Vibration*, 276:1–11, 2004.

[60] J. Hou and M. K. Hinders. Dynamic wavelet fingerprint identification of ultrasound signals. *Materials Evaluation*, 60(9):1089–1093, 2002.

[61] J. Hou, K. R. Leonard, and M. K. Hinders. Automatic multi-mode lamb wave arrival time extraction for improved tomographic reconstruction. *Inverse Problems*, 20(6):1873–1888, 2004.

[62] Mark Hinders, Jill Bingham, Kevin Rudd, Rob Jones, and Kevin Leonard. Wavelet thumbprint analysis of time domain reflectometry signals for wiring flaw detection. *Review of Quantitative Nondestructive Evaluation*, 25:641–648, 2006.

[63] M. Hinders, R. Jones, K. Leonard, and K. Rudd. Wavelet thumbprint analysis of time domain reflectometry signals for wiring flaw detection. *Engineering Intelligent Systems for Electrical Engineering and Communications*, 15(4):225–239, 2007.

[64] J. D. Hou, S. T. Rose, and M. K. Hinders. Ultrasonic periodontal probing based on the dynamic wavelet fingerprint. *Eurasip Journal on Applied Signal Processing*, 2005(7):1137–1146, 2005.

[65] Gerald Kaiser. *A Friendly Guide to Wavelets*. Birkhauser, Boston, 1994.

[66] X Jia. Modal analysis of Lamb wave generation in elastic plates by liquid wedge transducers. *JOURNAL OF THE ACOUSTICAL SOCIETY OF AMERICA*, 101(2):834–842, FEB 1997.

[67] J. R. Davis, editor. *Corrosion of Aluminum and Aluminum Alloys*. ASM International, 1999.

[68] ASTM G 34-01. Standard Test Method for Exfoliation Corrosion Susceptibility in 2XXX and 7XXX Series Aluminum Alloys (EXCO Test). *American Society for Testing and Materials*, 2006.

Vita

Jill Bingham was born in Norfolk, Virginia on July 14, 1982. She attended Maury High School where she graduated with high honors in June 2000. She was also named the "Science Student of the Year." Jill received her Bachelor's of Arts degree from Carleton College located in Northfield, Minnesota in June of 2004. Where she was inducted into the Scientific Research Society Sigma Xi. In the fall of 2004 Jill started graduate work as a Graduate Assistant in the Nondestructive Laboratory in the Applied Science Department at The College of William and Mary. She completed and successfully defended her dissertation December 11, 2004. After completion of her doctorate, Jill moved to Washington DC.